LAPPEENRANTA UNIVERSITY OF TECHNOLOGY

LUT School of Energy Systems

LUT Mechanical Engineering

Eetu Kivirasi

MACHINE VISION CAMERA BASED SPATTER ANALYSIS SYSTEM FOR DMLS PROCESS

Examiners: Professor Antti Salminen, LUT

              M.Sc. (Tech) Juha Kotila, EOS

Supervisors: D.Sc. (Tech) Heidi Piili, LUT

              Ph.D. Pilvi Ylander, EOS

TIIVISTELMÄ

Lappeenrannan teknillinen yliopisto
LUT School of Energy Systems
LUT Kone

Eetu Kivirasi

Machine vision camera based spatter analysis system for DMLS process

Diplomityö

2018

90 sivua, 63 kuvaa, 5 taulukkoa ja 11 liitettä

Tarkastajat: Professori Antti Salminen, LUT

DI Juha Kotila, EOS

Hakusanat: metallin lisäävä valmistus, jauhepetitulostus, direct metal laser sintering, konenäkö, nestelinssi, roiskeanalyysi, syntymekanismi

Tämä diplomityö kartoittaa DMLS-prosessin eri vaiheita ja niistä syntyviä kylmiä ja kuumia roiskeita. Tämä diplomityö tehtiin osana Electro Optical System Oy:n projektia, jossa tarkoituksena oli kehittää uusi työkalu R&D-osastolle (tutkimus & kehitys). Roiskeiden syntyä tutkittiin tätä työtä varten kehitetyllä konenäköpohjaisella roiskeanalyysijärjestelmällä. Mittauslaitteisto valmistettiin, koska markkinoilla ei ollut vastaavaa saatavilla. Mittauslaitteisto koostuu konenäkökamerasta, nestelinssistä, kiinnitysjärjestelmästä ja analyysiohjelmistosta. Metallin lisäävän valmistuksen monitoroinnissa kiinnostus on siirtynyt lähemmäs prosessin reaaliaikaista tarkkailua. Tarkkailun avulla voidaan saavuttaa kustannustehokkaammin parempilaatuisia kappaleita ja tehostaa laadunvalvontaa prosessin aikana.

Työ koostuu kirjallisuuskatsauksesta ja kokeellisesta osasta. Kirjallisuusosassa esitellään yleisimmät käytössä olevat monitorointijärjestelmät metallin lisäävässä valmistuksessa sekä roiskeiden syntyteoriaa. Kirjallisuushavaintojen perusteella päätettiin tutkia lämmöntuonnin, lasertehon ja skannausnopeuden vaikutusta melt poolin käyttäytymiseen ja roiskeiden syntyyn. Kokeellisessa osassa tutkittiin eri prosessiparametrien vaikutusta roiskeiden määrään ja nopeuteen ja melt poolin muotoon EOS:n M 290-koneella. Saadut tulokset vastasivat kirjallisuudessa esitettyjä teorioita. Kehitetyllä mittauslaitteistolla saatiin teorioita tukevat mittaustulokset.

ABSTRACT

Lappeenranta University of Technology
LUT School of Energy Systems
LUT Mechanical Engineering

Eetu Kivirasi

Machine vision camera based spatter analysis system for DMLS process

Master's thesis

2018

90 pages, 63 figures, 5 tables and 11 appendices

Examiners: Professor Antti Salminen, LUT

  M.Sc. (Tech) Juha Kotila, EOS

Keywords: additive manufacturing, powder bed fusion, direct metal laser sintering, machine vision, liquid lens, spattering analysis, spattering theories

This thesis examines the different phases of the DMLS process and the hot and cold spatters that are formed in the process. This thesis was made as a part of Electro Optical System Oy's project to develop a new tool for the R&D department. The melt pool generated spatters were studied by a machine vision based spatter analysis system developed especially for this thesis. The measuring system was manufactured because there were no commercially available measuring systems. The measuring system consists of a machine vision camera, a liquid lens, and attachment system and analysis software.
In monitoring of additive manufacturing the interest has shifted closer to the online monitoring of the process. It is possible to achieve better part quality more cost-efficiently and optimize the quality control during the process.

The thesis consists of a literature review and an experimental part. The literature section outlines the most commonly used monitoring systems for additive manufacturing and theories about spattering. Based on literature findings, it was decided to investigate the effect of heat input, laser power and scanning speed on melt pool behavior and spatter formation. In the experimental part, the effect of different process parameters on the number and velocity of spatters and the melt pool was studied using the EOS M 290-machine. The results obtained corresponded to the theories in the literature. The obtained measurement results by the developed measuring equipment also corresponded to the theories in the literature.

ACKNOWLEDGEMENTS

Eetu Kivirasi

Turku   01.04.2018

TABLE OF CONTENTS

Appendix XI: Analysis procedure using Osirec

LIST OF SYMBOLS AND ABBREVIATIONS

H_d	Hatch distance [mm]
L_t	Layer thickness [mm]
P	Laser power [W]
V_s	Scanning speed [mm/s]

316L	EOS StainlessSteel 316L
AM	Additive Manufacturing
CMOS	Complementary Metal Oxide Semiconductor (image sensor type)
CPM	Comfort Powder Module
DFAM	Design for Additive Manufacturing
DMLS	Direct Metal Laser Sintering
DZ	Denuded Zone
EOS Oy	Electro Optical Systems Finland Oy
EOS VED	Volume Energy Density used by Electro Optical Systems
HS	High Speed
Kn	Knudsen number
L-PBF	Laser Powder Bed Fusion
LP	Laser Power
LPM	Laser Power Monitoring
MP1	EOS CobaltChrome MP1
MPM	Melt Pool Monitoring
OT	Optical Tomography
PIV	Particle Image Velocimetry
SS	Scanning Speed
Torr	Pressure unit (1/760 of a standard atmosphere)
QA	Quality Assurance
QC	Quality Control
R&D	Research and Development
SEM	Scanning Electronic Microscope
VED	Volume Energy Density

1 INTRODUCTION

The layer-by-layer manufacturing technology was found in early 1970s, which was the precursor of the laser cladding process. In the late 1970s molding process forming three dimensional parts layer-by-layer was patented, which was concept of Selective Laser Sintering (SLS) systems. Additive manufacturing (AM) became available in the late 1980s and Direct Metal Laser Sintering (DMLS) machines in mid 1990s. This is when the era of rapid prototyping had begun. Ever since that day the evolution of powder bed fusion (PBF) based technologies have been fast. AM technologies are considered as the third industrial revolution, because it has revolutionized traditional manufacturing process. (Gu, 2015, pp. 1-25.)

AM has made it possible to manufacture complex shapes and integrated parts which cannot be manufactured with traditional manufacturing methods. It is possible to build parts with multi-components from 3D CAD model layer-by-layer without the need for assembly. The strength-weight ratio of the part can be optimized with Design for Additive Manufacturing (DFAM) and topography optimization. (Atzeni & Salmi, 2015, pp. 500-506.)

Laser additive manufacturing process is usually carried out without any monitoring or control. Monitoring and controlling in the manufacturing process are still seldom used in the industry, because monitoring systems for AM has not been on the markets for long. Most of the defects in DMLS are caused by unstable process and spatters formed by this instability landing on top of the build layer. The main goal in AM process monitoring is to observe the quality of the process, and in the future to develop real-time closed-loop feedback control. Based on a high quality monitoring system, it is possible to build a closed loop system that manages the process parameters in real time to ensure better part quality. Process monitoring has raised the quality of the build part and more attention has been paid to the importance of monitoring in recent years in AM, because markets have shown that there is a commercial need for monitoring systems. When aim is to reduce the amount of the spatters, improve the process reproducibility and save costs, process monitoring and controlling are essential, because with monitoring systems it is possible to develop more efficient and faster processes without sacrificing part quality. (Bi et al. 2013,

Pavlov et al. 2010, Spears et al. 2016.) The thesis topic came from an idea to improve quality of parts and the best way to build high quality parts is to know more about the melt pool behavior and spatter generation.

Different monitoring systems are a hot topic at the moment and EOS wants to develop new monitoring tool to complete and combine their monitoring product family. The focus of this monitoring system is to monitor the building process inside the build chamber. When comparing to the other EOS monitoring systems this machine vision camera based spatter analysis system is different because it gathers information of the process stability and of the forming spatters, condensate and smoke. This monitoring system also offers information for process optimization to minimize these forementioned spatters, condensate and smoke. The motivation to create this monitoring system is to get a tool for R&D (research and development) department. The quality-price ratio of machine vision cameras and computer calculation power is getting more reasonable, and this makes it even more fascinating solution, eventually for closed loop control. Interest for closed-loop systems in machine vision inspection is rapidly increasing in the technical and engineering sector. (Beyerer et al. 2016.) Aim of this Master`s Thesis is to characterize and understand the basic phenomena of spattering by utilizing machine vision camera based spatter analysis system. This thesis was done in the research and development department of Electro Optical System Oy.

The focus of this thesis is on the development of the spatter analysis system. There are no commercially available machine vision based monitoring systems for the DMLS process and that is why EOS decided to build it for R&D-tool to help process. The prototype has been designed and manufactured within this Master's Thesis for EOS M 290 machine. Spatter analysis software is custom made for EOS based on given specs of the desired monitoring parameters.

This thesis will primarily benefit research and development department of EOS by offering new tools to detect and understand spatters effect on the part quality. This thesis also helps to identify spatter formation by comparing images to process parameters and to bring new perspective and ideas into process development.

2 BACKGROUND

The first DLMS system EOSINT M 160 was presented for public in 1994. EOS launched EOSINT M 250 DMLS system for AM in 1995 and EOSINT M 250 Xtended was launched with 20 μm layer thickness processes in 2001. Earlier machines used carbon dioxide (CO_2) laser and the first commercially available DMLS system EOSINT M 270 with fiber laser launched in 2004. Fiber laser was a game changer for DMLS process quality because the fiber lasers have much better beam quality than earlier used CO_2 lasers. Metal materials absorb with fiber laser produced wavelengths (~ 1064 nm) better than CO_2 laser wavelengths (~ 9000-10000 nm). EOSIN M 280 with optional 200 W or 400 W filer laser was introduced in 2010. EOS launched in 2011 Laser Power Monitoring (LPM) which monitored laser power stability during the build process and Comfort Powder Module (CPM) which offers safe powder handling in the closed process chamber for further quality assurance. EOS M 400 with one kW fiber laser was presented in 2013. EOS M 290 machine with 400 W fiber laser was launched in 2014. Real time EOSTATE MeltPool monitoring and analysis system, which monitor complex melting process by measuring light emissions of the melt pool for M 290 machines, was introduced in 2015. The largest and fastest DMLS systems EOS M 400-4 with four 400 W fiber lasers was presented in 2016. Real time monitoring system EOSTATE Exposure OT for additive manufacturing, which uses optical tomography to reduce costs of non-destructive examinations, was presented in 2017. (EOS, 2018a.)

Monitoring in additive manufacturing has its importance because the stability of the process was influenced by several parameters, such as laser power, scan speed, hatch distance and layer thickness, at the same time. The goal of the process monitoring was to enable quality assurance during the build process by improving the understanding of melt pool behaviour and spattering phenomena occurring during DMLS process. Melt pool stability has a large impact on the quality of build parts because melt pool determines whether the process was in keyhole, transition keyhole or conduction mode. In the keyhole mode the melt pool is from three to five layers deep, whereas in the conduction mode the melt pool is wider and shallower. These different process modes are shown in figure 1.
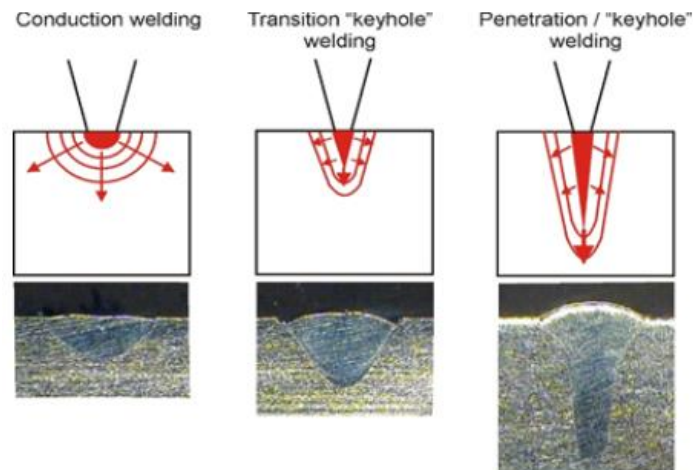
Figure 1. Schematic with microscopic image of the different process modes depending of the heat input. Red colored area in the schematic presents cavity keyhole, inner red line presents melt pool and outer red line heat affected zone. (LASERSTODAY, 2018a).

The process modes have different phenomena causing the spattering. For example in the conduction mode prevalent spattering phenomena is entrainment driven spattering and in the keyhole mode prevalent phenomena is recoil pressure driven spattering. Regardless of process mode, most of the large hot spatters are generated from a melt pool by Marangoni effect and recoil pressure. The Marangoni effect influences to the melt pool fluid flow and recoil pressure is prevalent phenomena for large melt pool origin hot spatters. The reason why monitoring systems have been built for AM was for quality control by monitoring several parameters to find correlations between them and part quality.

There are a few commercially available monitoring systems for additive manufacturing. According to (Purtonen et al. 2014), the object of monitoring is the improvement of reproducibility, assurance of reliability and quality of the process within a single manufacturing cycle and between several cycles.

2.1 Objectives

The objective of the literature review is to provide a comprehensive overview to state-of-art studies in machine vision camera based monitoring systems. The aim is also to provide information of melt pool behavior, spattering phenomena and spatter origin. Objectives of the experimental part of this thesis are to identify the required properties of the machine vision camera based spatter analysis system, define the origin of spatters and introduce

spatter types. The aim is also to introduce which machine modifications are required. Significant consideration is given to the analysis system assembly and testing, as the main target of the experimental part of this thesis is to build and test the measurement system that meets the requirements for monitoring additive manufacturing.

This study seeks answers to the following research questions:

1. How spatters are defined?
2. How do spatters form?
3. How it is possible to image spatters with machine vision camera?
4. How spatters can be measured with this imaging system?
5. How the measurement system was built to be suitable for monitoring spatters and melt pool with EOS requirements?
6. What limitations spatter analysis systems have?
7. How measured data can be used in research and development department?

2.2 Scope

The used literature consists mostly of pre-reviewed scientific articles, selected books and company web pages. Literature reliability is increased by cross referencing. Used material is from the databases of the library of Lappeenranta University of Technology, databases and general network resources. The experimental part of this study consists of measurement system design, manufacturing, assembling and tests to attempt to recognize spatter formation phenomena. The main goal is to build proper R&D tool for the use of EOS R&D engineers and gather more information of spatter formation phenomena.

This thesis will concentrate on DMLS process, which EOS has named its laser-based powder bed manufacturing process. This thesis will focus to CMOS (complementary metal oxide semiconductor) cameras in field of different machine vision cameras, because those cameras have the best image quality at the moment, and the data volume can be post processed for numerical and statistical form. This thesis will also focus to active illumination laser technology (custom made Oseir HiWatch Compact) in field of different illumination technologies, because laser illumination is proven to be the best illumination option for particle imaging. Prototype assembly is limited to EOS M 290 machines because it has EOSTATE MeltPool monitoring system and EOSTATE Exposure OT monitoring system.

3 MOST USED MONITORING SYSTEMS IN METAL ADDITIVE MANUFACTURING

The objects of monitoring are; 1) to improve reproducibility by observing the machine functions, for example oxygen level, shield gas pressure, laser power and layer thickness. 2) Assurance of reliability by monitoring process parameters, for example laser power and scanning speed. 3) Quality of the process within one or several manufacturing cycles by monitoring melt pool stability. 4) Experimenting, for example how the spatters form when using different parameters. 5) Gathering information systemically to teach self-learning algorithms to detect defects. 6) Understanding the process and the phenomena behind it, by comparing measurement data to the theories. (Purtonen et al. 2014.)

3.1 Photodiode-based process monitoring

Electro Optical System has developed in collaboration with Plasmo a photodiode based melt pool monitoring system with four channels at sampling rates up to 300 kHz. Monitoring system measures the brightness of the process emissions giving fast feedback about the quality of the process. Heuristic model is created to gather input and output parameters to collect enough data. Based to this data the system can be parametrized to fulfill the quality needs. Monitoring system corresponds to part properties by enabling the fully automated detection of process phenomena. The system layout of EOSTATE Meltpool is presented is figure 2.
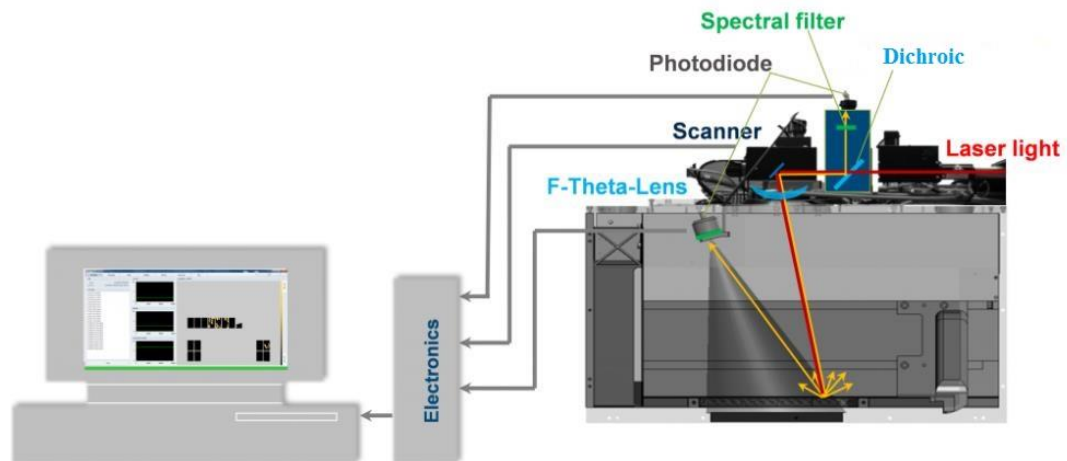
Figure 2. EOSTATE Meltpool uses two photodiodes. OnAxis diode measures the process emissions of the laser beam and powder at the interaction zone. Overview of process emissions of the complete building platform is given by OffAxis. (LASERSTODAY, 2018b).

3.2 Camera-based process monitoring

Electro Optical System has developed in collaboration with MTU Aero Engines a camera-based EOSTATE Exposure OT (OT) monitoring system. The system consists of high resolution (2560 x 2160 pixels) CMOS based camera and NIR wavelengths optics with long depth of field. Entire building platform is imaged and the spatial resolution is 130 µm /pixel. Images correlate to the temperature and size of the interaction zone. All of the images from each layer are integrated to one image, which correlates the emitted heat. OT is a self-learning monitoring system and analysis is based on three analysis algorithms; Threshold-, Deviation Blob- and Simple Blob-Indication Detection. Integrated image taken with EOSTATE Exposure OT is presented is figure 3.
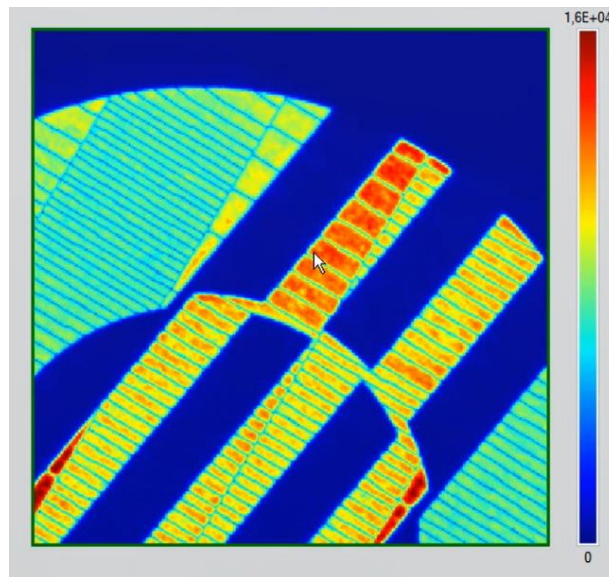
Figure 3. Integrated image taken with EOSTATE Exposure OT showing how OT can detect different exposure strategies heat input. (3Dprint, 2018).

The definition of high-speed camera is more than 1000 frames per second at megapixel resolution. Generally high-speed cameras are based on high-end CMOS and CCD censors. Because of the limited band width and amount of data, the data is recorded in to local memory. High-speed cameras need high powered illumination for high-quality images because of the short exposure time. When the resolution of images is reduced, the framerate is increasing. For example, with Phantom VEO 710 full resolution (1280 x 800) the framerate is 7400 and reduced resolution (256 x 256) the framerate is 75 000. When using high-speed cameras, the resolution has a high influence to the frame rate. High speed cameras produce large amount of data and therefor it is not possible to monitor entire build process or analyze it. (Batchelor. 2012, pp. 358-397 & ResearchGate, 2018.)

Machine vision cameras use CCD or CMOS image sensors. The subcategories of these two sensors are color and monochrome. CMOS sensor sizes of machine vision cameras are between 1:1.2″ - 41.0 mm. (photographylife, 2018.) Typical sensor sizes of machine vision cameras are presented in figure 4. High resolution fast frame rate cameras use CMOS image sensors because they are ten times faster than CCD sensors. Machine vision cameras have a special high dynamic range, for both bright and dark conditions. Machine vision cameras have high frame rates even with full resolution, for example, with 20 megapixels up to 30 frames per second (fps) and 5 megapixels up to 250 fps. (jai, 2018). Unlike high-

speed cameras, machine vision cameras are connected to a computer with a cable (Camera-Link, Gig-E or USB3) for real-time high-speed communication. (emva, 2018). The camera is transferring images to the computer hard drive, and this makes it possible to image long-term without interrupting the imaging or without changing the memory cards. (Batchelor. 2012, pp. 358-397).
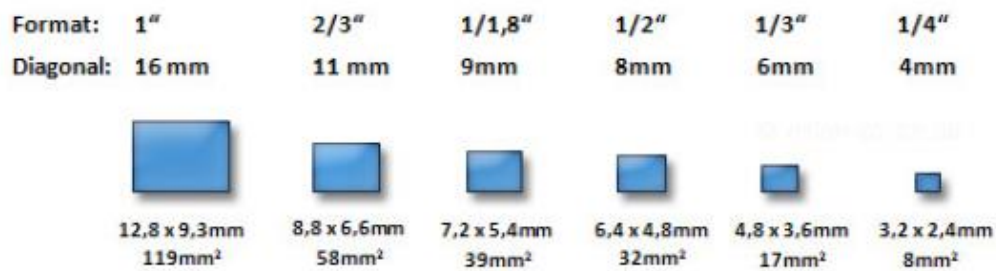
Figure 4. Machine vision camera sensor sizes. (Vision Doctor, 2018).

Another example of recent development in monitoring of additive manufacturing is that CMOS and CCD cameras are not suitable when moving from VIS-NIR wavelength to infrared (IR) wavelength, because CMOS and CCD cameras are not able to detect these wavelengths. Therefore, infrared cameras are needed. Infrared cameras are divided in to two main categories, which are cooled and uncooled detectors. Uncooled detectors can be separated further in to two different subcategories, which are microbolometers and ferroelectric detectors. When high spatial resolution and high sensitivity are wanted, a vanadium oxide (VOx) microbolometer offers better features than the ferroelectric detector. There are only a few high quality commercially available optics for infrared cameras because fused silica lenses have a low transmittance of infrared radiation and therefore high priced germanium lenses must be used. (Batchelor. 2012, pp. 399-405 & Gade et al. 2014). Resent articles about camera based monitoring researches are gathered into table 1.

Table 1. PBF-process monitoring with camera systems. Camera type: Digital single-lens reflex camera (DSLR), High speed camera (HS). Sensor Type: Complementary metal oxide semiconductor camera (CMOS), Thermographic camera (Thermal). Material: aluminum alloy (Al), steel alloy (Fe), nickel alloy (Ni), stainless steel (SS), titanium alloy (Ti). Process: Direct Metal Laser Sintering (DMLS), Laser Powder Bed Fusion (LPBF), Powder Bed Fusion (PBF), Selective Laser Melting (SLM).

Camera	Camera type	Sensor type	Illumination	Material	Process	Target	Term	Reference
FASTCAM Mini UX100	HS	CMOS	Laser	SS	PBF	Schlieren	Particle	Bidare et al. 2017
FASTCAM SA2 Photron	HS	CMOS	-	SS	SLM	Melt pool	Spatter	Gunenthiram et al. 2018
-	-	-	-	SS	LPBF	Melt pool	Spatter	Heeling & Wegener, 2016
-	-	-	-	SS	LPBF	Melt flow	Spatter	Khairallah et al. 2016
-	-	-	-	Ni	SLM	Gas flow	Spatter	Ladewig et al. 2016
AOS SPRI-F2	HS	CMOS	-	SS	SLM	Spatter beahvior	Spatter	Liu et al. 2015
Olympus I-speed 3	HS	CMOS	-	Fe	LPBF	Monitoring	Spatter	Repossini et al. 2017
-	-	-	-	Ti	SLM	Melt flow	spatter	Qiu et al. 2015
Fastcam 1024 PCI	HS	CMOS	LED	Al	SLM	Spatter formation	Spatter	Taheri Andani et al. 2017

3.3 Acoustic-based process monitoring

General Electric (GE) published in May 2017 an acoustic monitoring system for additive manufacturing. GE developed in-situ monitoring system using acoustic waves to improve work flow and simplify the qualification of printed parts. Monitoring is based on using acoustic sensors, which measures acoustic signals during the build process. The system compares measured acoustic profile to the profile of the already qualified part to ensure that the build part is defect free. The main goal of GE is to eliminate post build quality control processes by developing high quality real-time monitoring systems for additive manufacturing. Schematic of acoustic monitoring system is presented in figure 5.
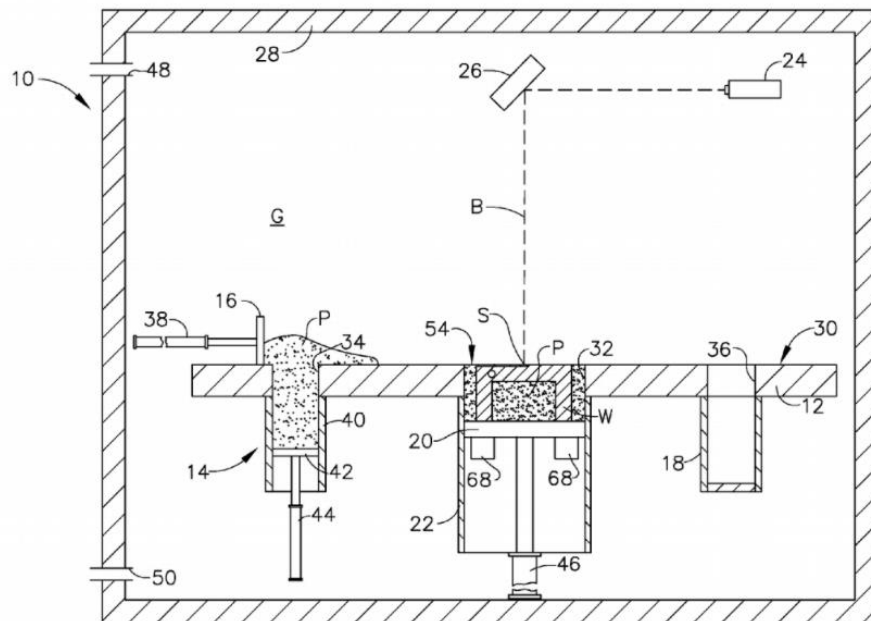
Figure 5. Schematic of the acoustic monitoring system designed by General Electric. Acoustic sensors (68) are located below the building platform to ensure high quality acoustic measured data from the building process. (3Dprinting industry, 2018).

4 SPATTERING THEORIES AND PHENOMENA

The spattering in laser manufacturing processes is a common phenomenon as capillary flow ejects the molten metal droplets out of melt pool, as can be seen in figure 6 (d-g). The capillary flow is molten material flow from bottom of the melt pool towards the surface. When the laser beam is in contact with the material, a melt pool is formed in figure 6 (a). Some of the material is melted and vaporized into plasma and the formed melt pool helps the material to absorb the laser. Spatters are formed because the molten material is compressed by blow off impulse pressure to cause liquid material to leave the melt pool. Capillary flow and melt pool front ejected spattering is shown in figure 6. (Ly et al. 2017.)
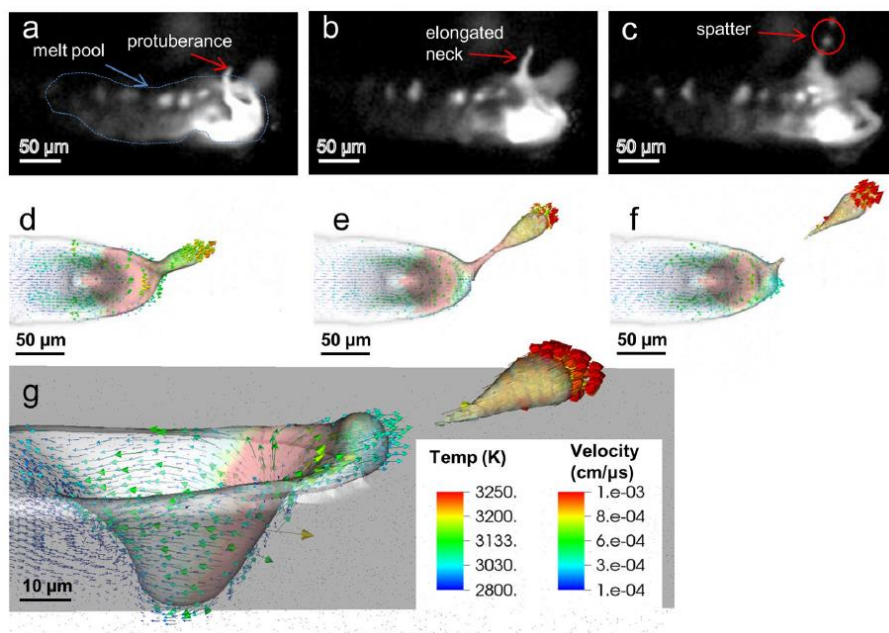
Figure 6. Melt pool ejected spatter forming (Ly et al. 2017).

Wang et al. (2017) presented three different types of spatters. First of the spatter types (I type spatter in figure 7) is metallic jet up towards the laser beam. Shield gas vortex rapidly heated by laser beam is creating this entrainment driven spattering (I type spatter). The second type (II type spatter in figure 7) is droplet spatter from the melt pool in to the opposite direction from scanning direction. This II type spatter is created by recoil pressure and Marangoni effect. Third type (III type spatter in figure 7) of spatter is powder spatter forming in the front edge of the melt pool. This III type of spatter is created by recoil

pressure and snow blow effect. (Wang et al. 2017.) Different spatter types and scanning electron microscope images of powder particle morphology in different type of spatters are shown in figure 7.
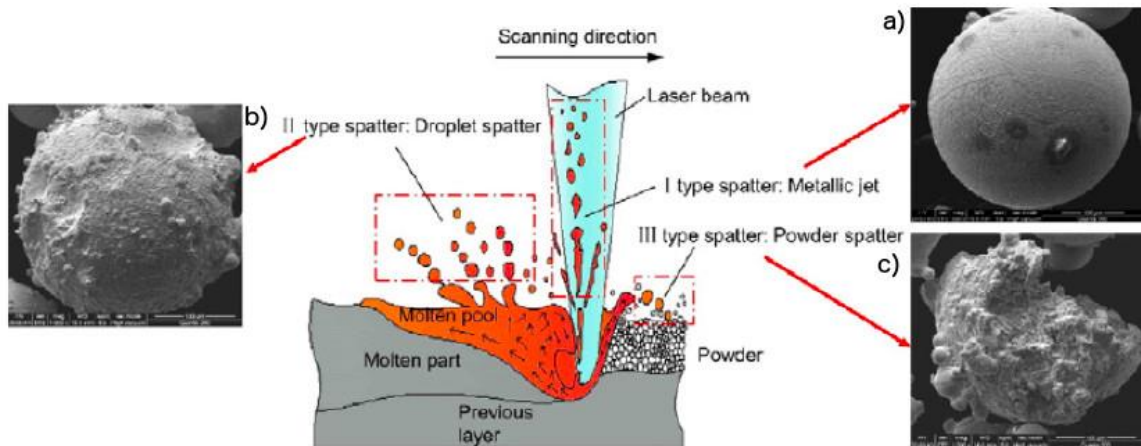
Figure 7. Three different spatter types in powder bed fusion processes with scanning electron microscope (SEM) morphology figures. (Wang et al. 2017).

It can be seen from figure 7(a) that spatter shape is similar to the powder, which indicates that the spatter did not hit to the laser beam. From spatter type II morphology figure 7(b) it can be seen that molten ejection from the melt pool forms droplet spatters. The shape of the spatter is close to the original powder particle. From spatter type III morphology figure 7(c) it can be seen that laser has partially melted the powder particle before ejection and the shape is different than the original powder shape. Spatter particle size is approximately five times larger than initial powder because these particles form of multiple molten powder particles. (Wang et al. 2017.) More precise figure of particle morphology and size can be seen in appendix I (Morphology).

Liu et al. (2015) have classified two types of spatters: droplet and powder based. Both spatter types are generated by recoil pressure and metallic vapor, as it can be seen in figure 8 a) and 8 b). Metallic jet is created by high recoil pressure removing material from melt pool. Metallic vapor crushes metallic jet into droplets during laser irradiation field forming droplet spatter. Powder based spatters are non-melted powder around the melt pool which is sucked in by metallic vapor. The spatter types are presented in figure 8.
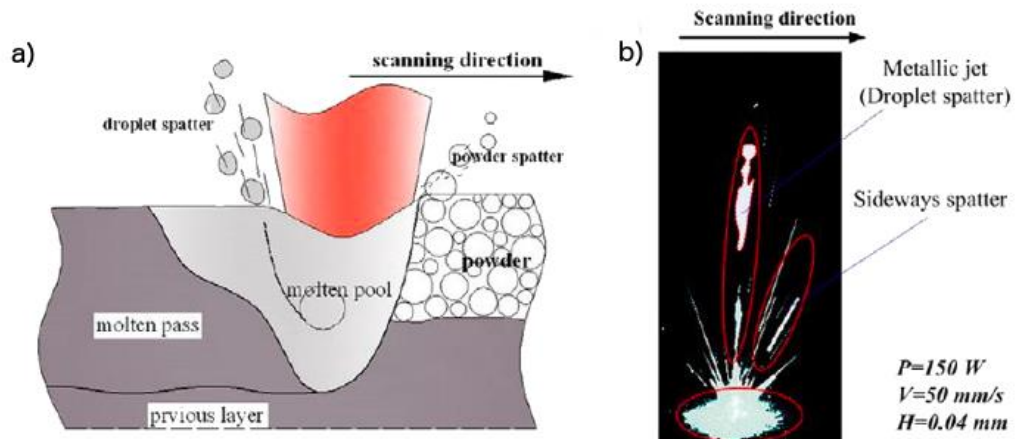
Figure 8. Spatter formation mechanism during PBF process. a) Schematic of the droplet and powder spatters. b) Image taken from side of the melt pool showing spatters.   (Liu et al. 2015).

Small powder based spatters (spatter A in figure 8) affect the final properties of build parts, for example by decreasing the density and mechanical properties. Larger droplet based spatters (spatter B in figure 8) affect to the powder recoating forming unwanted heterogeneous layer thickness. Powder layer thickness is near the size of the particle A and it can be melted by the laser beam. The size of particle B is larger than layer thickness, therefore it has influence on the next layer thickness near particle. Because of larger size than layer thickness, the laser cannot melt in the same way as the rest of the layer. Spatters influence on the layer thickness is shown in figure 9. (Liu et al. 2015.)
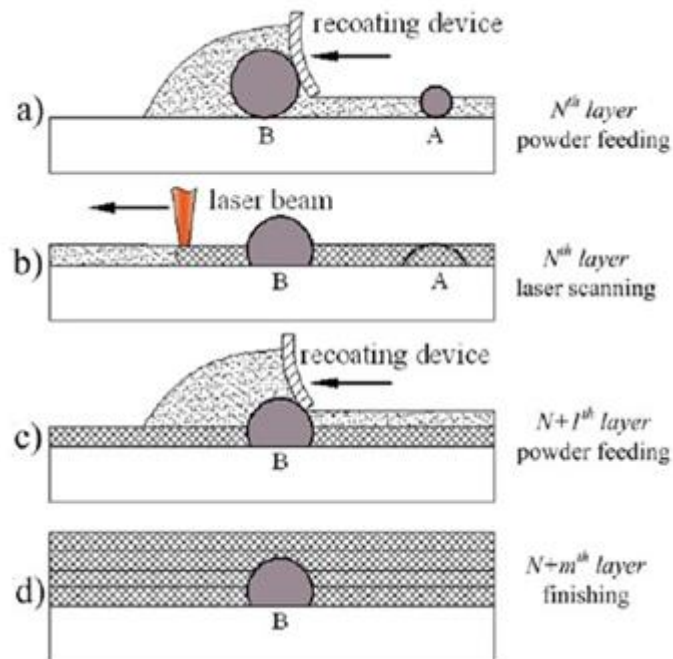
Figure 9. Large Spatter causing heterogeneous layer thickness to the powder bed during PBF process. (a) Schematic of the spatters on the next layer. (b) Un-melted droplet based spatter after scanned layer. (c) Large spatter causing heterogeneous layer thickness on several layers. (d) Spatter B forming defect inside the build layers. (Liu et al. 2015).

The PBF process is very sensitive to the oxygen and conditions of the atmosphere in the building chamber. Oxidized spatters on top of the powder bed will be re-melted and that causes pores to the part. It is proven by microstructure analysis and tensile strength tests that spattering degrades the quality of build part. Healing effect from the next layer reduces the spatter impact on the part quality by importing heat to the defect. (Ladewig et al. 2016.) Figure 10 presents how large spatters cause heterogeneous powder layer thickness causing uneven melting which in turn causes pores.
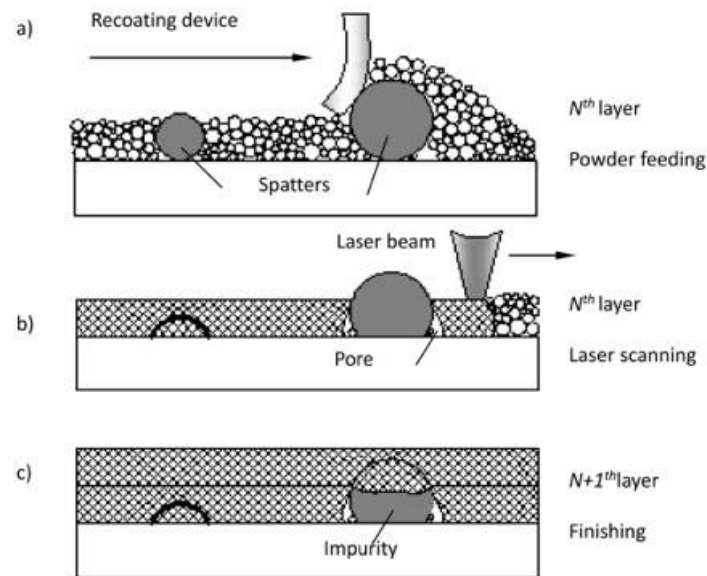
Figure 10. The oxidized spatters decrease the quality of the build layer. (a) Schematic of the large spatter causing pore formation, (b) pore formation in laser scanning and (c) the finished layer. (Wang et al. 2017).

Spattering is caused by many reasons, such as rapid melting and cooling, heat transfer and melt pool instability, which can be seen from figure 11. Dark blue color particles in figure 11(a) presents powder before the laser beam is focused to the powder bed. In figure 11 (b-d) laser beam heat powder bed surface rapidly Lavery et al. (2014) investigated the effect of the laser power on the porosity of the final part using Latice-Bolzmann simulation of a 316L powder melted by a 200 W laser. Because of rapid melting and cooling of the melt track and melt pool stability, it is difficult to define the root cause of spattering accurately. (Liu et al. 2015, Simonelli et al. 2015 & Wang et al. 2017.)
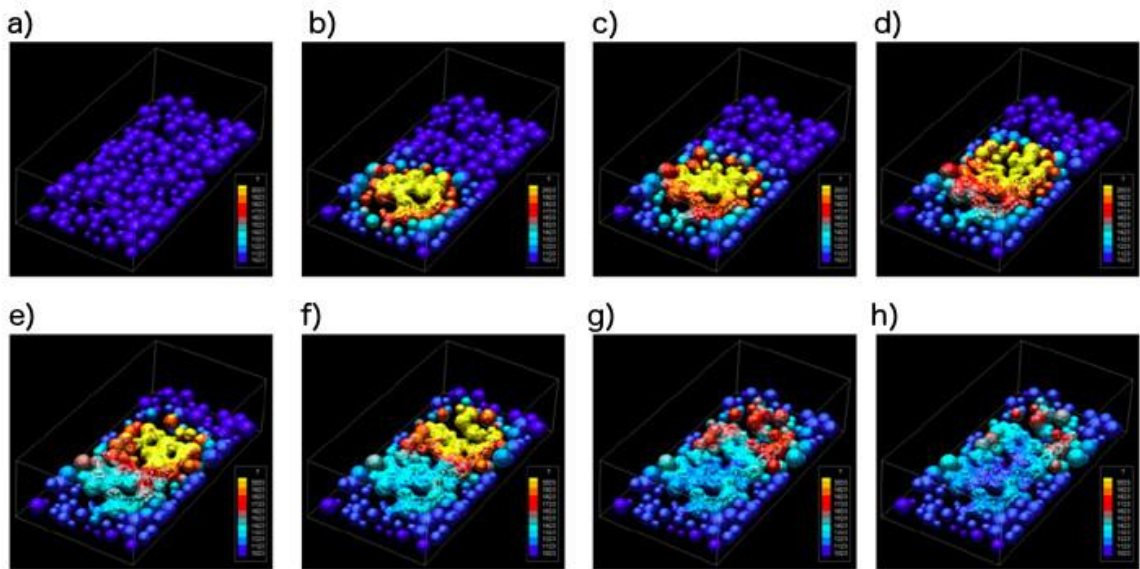
Figure 11. 3D Lattice-Bolzmann simulation of PBF process. (Lavery et al. 2014).

4.1 Recoil pressure driven spattering

Studies of melt pool ejections and the underlying mechanisms are limited in PBF processes. These mechanisms are widely investigated in laser welding processes. PBF and welding processes differ significantly from each another, for example, the laser spot size is near 1 mm in laser welding and approximately 80 μm in PBF. Therefore PBF results cannot be compared to the laser welding results. Melt pool flow is also different in powder bed processes, because powder particles have different thermal conductivity than for example solid plates in laser welding. Laser beam creates strong metal evaporation around itself and rapidly heating metal vapor vortex generates recoil pressure gradients causing melt ejection from melt pool. Ly et al. (2017) have studied spatter formation with powder layer and solid plate situation in figure 12 using particle image velocimetry (PIV).
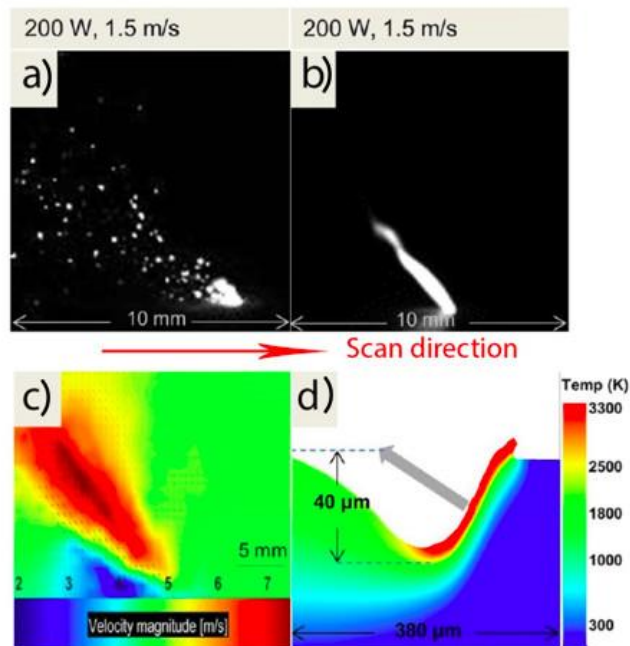
Figure 12. a) Recoil pressure driven spattering from powder bed and b) from platform. c) Recoil pressure driven material jet simulation from powder bed. d) Grey arrow showing expected direction of the vapor plume in simulation model from platform. (Ly et al. 2017).

Recoil momentum (which can be seen in figure 12(d) as grey arrow) and melt pool flow motion (which can be seen in figure 13(g-j) as orange droplet) buildup of liquid molten material ahead of the laser beam causes forward plowing liquid ejections. Ejections are large (25-100 μm) when compared to the powder layer thickness (40 μm). When the laser energy per unit volume decreases, the laser scan speed increases and melt pool becomes shallower. The high temperature region spreads out to the melt pool front (which can be seen in figure 13(d) as red) and therefore the vapor plume form backwards of the scanning direction (which can be seen in figure 12(a-b)). When the laser energy is insufficient to melt the melt pool front and create an efficient recoil pressure, the amount of spatters are expected to reduce, because recoil pressure phenome creating spatters is decreased. If the kinetic energy is greater than the surface tension of the molten material, melt pool can eject spatters in the opposite direction of the scanning direction. (Ly et al. 2017.) Melt pool ejected droplet spatters are presented in figure 13.
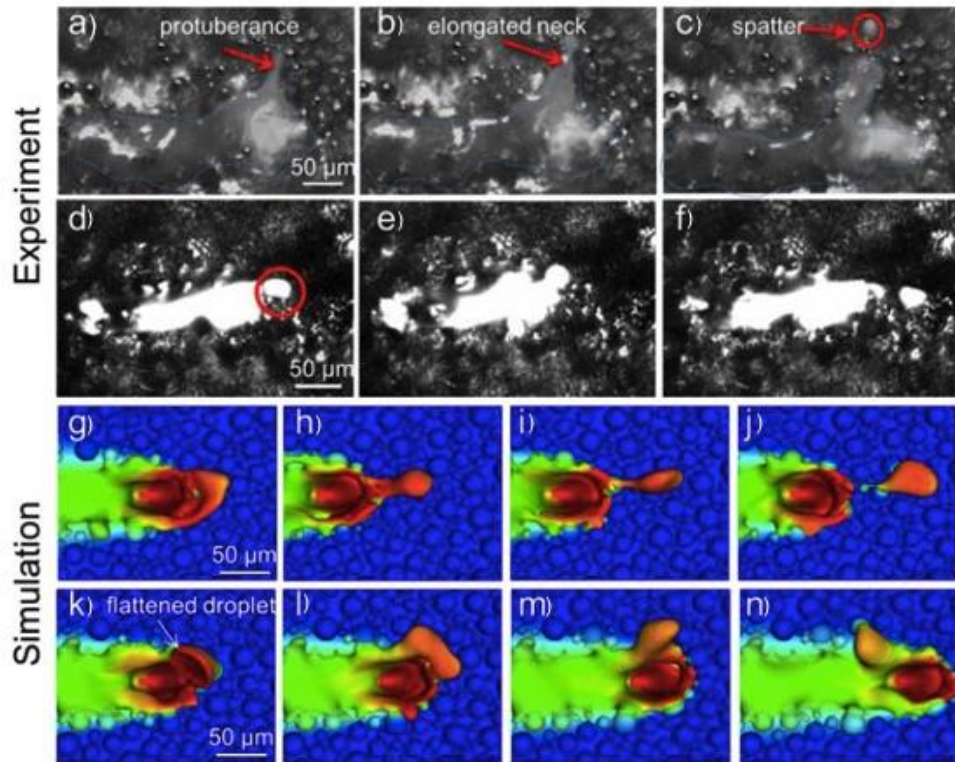
Figure 13. Comparison between experiment (a-f) and simulation (g-n) of spatter formation. (Ly et al. 2017).

Experimental test series (a-c) made of titanium, used parameters was power = 300 W and scanning speed 1.5 m/s. Test series (d-f) made of stainless steel, used parameters was power 200 W and scanning speed 2.0 m/s. Simulation (g-j) shows droplet ejection and (k-n) present sub-threshold ejection. Melt pool dynamics and forwarded flow motion create protuberance (which can be seen in figure 13a). Melt pool created elongated neck thins out and droplet spatter is ejected (which can be seen in figure 13b-c) (Ly et al. 2017).

4.2 Entrainment driven spattering

There are at least three different types of entrainment driven spatters: (1) subsumed particles which are pulled into the melt pool, (2) cold particles that are pulled towards to the vapor jet but miss the laser beam or (3) powder particles which travel towards the vapor jet, hits to the laser beam and become hot molten spatters. Different types of entrainment driven spatters and the gas flow wakefield is presented in figure 14. The laser beam creates vapor flux from the melt pool which causes inward gas flow (which can be seen in figure 14a). This vapor flow, similar to the physics of the submerged jet, pulls

particles along the vapor flow (which can be seen in figure 14b). Vapor jet forming takes some time because moving laser beam is creating gas flow around the jet
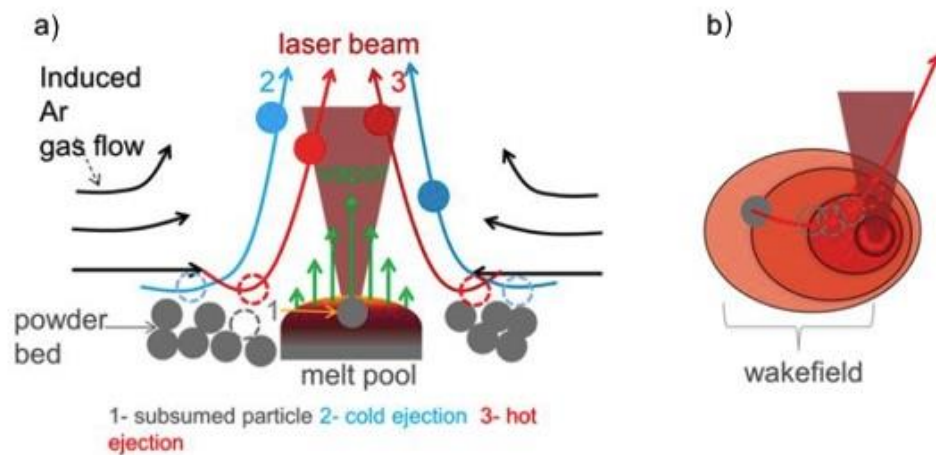
Figure 14. a) Schematic of the three different types of entrainment driven spatters created by vapor jet. b) Moving laser beam and vapor jet created wakefield. (Ly et al. 2017).

Type 1 powder particles are located near the melt pool, type 2 powder particles originate more than two times melt pool width away and type 3 powder particles are originated under two times melt pool width away. The moving laser beam creates a non-uniform jet stream wakefield that extends to three to four times laser beam diameters away (which can be seen in figure 14b). (Ly et al. 2017).

According to Ly et al. (2017), vapor vortex created by laser beam raise up dark cold particles from powder bed (marked in blue color in figure 15a) and incandescent hot particles (circled red in figure 15a). Vapor vortex has lifted particles to motion (which can be seen in figure 15b as blue and red arrows). Entrainment driven spattering process starts to repeat itself (which can be seen in figure 15d). (Ly et al. 2017.) Melt pool formation and spatter ejections are shown in figure 15.
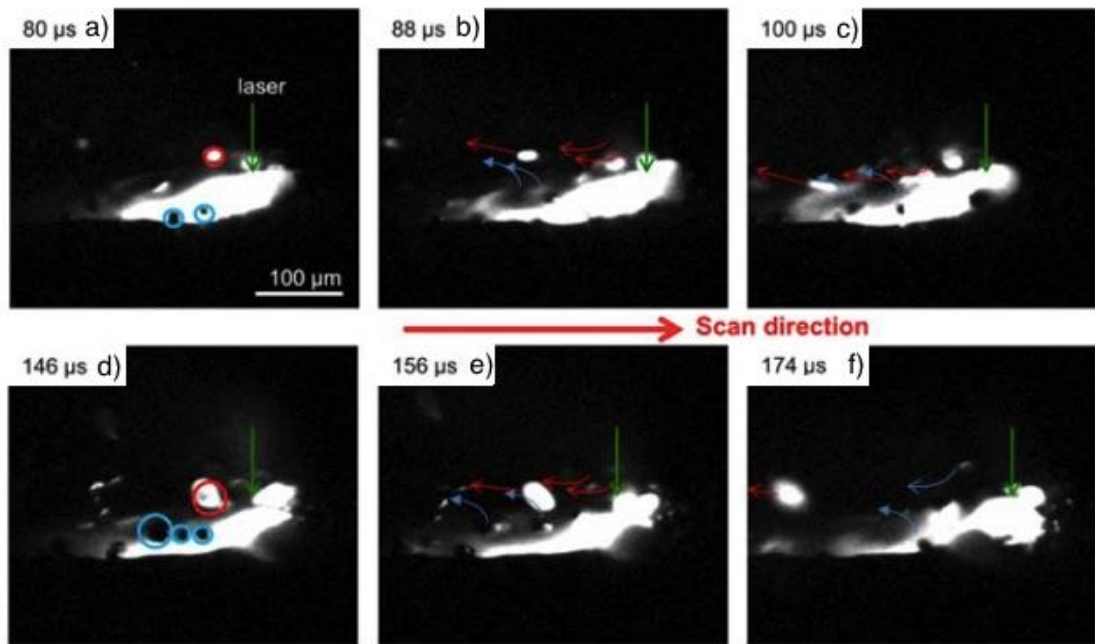
Figure 15. Melt pool formation progression from 80 µs to 174 µs. Used laser power was 300 W and scanning speed 1500 mm/s. (Ly et al. 2017).

When cold powder particles are accelerated by the vapor vortex, particle velocity rises from 1 m/s to 4 m/s (which can be seen in figure 15b). When cold particles pass through the laser path, they are rapidly heated and start to emit light by themselves. Particle velocity rises up to 6-15 m/s when passing through laser beam path (which can be seen in figure 15e). Based on Ly et al. (2017), 60 % of spatters are hot ejections, 25 % are cold ejections and 15 % from recoil pressure induced ejections. Entrainment driven spattering and simulations is presented in figure 16.
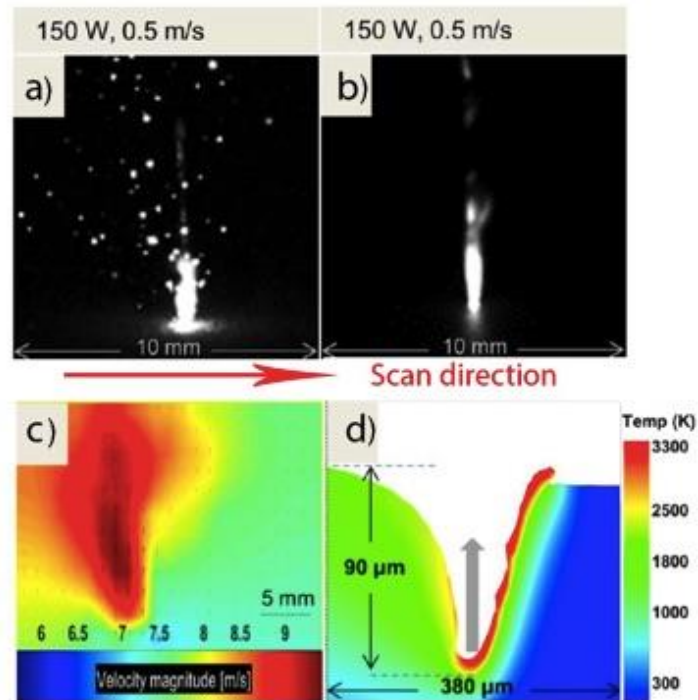
Figure 16. a) Entrainment driven spattering from powder bed and b) from platform. c) Laser beam created material jet simulation from powder bed. d) Grey arrow showing expected direction of the vapor plume in simulation model from platform. (Ly et al. 2017).

4.3 Denudation

Denudation and the part quality have correlation, because denudation process defines the amount of overlay powder in the scan track. Denudation zone (DZ) width measured from powder bed when laser power was varied is shown in figure 17. The laser power ranging from 10 to 350 W, argon gas pressure was 0.2 Torr and used layer thickness was 60 µm. When the laser power is increasing, melt track width and DZ increases. (Matthews et al. 2016.) Re-solidified melt can be seen lighter contrast from figure 17.
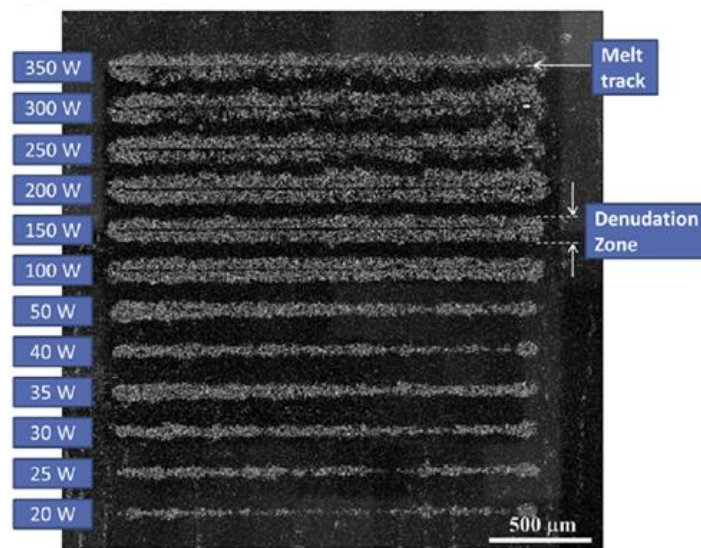
Figure 17. Denudation zone width dependence to the laser power. (Matthews et al. 2016).

Matthews et al. (2016) measured melt track width by using three different scanning speeds and denudation zone width by using two different argon gas pressures and three different scanning speeds. Results are presented in figure 17. Denudation zone width increased almost two times when gas pressure changed from 760 Torr to 0.2 Torr, while melt track width remain constant. When laser power is increasing DZ increases as well in low gas pressure (0.2 Torr). Laser scanning speed increases DZ width more in 760 Torr pressure than in 0.2 Torr pressure. Open symbols represent 0.2 Torr pressure and solid symbols 760 Torr pressure in figure 18. Scanning speed 0.5 m/s is marked as square, 1.5 m/s as circle and 2 m/s as triangle in figure 18.
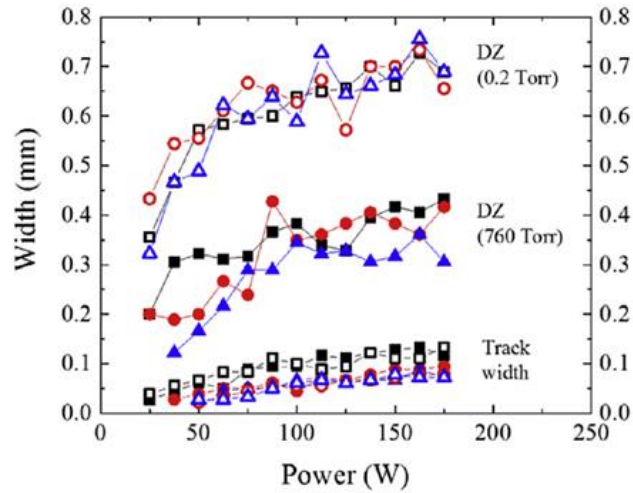
Figure 18. Denudation zone widths as a function of the laser power, scanning speed and shield gas pressure. (Matthews et al. 2016).

Matthews et al. (2016) studied DZ width as a function of argon gas pressure as shown in figure 18. In gas pressure variation for single track tests the parameter for the laser power was 225 W and for scanning speed 1.4 m/s. As it can be seen in figure 18, DZ width at 220 Torr pressure is near 500 μm and lots of overlay particles over the melt track. Denudation zone increases from 500 μm to 800 μm when gas pressure decreases from 220 to 10 Torr. Also the number of overlay particles in melt track decreases with gas pressure, which can be seen in figure 19. Forces creating denudation zone are at relative minimum at 2.2 Torr pressure, this can be seen in figure 19 as the smallest DZ width and the particle size distribution. Small powder particles can be displaced with smaller force than large particles.
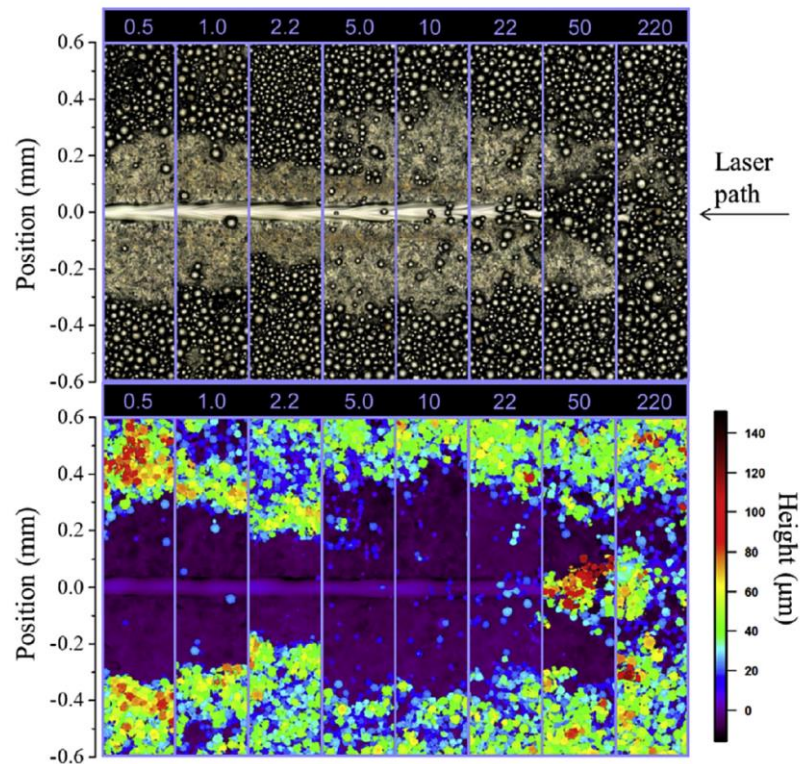
Figure 19. Denudation zone widths as a pressure decreased from 220 to 0.5 Torr. (Matthews et al. 2016).

4.4 Marangoni

Marangoni effect is a strong flow inside the melt pool. It can be seen as a surface tension pulling surface fluid towards the cold spot, producing a small melt pool. The purpose of the thermal Marangoni flow is to transfer heat inside melt pool flow to maintain minimum surface tension. High laser energy density input to the powder bed produces turbulence to the melt pool, which causes intense Marangoni convection. Intense Marangoni convections cause instability to the melt pool which creates pores during PBF process. Simulation of Marangoni convection using different scanning speed is presented in figure 20.
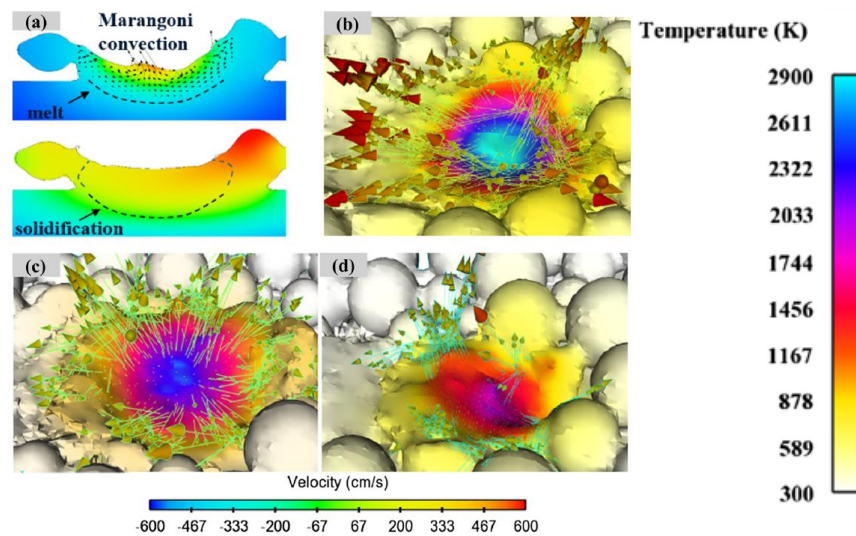
Figure 20. Simulation of Marangoni convection in the melt pool. (Pei et al. 2017).

High scanning speed causes Plateau-Rayleigh instability to the melt pool which increases surface tension and Marangoni convection in the melt pool. The velocity of Marangoni convection inside melt pool is near 4500 mm/s towards the laser beam (which can be seen in figure 20a as orange in the middle of melt pool top surface). Using scanning speed 600 mm/s, melt pool peak surface temperature is near 2900 K and Marangoni convection velocity is approximately 5250 mm/s (which can be seen in figure 20b). When the melt pool is stable, temperature field is circle-shaped and therefore melt track is uniform. Increasing scanning speed to 1000 mm/s, surface peak temperature decreases to 2500 K and the velocity of Marangoni convection decrease to 4 mm/s (which can be seen in figure 20c). When the scanning speed is increased, the melt pool temperature field is decreased. Using scanning speed of 1600 mm/s, surface peak temperature decreases to 1950 K and velocity of Marangoni convection is 2500 mm/s (which can be seen in figure 20d). Small temperature field of the melt pool and low temperature melt pool causes unstable melt pool flow. Unstable melt pool flow increases surface tension and therefore more Marangoni convection, which increases porosity. (Pei et al. 2017.)

4.5 Snow-plow

So-called snow-plow spatters are very large droplet spatters ejected forward from melt pool. In snow-plow the laser beam builds up liquid material forward to the front of the melt pool. When liquid flow meets the wall of depression in front of melt pool, hot ejection spills large spatter over onto the powder bed ahead of the laser beam. Snow-plow ejections

are a way of nature to minimize surface energy by using surface tension. The melt track achieves a lower surface energy after ejection, because the melt pool shape gains a steady state. (Khairallah, et al. 2016.) Melt pool flow as a function of time is presented in figure 21.
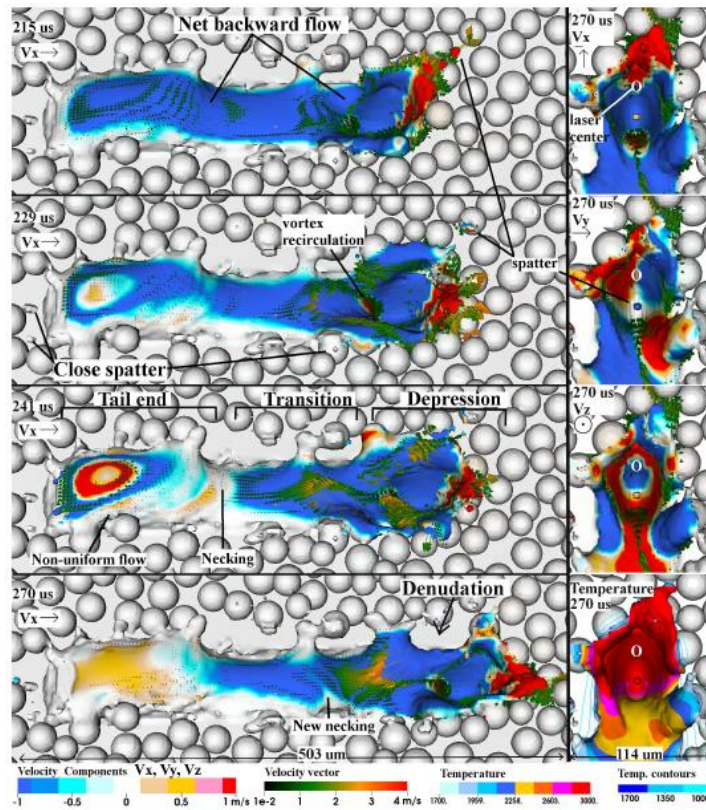
Figure 21. Simulation from melt pool flow progress as a function of time. (Khairallah et al. 2016).

5 THE EFFECT OF PROCESS PARAMETERS ON SPATTERING

Most of parameters used in PBF are strongly interdependent and are mutually interacting, for example laser power, scanning speed and laser spot diameter are affecting to the volume energy density (VED). Melt pool stability and laser beam, which creates vapor vortex, have the most influence to the spattering phenomena.

Process parameters can be sorted into four categories: laser parameters (laser power and spot size), scan parameters (scan speed, -spacing and –pattern), material parameters (particle shape, -size, -distribution, powder bed density, layer thickness and material properties) and process gas parameters (used gas, gas pressure and gas flow). (Gibson et al. 2010, pp.7.)

5.1 Laser parameters

DMLS process is based on complete melting of powder. High quality, high power and small spot size are required qualities of the laser beam, because with small high quality beam it is possible to achieve more precise tolerances to the build parts. Based on these qualities, most commonly used laser type in PBF process is water cooled 1064 nm ytterbium-fiber laser and because metallic materials have high absroption for 1064 nm wavelength. Spot diameter defines the area which is rapidly heated and melted. (Gunenthiram et al. 2018.) Laser beam profile analysis from ytterbium-fiber laser is shown in figure 22.
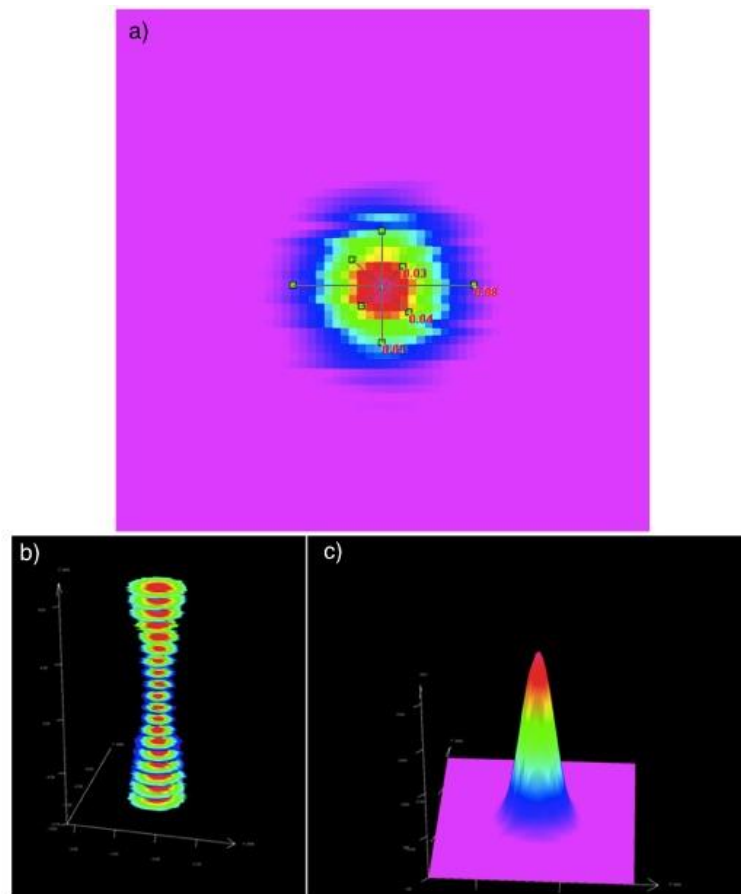
Figure 22. a) False color image of laser beam diameter from focus point. b) Isometric 3D image is measured from +-9 different levels from focus point at 1mm steps. c) An 3D model of laser beam shape in focus point. (Ophir, 2018).

Typically, focused spot diameter in DMLS machines is 80 μm (which can be seen in figure 22a). When laser spot diameter increases, also the melt pool size increases, because heat input is now distributed over a larger area and therefore the amount of heat input per area decrease. Laser power along scanning speed, beam diameter and hatch distance determine the heat input which defines the amount of melted and vaporized powder. Increasing laser power will increase the velocity of the melt pool flow and therefore vapor vortex size. Melt pool flow has correlations with Marangoni convection which causes recoil pressure driven spattering and vapor vortex causes entrainment driven spattering. (Gunenthiram et al. 2018.)

5.2 Scanning parameters

Scanning pattern in DMLS processes is implemented with sequentially scanned stripes which rotate with pre-defined strategy. The stripes are primarily used with metal parts to minimize residual stress. In commonly used scanning strategy for metallic materials the laser beam turns on and off in every stripe, and in the start and end point laser beam creates a different type of spattering because it takes time to form a keyhole. Scanning speed and laser power is used to calculate VED. When the scanning speed increases the melt pool length extends and the melt pool becomes unstable. When high scanning speed is used, VED decreases and melt pool becomes shallower which can lead to balling effect. Balling effect is a result of low heat input and is shown in figure 23. Vapor vortex moves faster when high scanning speed is used on the surface of the powder bed which increases entrainment spattering and denudation. The laser beam heats the shield gas flow rapidly creating vapor jet, which causes entrainment spatters. When the vapor jet forms it creates a low pressure zone near the melt pool and depending on the pressure, denudation zone size varies. (Gibson et al. 2010, pp.123 & Gunenthiram et al. 2018.)
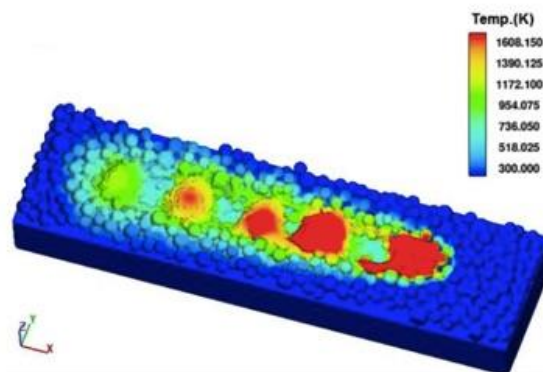
Figure 23. 3D simulation of balling effect. Used laser power is 200 W and scanning speed is 2300 mm/s. (Lee & Zhang, 2015).

5.3 Powder material

Powder bed density consists of particle size, shape and distribution of the powder particles. Absorption and powder bed thermal conductivity depends on powder bed density. Particles have different shape based on how they are manufactured. For example, water atomized particles (which can be seen in figure 24a) are randomly formed and gas atomized particles (which can be seen in figure 24b) are evenly round-shaped as shown in figure 24.
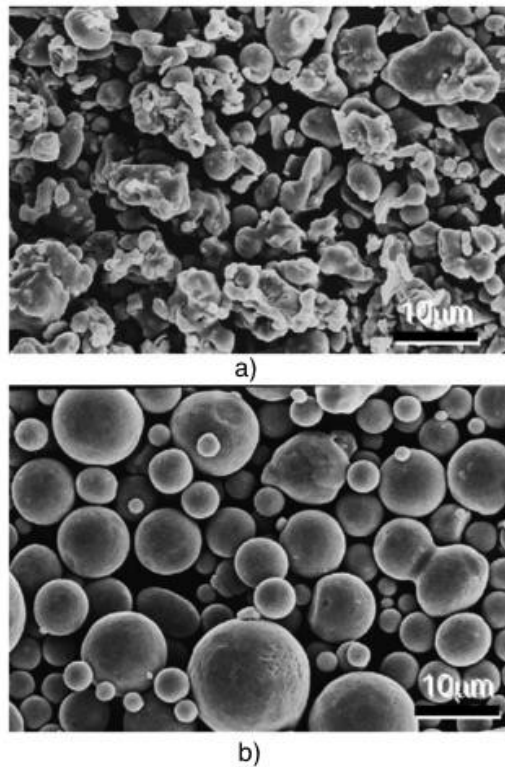
Figure 24. a) Micro structural image of a water atomized 316L stainless steel powder and b) gas atomized 316L stainless steel powder, both imaged with SEM. (Koseski et al. 2005).

Smaller powder particles have larger surface area and it absorbs laser power more efficiently, which helps laser to melt more material with the same power than larger particle size. Melted track is smoother with smaller particles than larger ones because of their smaller volume than larger particles and they are completely melted. Simulation of the influence of different particle size to the melt track is shown in figure 25.
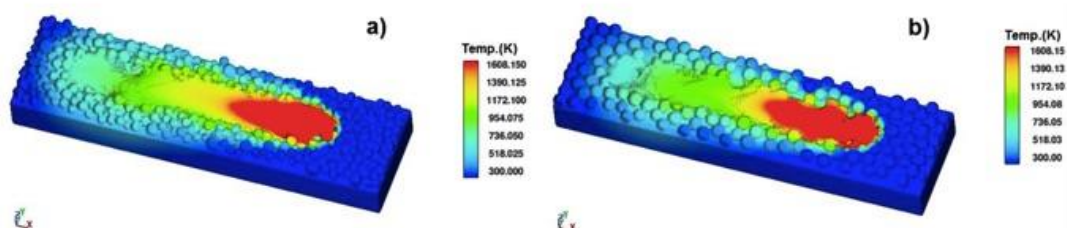
Figure 25. a) Simulated track with small particle size. b) Simulated track with larger particle size. The used parameters are laser power = 200 W and scanning speed = 1100 mm/s. (Lee & Zhang, 2015).

According to (Lee & Zhang, (2015) when the powder bed is dense it is possible to build parts with better surface quality. Melt pool fluid flow and heat conduction is different when using different packing density powders. This changes the melt pool fluid flow, which changes the spattering because the process changes between keyhole and conduction mode. Higher packing density reduces down direction fluid convection, which decreases balling defects and voids. Powder density effect to the melt track is presented in figure 26. The quality of the part depends on the chemical composition of the powder material. For example, high oxygen level in powder increases the number of spatters and pores.
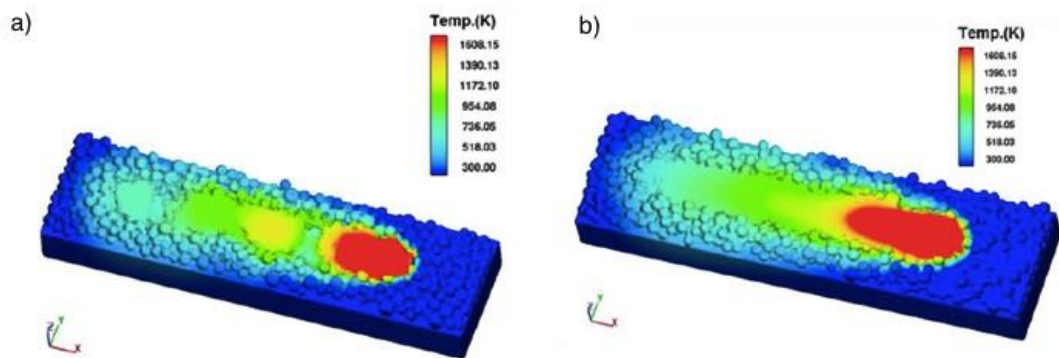
Figure 26. a) 3D simulation of powder density (38 %) effect to the melt track and b) with powder density of 45 %. (Lee & Zhang, 2015).

5.4 Process gas parameters

Purpose of the inert gas flow is to protect melt pool from oxidation and remove the condensate and by-products which are produced by the melting process. Removing the condensate is important because it will absorb the laser beam energy, which reduces the intensity of the spot. Beam can also scatter when the condensate cloud is in the path of the laser. This increases the size of the laser beam, which creates larger melt pool. Ideal gas flow type is laminar flow, which is identical in the entire building platform. According to Ferrar et al (2011), gas flow is not identical in every location on the platform, because of the machine flow nozzle and used gas flow speed. That changes significantly the part porosity and strength properties. Laser beam created welding plume and condensate is presented in figure 27. Building chamber is filled with inert gas (argon or nitrogen) depending on process material.
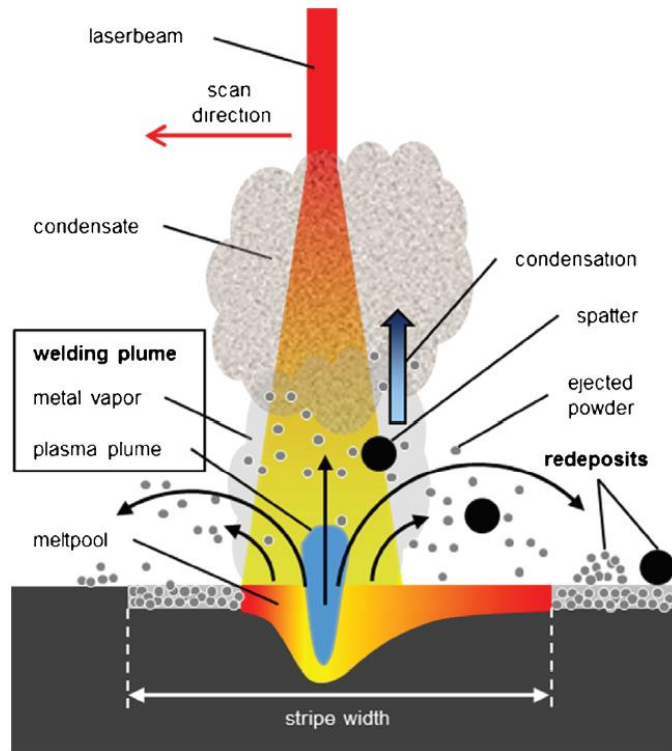
Figure 27. Schematic of powder bed fusion process by-products. (Ladewig at al. 2016).

Based on research of Matthews et al. (2016), inert gas pressure controls the vapor flux created by the melt pool. In lower gas pressures (under 50 Torr) the vapor jet expands into a wide plume (which can be seen in figure 28b). In high gas pressures (over 100 Torr) vapor jet is narrower than with the low gas pressures (which can be seen in figure 28a). Depending on gas pressure in the building chamber, particle distribution changes in the Bernoulli effect-driven denudation zone. (Ferrar et al. 2011 & Matthews et al. 2016.)
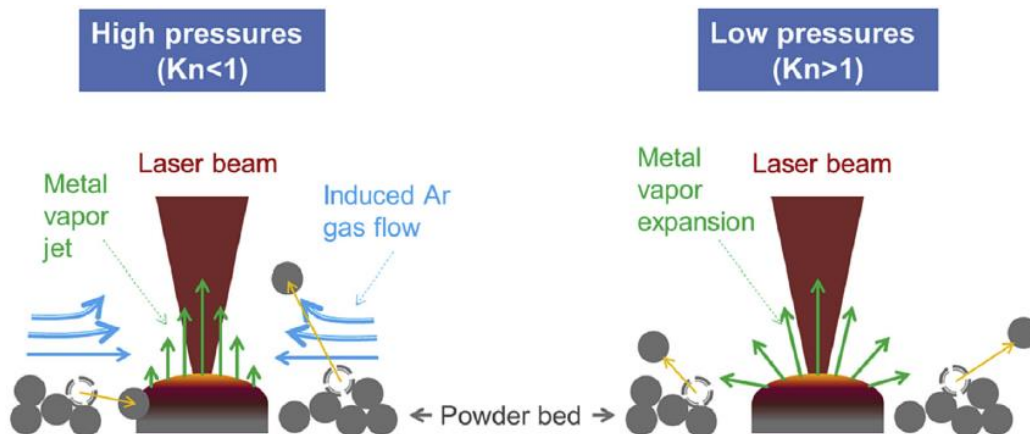
Figure 28. Schematic of the metal vapor jet shape depending on surrounding argon gas pressure. (Matthews et al. 2016).

6 EXPERIMENTAL PART

The experimental part of this thesis was conducted to define, design and manufacture a suitable spatter analysis system for DMLS process. This system is custom made as this kind of analysis systems is not commercially available at the moment. The aim of this experimental part is to test the designed spatter analysis system by measuring spattering from different locations on the platform, parameters and materials. Experimental part consist of choosing suitable hardware (camera, optics, illumination and protecting enclosure), design and manufacture of custom made set-up (zero-point mounting system and linear rail), analysis software development in collaboration with Oseir Ltd (Osirec spatter analysis software), experimental set-up (installation of hardware and manufactured mounting system inside of the M 290) and experimental procedure (image and analysis procedure).

The hardware was created specifically for the machine vision camera based spatter analysis system. Suitable measuring system for spatter analysis did not exist. That is why it was designed specifically for this thesis. The design process of the hardware followed Design for Manufacture and Assembly procedure (DFMA), which means cost effective manufacturing and ease assembly.

6.1 Materials

Two different metal powder materials were used in this thesis: 316L (iron-based stainless steel) and MP1 (cobalt-chrome-molybdenum-based steel alloy). 316L is generally considered as very splashy process whereas process of MP1 is considered as clean process. Both materials are commonly used in AM and this is why their spattering behavior was monitored.

EOS StainlessSteel 316L is an iron-based alloy for parts that are required high ductility and corrosion resistance. 316L is commonly used in watch and jewelry, orthopedics and aerospace mounting parts. Material meets the requirements of the ASTM F138. (EOS, 2018b) More specific information about EOS, for example build volume, density, surface roughness and mechanical properties of build part can be found from appendix II (Material

data sheet EOS StainlessSteel 316L). Watch case made from EOS 316L is shown in figure 29.

Figure 29. Example part made from EOS 316L. (EOS, 2018d).

EOS CobaltCrome MP1 is a cobalt-chrome-molybdenum-based super alloy for parts that are required high strength, temperature and corrosion resistance. MP1 is commonly used in biomedical and high-temperature engineering applications. Material meets the requirements of the ISO 5832-4 and ASTM F75. (EOS, 2018b) Fuel injector made from EOS MP1 is shown in figure 30. More specific information about EOS MP1, for example build volume, density, surface roughness and mechanical properties of build part can be found from appendix III (Material data sheet EOS CobaltCrome MP1).

Figure 30. Example par made from EOS MP1. (EOS, 2018c).

6.2 EOS M 290 Direct Metal Laser Sintering system

The machine used in experiments was EOS M 290 introduced in (Figure 31). M 290 is a high-quality industrial laser sintering machine. Direct metal laser sintering system has a 400 watt ytterbium-fiber laser and the system has a building volume of 250 x 250 x 325 mm. Process laser wavelength is 1060-1100 nm and focus diameter 100 μm. M 290 has an extensive material range in metallic material. EOS monitoring suite is available for EOS M 290 including EOSTATE MeltPool, EOSTATE Exposure OT, EOSTATE System and EOSTATE PowderBed monitoring systems. More specific information about M 290 can be found from appendix IV (EOS M 290 data sheet).

Figure 31. EOS M 290 Direct Metal Laser Sintering system. (Pddnet, 2018).

7 CHOICE OF THE SUITABLE HARDWARE FOR CAMERA SYSTEM

7.1 Machine vision camera

High quality image analysis software needs at least 2 megapixel resolution images to work properly, the reason for high resolution is that a detected single particle should illuminate at least 5 pixels for high quality spatter detection and size measurement. The hardware assembly should be as small as possible, because of the limited space inside of the M 290 building chamber. Space limitation of the machine is shown in figure 32.
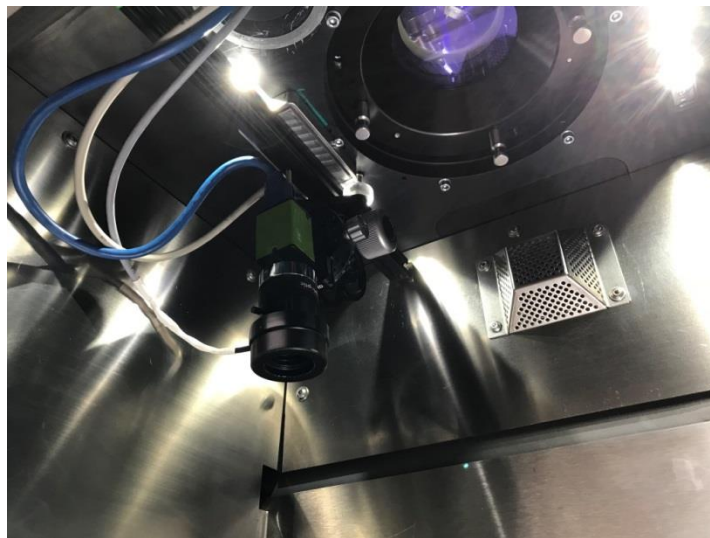
Figure 32. Image of the measurement system inside the building chamber.

The physical size of camera needs to be less than 40 x 40 x 50 mm. High frame rate is also needed to detect fast moving small particles. These requirements made the choosing of the camera difficult. Frame rate is not necessarily describing all properties of the camera, especially when the machine vision camera is considered because machine vision cameras have much better resolution when compared to high speed cameras. The machine vision cameras are suitable for online measurements, unlike high speed cameras because they do not need memory card buffer for images. Difference between high speed camera and machine vision camera is shown in table 2.

Table 2. Comparison table of high speed and machine vision cameras.

Camera type	High speed	Machine vision
Sensor	CMOS	CMOS
Resolution	1280 x 1024	2464 x 2056
Frame rate	1800	74
Pixel size [µm]	5.6	3.45
Color depth	12-bit	12-bit
Data transfer	RAM	USB3.0
Size [H x W x D]	73 x 73 x 82.5	29 x 29 x 41.5
Record time	4.2 s	10 h

First experimental set-up was based on Flir Grashopper3 GS3-U3-23S6M-C CMOS machine vision camera build-in with Sony IMX174 2.3 megapixel monochrome sensor shown in figure 33. Sensor resolution is 1920 x 1200 and pixel size 5.86 µm. More specific information about the camera, for example about the frame rate and quantum efficiency can be found from appendix V (GS3-U3-23S6M-C data sheet).

Figure 33. Flir GS3-U3-23S6M-C machine vision camera. (Ptgrey, 2018).

JAI-GO was selected for system development phase because of the small physical size (29 x 29 x 41.5 mm), high resolution (2464 x 2056), small pixel size (3.45 µm), 12-bit output and relative high frame rate (8-bit / 74 fps). Further tests based on JAI-GO 5100M CMOS machine vision camera shown in figure 34. More specific information about the camera for example quantum efficiency can be found from appendix VI (JAI-GO-5100 data sheet).

Figure 34. JAI-GO-5100-USB machine vision camera. (Opli, 2018).

7.2 Optics for machine vision camera

Glass-material optical lenses are not optimal for the purpose: they are not perfectly homogenous or coatings are not formed perfectly on lens, optical wave front can chance and it has huge effect on image quality. (TelescopeOptics, 2018). The selected lens for the first test set-up was Schneider Xenoplan 1.9/35-0901 shown in figure 35, because it meets the optical quality requirements that are determined by the used camera and the work distance is suitable for the measurement system installation. The spectral range of the lens is from 400-1000 nm making it suitable for used active illumination which operating wavelength is 802 nm. Lockable focus and iris setting mechanism make it reliable in use, because focus cannot be changed by itself when machine is active in use. More specific information about lens can be found from appendix VII (Schneider Xenoplan 1.9/35-0901 data sheet).

Figure 35. Schneider Xenoplan 1.9/35-0901 3 Mega-Pixel lens. (Bockoptronics, 2018).

When the first test was executed, it was noticed that the focus needs to be able to be changed while the machine is running. This is impossible with mechanical focus lens without stopping the process, because the measurement system was placed inside of the building chamber and the atmosphere conditions would have been lost. Due to this Varioptic Caspian C-39N0-250 liquid lens was chosen for the second test series, because it has electrically controllable focus and focus change is possible without opening building chamber.

The desired properties of the optics were high quality, variable iris, electronically controllable focus and a small physical size. Small physical size was needed because the protecting enclosure has a physical size limitation for the camera. It was impossible to adjust the focus without opening protecting enclosure and building chamber. That was one reason why the lens with electronically controllable focus was chosen. The second reason why the lens with electronically controllable focus was wanted was that every user had a different view of focus. The idea was to minimize measurement errors from different focus planes, make it more user friendly and efficient when measuring different levels. Suitable optics for the prototype was found from the company Varioptic. Caspian C-39N0-250 shown in figure 36 was selected to fulfill desired properties. More specific information about the selected lens can be found from appendix VIII (Varioptic Caspian C-39N0-250 data sheet).

Figure 36. Caspian C-39N0-250 liquid lens. (BrilliantOptics, 2018).

7.3 Protecting enclosure for the machine vision camera

When the camera system is installed inside the machine, it needs protective housing against metal powder dust. Dust accumulates on the lens and connectors without proper enclosure enabling the risk of short-circuiting. The protecting enclosure is manufactured and machined from aluminum because light weight was wanted. The protective housing is specially designed for JAI-GO series machine vision cameras and is shown in figure 37.

Figure 37. autoVimation Colibri IP66 (Nema4) Industrial Camera Enclosure. (autoVimation, 2018).

When installing the camera system inside the building chamber, the volume of used space is critical. The camera enclosure cannot be installed in the path of the laser beam. The desired properties of the protective housing are small physical size, IP66-protection, anti-reflective coating on lens and high quality, protective housing lens has influence to the image quality. Gas nozzle and the possibility of 90° deflection mirror installation added extra requirements for the protective enclosure. The autoVimation Colibri IP66 (Nema4) Industrial Camera Enclosure shown in figure 37 was the best option for this measurement system due to its smallest physical size and the best qualities of all the protective enclosures commercially available. More specific information about Colibri can be found from appendix IX (Colibri IP66 (Nema4) Industrial Camera Enclosure data sheet).

7.4 Illumination laser

Airborne particles, which do not emit light of their own, need to be illuminated before camera system can see them. Suitable illumination source for this application is laser, because with laser illumination it is possible to achieve high-intensity illumination and precise timing for adjustable pulses.

The desired properties of the illumination are pulsed laser source, freely adjustable pulse sequence and number, small physical size and enough pulse energy (0.5 mJ-2.5 mJ), because small high speed particles need several light pulses on single image before speed is possible to calculate and illumination need to have high enough intensity so that the camera can detect the illuminated particles. Requirement for small physical size comes from the hardware installation location in M 290 machine. Suitable laser was found from Oseir Ltd. HiWatch Compact laser shown in figure 38 was selected for test and prototype. More specific information about HiWatch can be found from appendix X (HiWatch data sheet).

Figure 38. Oseir HiWactch illumination laser. (Oseir, 2018).

7.5 Custom-made mounting set-up

The custom-made set-up consists of zero-point mounting system, linear rail, enclosure fitting and protective housing for the camera and the lens. The set-up was designed and built because there was no commercially available set-up for camera based measurement system. All of the parts are presented more specifically in figure 39. Some of the parts, for instance camera enclosure and linear rail were stock products.

Figure 39. Custom made mounting system.

Custom made zero-point mounting system was designed for machine vision based spatter analysis system hardware because there are no commercially available suitable mounting systems for EOS 290 machine. Mounting possibilities are limited inside EOS M 290 machine because of the process laser T-Theta lens and the path of the process laser beam. Fasteners were to keep as small as possible to ensure maximum camera movement without compromises on quality. Zero-point mounting system was designed for modified Colibri Compact series camera housing made by autoVimation. Zero point fasteners were chosen to minimize user-specific differences in hardware installation between different M 290 machines. 3D image of zero-point mounting system is shown in figure 40.
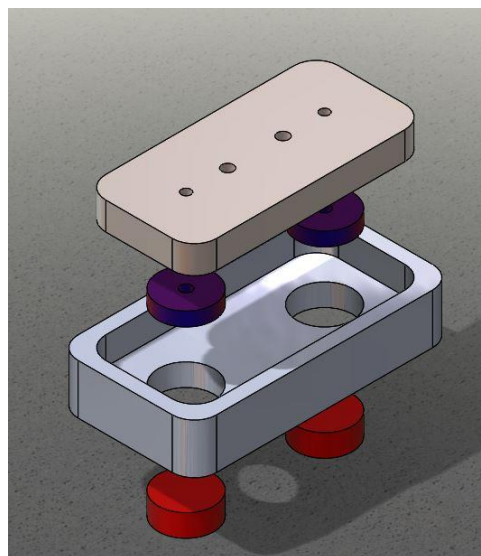
Figure 40. Specially designed zero-point mounting system of spatter analysis system for EOS M 290 machine.

Linear rail was purchased for enabling linear movement of the camera inside of the building chamber. Desired qualities of the linear rail were compact in design, manufactured of non-ferromagnetic material, high reliability and sealing against the powder dust. SKF LM miniature rail system was the best option on the markets, but had 16-week delivery time from purchase and this is why a similar product was needed to replace this. Therefore, Drylin T rail was purchased for this measurement system, it is shown in figure 41.

Figure 41. DryLin T linear rail system.

Mounting system for the camera enclosure was designed by using the measurements of the linear rail. This enclosure fitting was designed and manufactured in EOS Finland Oy. The fitting was printed from aluminum alloy to ensure light weight and durability without compromising functionality. It was printed because the part has several features that are impossible to manufacture with conventional machine. The enclosure fitting is shown in figure 42.
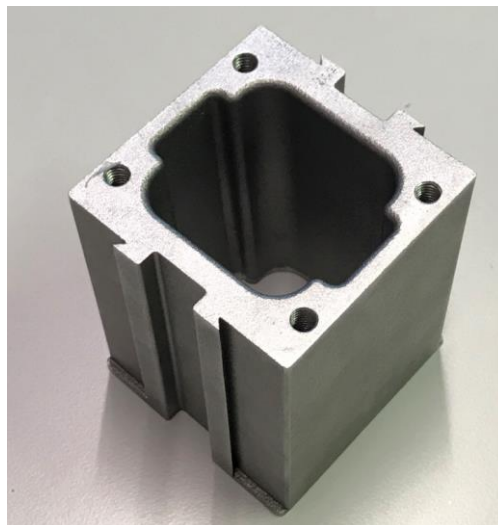
Figure 42. Printed aluminum alloy enclosure fitting.

8   ANALYSIS SOFTWARE DEVELOPMENT

There was no suitable analysis software available for this purpose, so it had to be developed specially for this spatter analysis system. Software called Osirecs by company Oseir was chosen after it was made sure that the analysis software fulfils Electro Optical System's specific requirements for the spatter analysis system. The Osirec software analyses captured images and Osirec calculates the melt pool dimensions, amount, speed and direction of the number of hot and cold particles in the front and back sectors. The measurements data acquired and the information received are used to monitor the process, and for better understanding of the spattering phenomena. The calculations in the Osirec software are based on National Instruments LabVIEW image processing library algorithms. The calculated data is exported to computer hard drive in html-format which includes histogram images. The data can be post-analyzed in excel or in Minitab for deeper statistical analysis. Analysis software user interface is shown in figure 43.
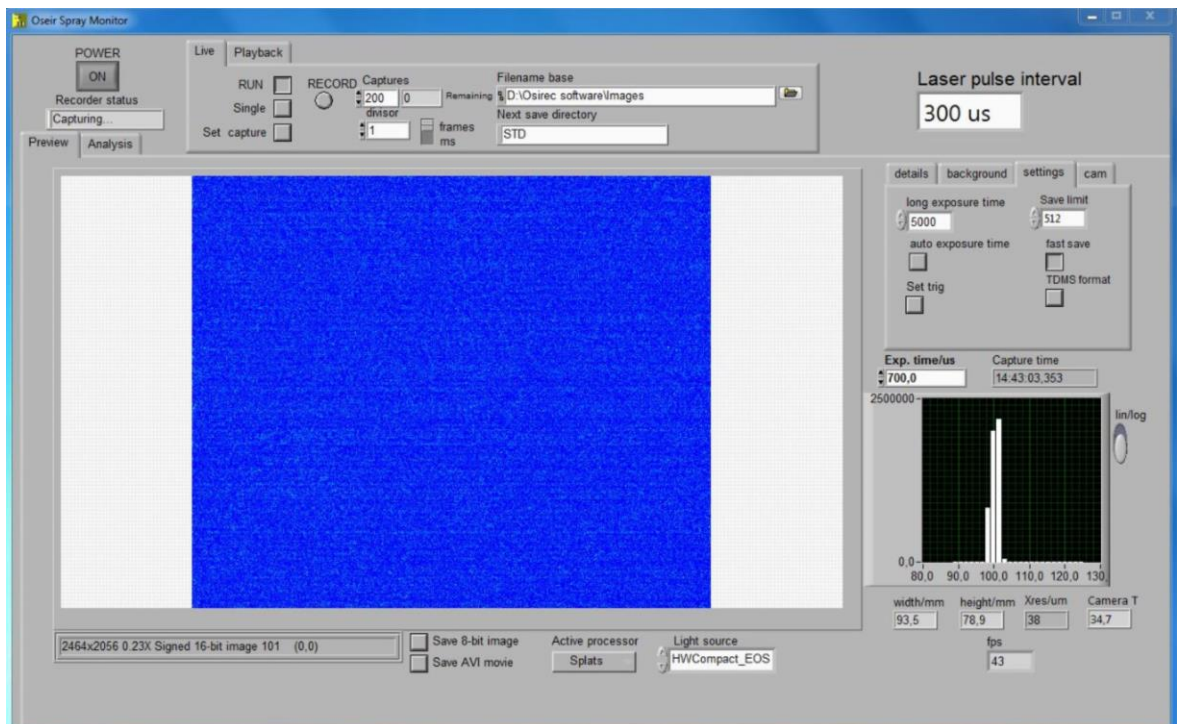
Figure 43. Osirec analysis software user interface.

9   EXPERIMENTAL SET-UP

The assembly of the measurement system constitutes of zero-point mounting system, linear rail system, enclosure fitting and camera enclosure. The zero-point mounting system consists of two parts: the one part (part a in figure 44) is attached to the roof of the building chamber permanently, and the other part (part b in figure 44) is attached in the middle of the linear rail. Enclosure fitting is attached to the sled of the linear rail and the camera enclosure can be attached to it. This system enables measurement system removal from the building chamber without changing the field of view in the platform. Measurement system assembly is shown in figure 44.
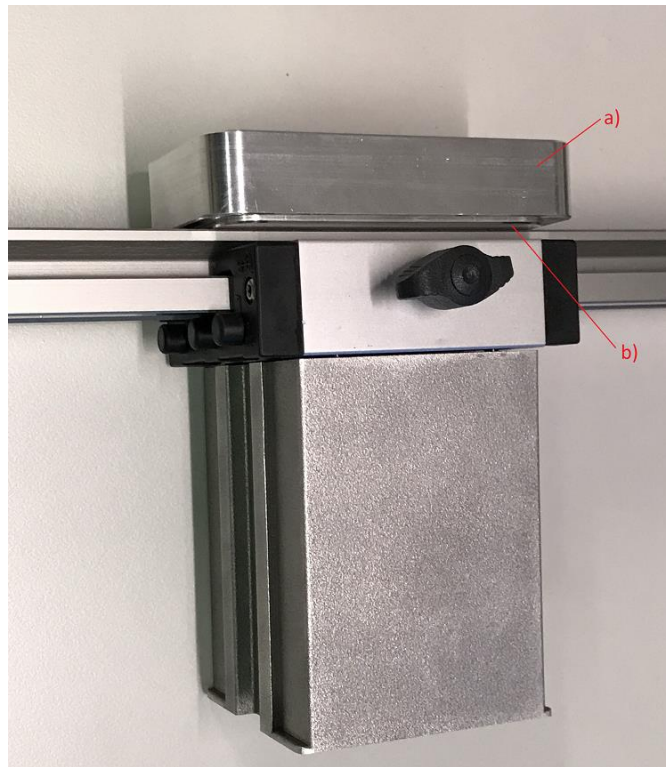
Figure 44. Measurement system assembly.

10 EXPERIMENTAL PROCEDURE

The experimental part consists of image and analysis procedures. The camera hardware set-up, illumination laser installation and software analysis set-up needed to be conducted before imaging. The camera hardware set-up consists of the camera and lens installation to the linear rail mount, focusing the camera to the currently imaged level and choosing the optimal location for the camera from front, middle or back sector. Active illumination laser is adjusted to the same level as the focus of the camera.

The lens is focused to the right level by using a special made depth of field target. The same target is used to calibrate the illumination laser to the same level. When the camera and the illumination laser are in the right position, test target can be removed from the building chamber. After this the machine can be prepared for the printing process. Set-up of the imaging is shown in figure 45.
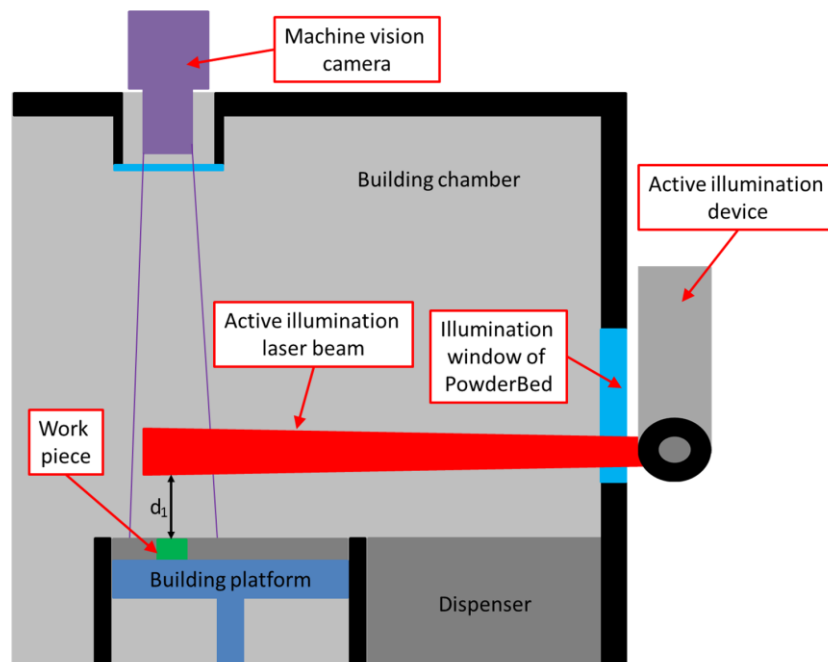
Figure 45. Schematic of the camera installation and illumination laser level calibration inside of EOS M 290.

10.1 Image procedure

Image procedure consists of 200 images taken from single layer, and from ten different layers (total 2000 images). The images are saved to the computer hard drive before the analysis procedure. The user can choose if the images are analyzed or turned into a video with Osirec. If the analysis part is chosen, the software calculates statistics for spatters. Results can be used to make quantitative analysis by Excel or Minitab. These statistical analysis and videos give better understanding between spattering theories and phenomena. The imaging and analysis procedure are shown in figure 46.
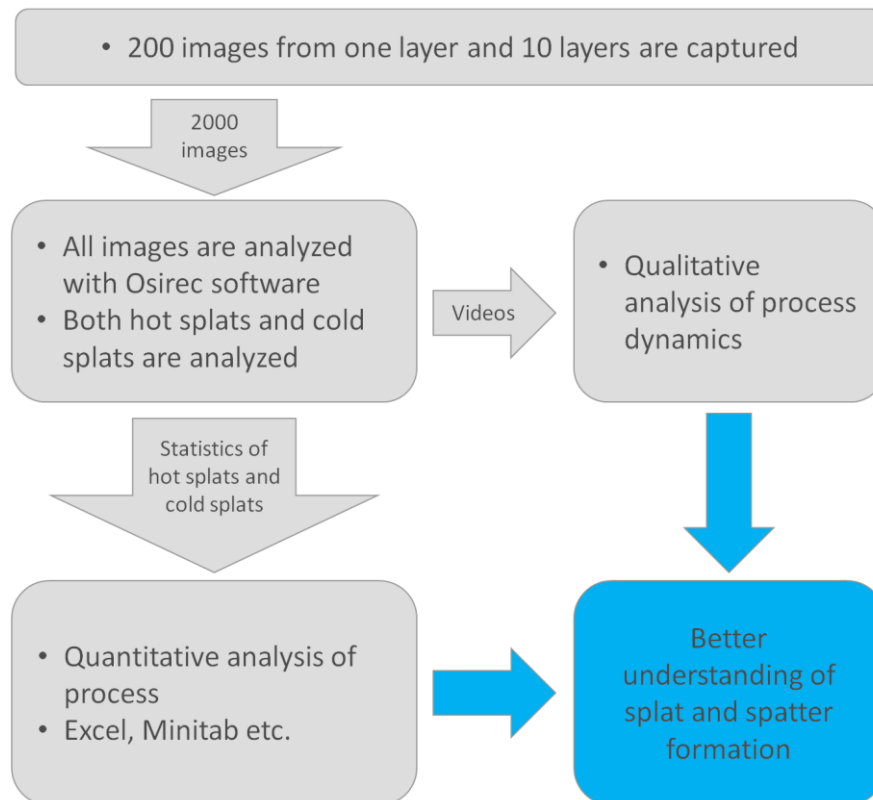
Figure 46. Schematic of image and analysis process with Osirec.

10.2   Parameters used in the test series I and II

Based on literature, it was noticed that laser power (LP) and scanning speed (SS) significantly changes the melt pool shape and stability and therefore the formation of spatters. Laser power was varied from standard process, from -35 % to -15 %, and from +15 % to +35 %, with 10 % steps. Scanning speed was varied from standard process from -50 % to -30 % and from +30 % to +50 %, with 10 % steps. Gas flow was kept constant in all of the tests to maintain the same atmosphere conditions in the chamber. The used parameters for test series I is presented in table 3 and 4 and parameters for test series II in table 5.

Table 3. Used parameters for 316 L in test series I

Parameter	Laser power [%]	Scanning speed [%]	Heat input [%]	Gas flow [%]
STD	100	100	100	100
LP +30 %	130	100	130	100
LP -30 %	70	100	70	100
LP +40 %	140	100	140	100
LP -40 %	60	100	60	100
SS +30 %	100	130	77	100
SS -30 %	100	70	143	100

Different test cases (LP and SS) are shown on the left side of the test matrices, table 3. These test cases were chosen to maximize the variation in heat input by changing laser power. Abbreviations used in table 3; standard parameters (STD) for 316 L*,* laser power (LP plus/minus) from standard parameter, scanning speed (SS plus/minus) from standard parameter. Heat input is calculated with equation 1.

$$EOS\ VED = \frac{P}{V_s * L_t * H_d} \tag{1}$$

In equation 1 *EOS VED* = Volume Energy density (J/mm^3), *P* = laser power (W), V_s = scanning speed (mm/s), L_t = layer thickness (mm), H_d = hatch distance (mm).

Table 4. Used parameters for MP1 in test series I

Parameter	Laser power [%]	Scanning speed [%]	Heat input [%]	Gas flow [%]
STD	100	100	100	100
LP +15 %	115	100	115	100
LP -15 %	85	100	85	100
LP +25 %	125	100	125	100
LP -25 %	75	100	75	100
SS +30 %	100	130	80	100
SS -30 %	100	70	148	100

Different test cases (LP and SS) are shown on the left side of the test matrices, table 4. These test cases were chosen to maximize the variation in heat input by changing laser power. Abbreviations used in table 4; standard parameters (STD) for 316 L, laser power (LP plus/minus) from standard parameter, scanning speed (SS plus/minus) from standard parameter. Heat input is calculated with equation 1.

Table 5. Used parameters for 316L in test series II

Parameter	Laser power [%]	Scanning speed [%]	Heat input [%]	Gas flow [%]
STD	100	100	100	100
LP +15 %	115	100	115	100
LP -15 %	85	100	85	100
LP +25 %	125	100	125	100
LP -25 %	75	100	75	100
LP +35 %	135	100	135	100
LP -35 %	35	100	65	100
SS +30 %	100	130	77	100
SS -30 %	100	70	143	100
SS +40 %	100	140	71	100
SS -40 %	100	60	167	100
SS +50 %	100	150	67	100
SS -50 %	100	50	200	100

Different test cases (LP and SS) are shown on the left side of the test matrices, table 5. These test cases were chosen to maximize the variation in heat input by changing laser power. Abbreviations used in table 5; standard parameters (STD) for 316 L, laser power (LP plus/minus) from standard parameter, scanning speed (SS plus/minus) from standard parameter. Heat input is calculated with equation 1.

10.3   Analysis procedure

When the images were saved to the computer hard drive, the analysis tab was opened from Osirec front page in playback mode. After this a pop up page for the selection of the images for the analysis opened as shown in appendix XI (1) and the images were chosen for the analysis. The software started to calculate the melt pool related data (melt pool direction, melt pool length mm, melt pool width mm and melt pool width divided by length ratio (L/W)), when the melt pool tab was opened in playback mode, as shown in appendix XI (2). The software calculated hot spatter relative intensity, hot spatter speed (m/s) and hot spatter direction compared to melt pool direction in the next tab as shown in appendix XI (3). The software calculated cold spatter speed (m/s) and direction compared to gas flow direction in the third tab, as shown in appendix XI (4). In the fourth tab the software calculated image statistics for hot and cold spatters, as shown in appendix XI (5). The software collected user information about the imaged and analyzed job. The data was exported to a selected file folder on the computer hard drive in the fifth tab as seen in appendix XI (6).

11 RESULTS AND DISCUSSIONS

The reliability of the measurement system was tested with images taken from different numbers of layers to be assured that the measurements can be repeatable and the results are comparable to each other. Based on investigations mean per image value, standard deviation (STD) and variation (VAR) value are large with five measurement repeats, which make the measurement results unreliable. Mean per image STD and VAR value are in the limits of acceptance with 10 and 20 repeats. Therefore, the number for repetition in the measurements was chosen to be 10. STD and VAR values for different number of repeats are shown in figure 47.
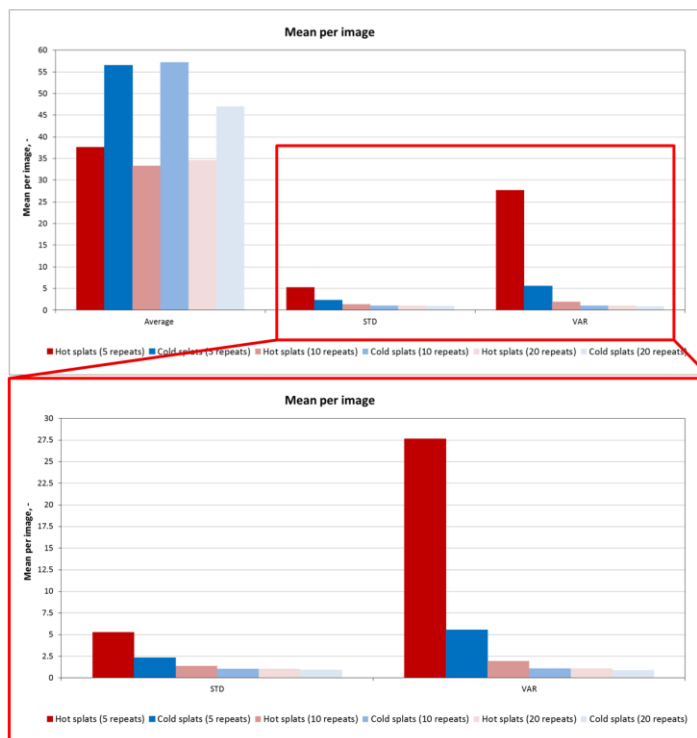
Figure 47. Amount of imaged layers' impact to the standard deviation and variation.

11.1 Test series I

Test series I was carried out with Flir machine vision camera using Schneider optics. The camera was focused 15 mm above the powder bed. The illumination laser sheet was calibrated to the same level. The purpose of test series I was to test different laser power values and scanning speeds effect to the spatter mean per image and spatter mean speed value. The test was carried out by using two different materials (EOS 316 L and MP1) and used machine was EOS M 290. Test series I consists of seven different test cases which can be found from table 4. The test position was on left down corner of the building platform, viewed from the door of the building chamber.

11.1.1 Mean per image

The mean per image number corresponds to how many observations there are on average in each image. Heat input correlation to the mean per image was tested with both materials, 316 L and MP1, in test series I. Heat input was calculated using equation 1. Mean per image number of hot- and cold spatters was analyzed for 316 L and MP1 and compared to the heat input, laser power and scanning speed. Results are presented in figure 48, 49 and 50.

Figure 48. Mean per image value for 316 L and MP1 using different heat input.

The mean per image number of hot and cold spatters decreases as the heat input decreases with both of the materials (which can be seen in figure 48). This can be explained by the increasing recoil pressure driven spattering (spatter type I) when the heat input increases. The camera spatter analysis system captures images above the building platform and therefore the spatters flying straight towards the camera cannot be detected. When the heat input increases, the vapor vortex around the laser beam increases, and vortex turns the flight direction of cold entrainment driven spatters and therefore the amount of cold spatter detections has variation. It was noticed that 316 L has more hot spatters and less cold spatters than MP1. Therefore, it can be concluded that there are differences between metal powder material types.
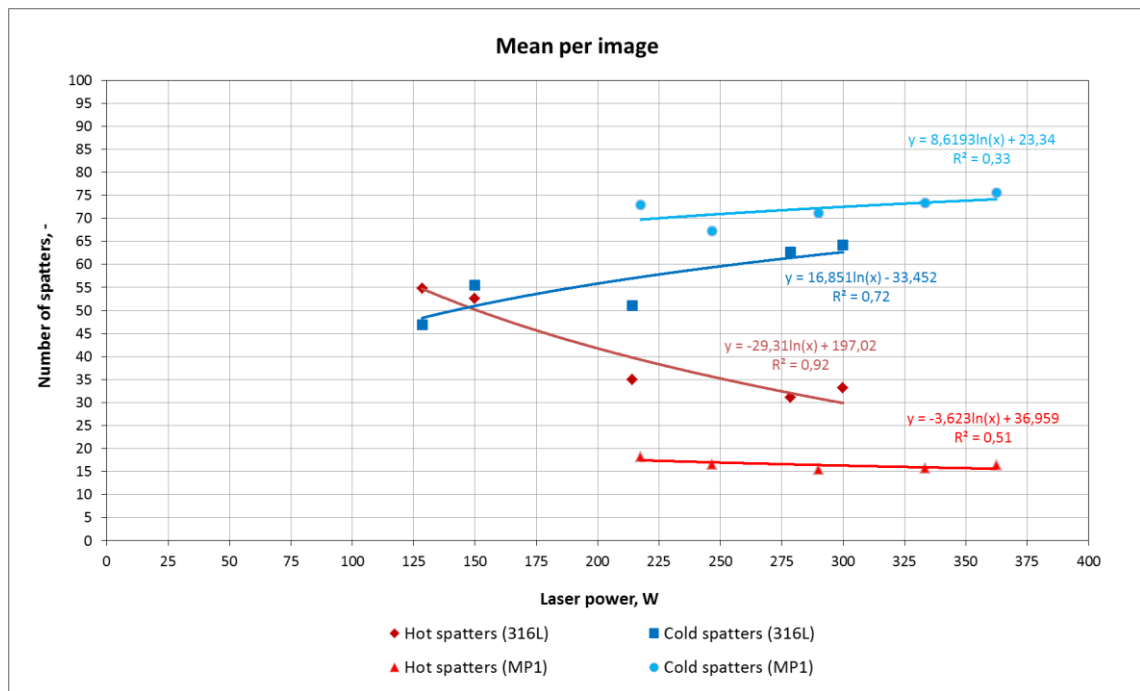
Figure 49. Mean per image values for 316 L and MP1 using different laser power.

The mean per image number of hot spatters decreases as the laser power increases with both materials (which can be seen in figure 49). It can be concluded that the laser power correlates to the number of detected hot spatters when using 316L with R^2 value 0.92. The number of detected hot spatters decreases as the laser power increases, because the forces causing recoil pressure driven spatters increases. Recoil pressure driven spatters fly upwards and our current measurement system cannot detect the spatters flying in direction

straight up. It cannot be concluded that laser power correlates to the number of hot spatters when using MP1. According to statistics R^2 value is 0.51.

The number of cold spatters increases as the laser power increases with both materials (which can be seen in figure 49). It can be concluded that the laser power correlates to the amount of detected cold spatters when using 316L, because R^2 value is 0.72. Mean per image number for the cold spatters of 316 L increase as the laser power increases, because the vapor vortex causing entrainment driven spatters increase. According to statistics laser power does not correlate to the number of cold spatters when using MP1 R^2 value is 0.33.
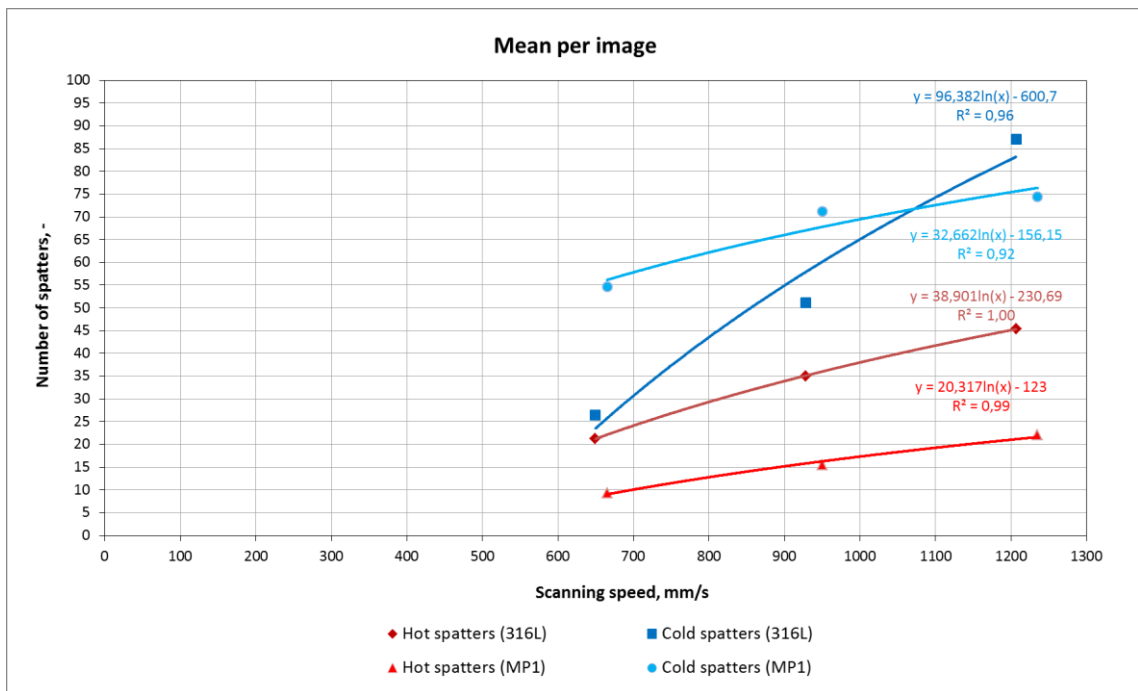
Figure 50. Mean per image value for 316 L and MP1 using different scanning speed.

The number of hot spatters increases as the scanning speed increases with both materials (which can be seen in figure 50). It can be concluded that the scanning speed correlates to the amount of detected hot spatters when using 316L and MP1, with R^2 value 1.00 for 316L and 0.99 for MP1. The number of detected hot spatters increase as the scanning speed increases, because when using high scanning speed, the melt pool becomes longer and narrower, which increases recoil pressure and Marangoni driven spattering (spatter type II). Recoil pressure driven spatters fly upwards and our current measurement system cannot detect the spatters flying straight towards the camera.

The mean per image number of cold spatters increases as the scanning speed increases with both materials (which can be seen in figure 50). It can be concluded that laser power correlates to the amount of detected cold spatters when using 316L and MP1, with R^2 value 0.96 for 316 L and 0.92 for MP1. Mean per image number of cold spatters increase as the laser power increases, because the vapor vortex causing entrainment driven spatters increase.

11.1.2 Mean speed

Mean speed value corresponds to how fast the hot- and cold spatters fly in the process. The correlation of heat input, laser power and scanning speed to the spatter mean speed was tested with both materials in test series I. Heat input was calculated by using equation 1. Mean speed of hot- and cold spatters was analyzed for 316 L and MP1 and compared to the heat input, laser power and scanning speed. Results are presented in figure 51, 52 and 53.
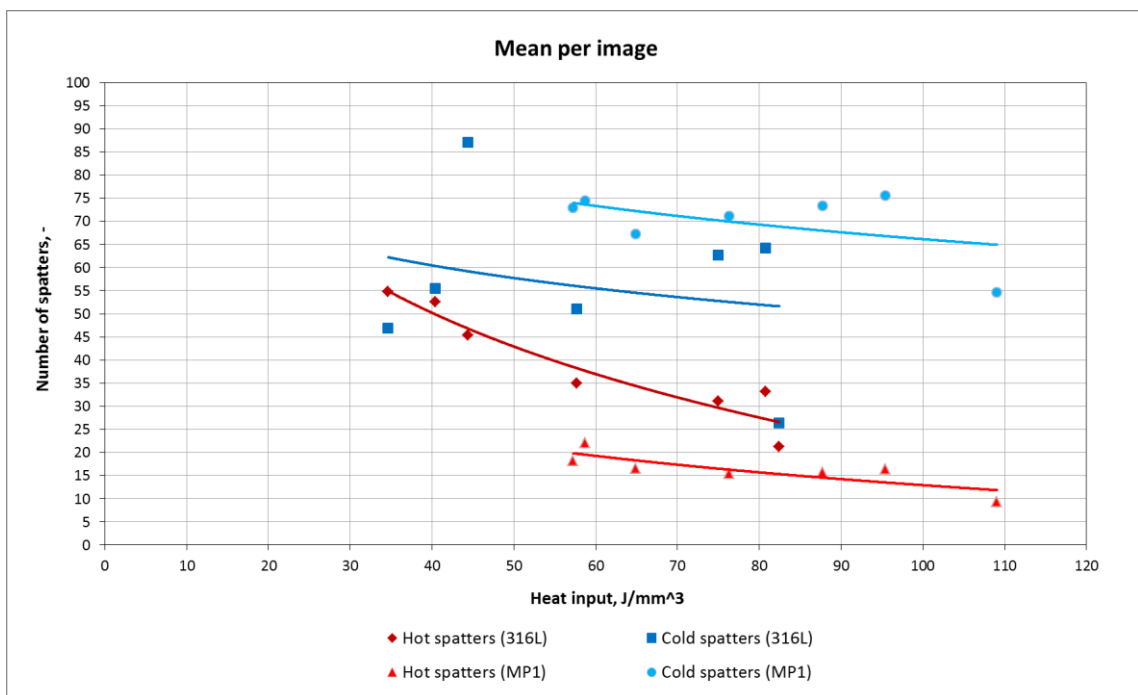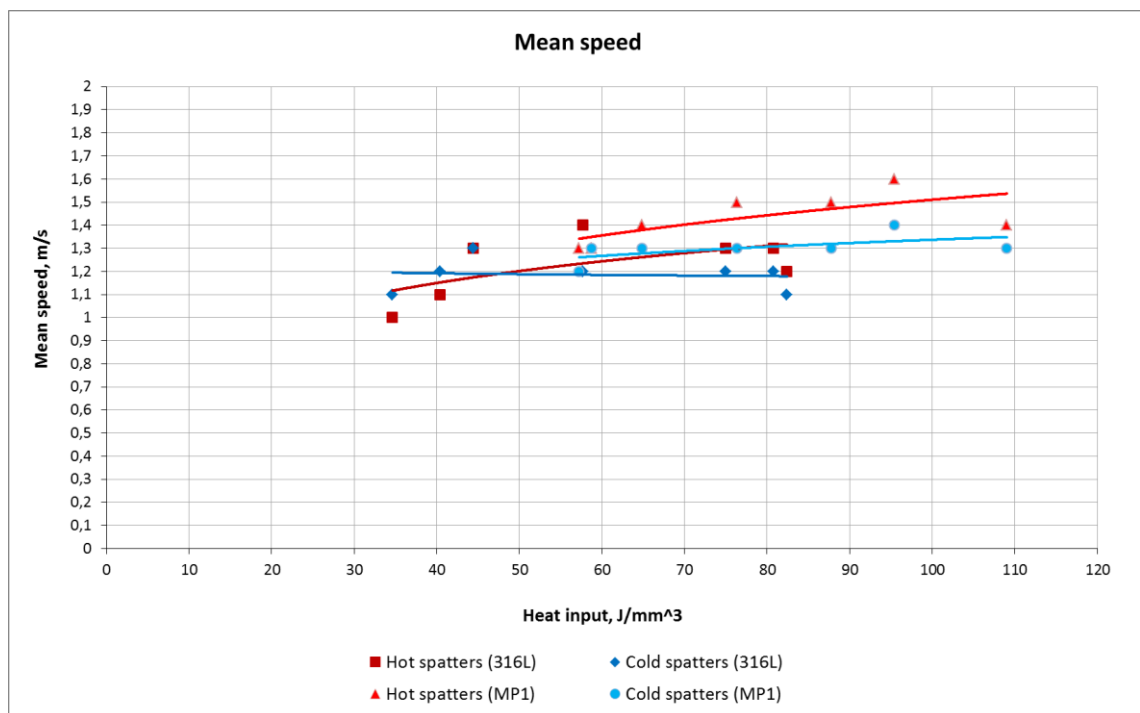

Figure 51. Mean speed of 316 L and MP1 hot and cold spatters when using different heat input.

The mean speed of hot spatters increases as the heat input increases with both materials (which can be seen in figure 51). This can be explained by the increasing forces that cause Marangoni effect and recoil pressure (spatter type II). The mean speed of cold spatters remains almost constant as the heat input increases with both materials (which can be seen in figure 51). This suggest that mean speed of cold spatters does not correlate to the heat input.
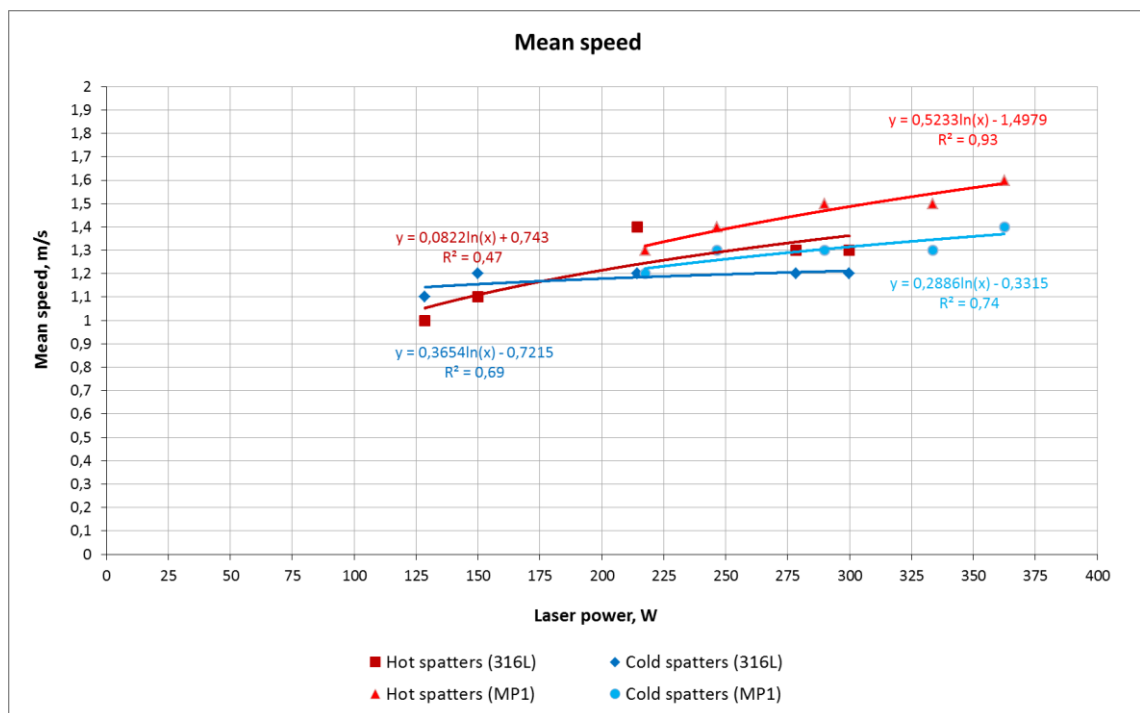
Figure 52. Mean speed of 316 L and MP1 hot and cold spatters when using different laser power.

The mean speed of hot spatters increases as the laser power increases with MP1 (which can be seen in figure 52). It can be concluded that laser power correlates to the hot spatters mean speed when using MP1 with R^2 value 0.93. Mean speed for MP1 hot spatters increase as the laser power increases, because forces causing Marangoni effect and recoil pressure (spatter type II) increase. It cannot be concluded that laser power correlates to the mean speed of hot spatters when using 316 L. According to statistics R^2 value is 0.47.

The mean speed of cold spatters is increasing with MP1 as the laser power is increasing (which can be seen in figure 52). It can be concluded that the laser power correlates to the mean speed of detected cold spatters when using MP1 with R^2 value 0.74. The mean speed

for the cold spatters of MP1 increases as the laser power increases, because vapor vortex causing entrainment driven spatters increase. It cannot be concluded that increasing the laser power correlates to the mean speed of cold spatters when using 316 L. According to statistics R^2 value is 0.69.
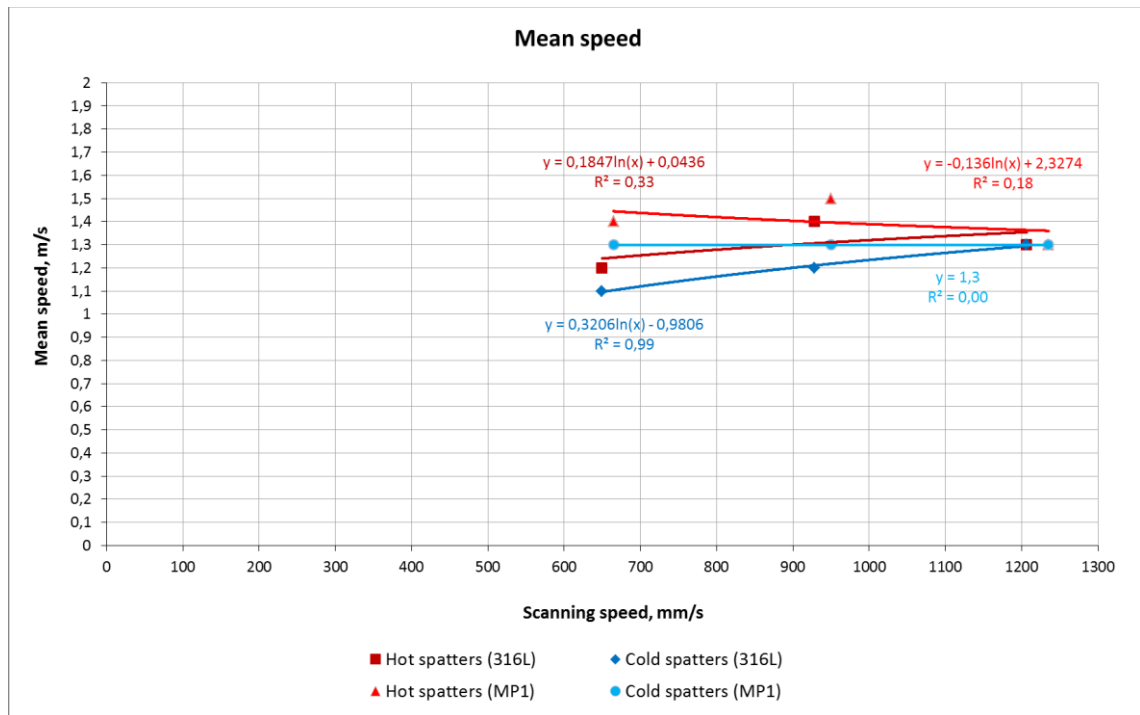
Figure 53. Mean speed of 316 L and MP1 hot and cold spatters when using different scanning speed.

It cannot be concluded that the scanning speed correlates to the mean speed of hot spatters when using 316 L and MP1 (which can be seen in figure 53). According to statistics R^2 value is 0.33 for 316 L and 0.18 for MP1. This can be explained by different spatter types in the test cases. For example, the test case SS -30 % has high heat input, which causes faster type I spatters and the spatters flying straight towards the camera cannot be detected by our current measurement system. Test case SS +30 % has low heat input which causes slow type II and III spatters when comparing to the type I spatters.

The mean speed of cold spatters is increasing with 316 L as the scanning speed is increasing (which can be seen in figure 53). It can be concluded that the scanning speed correlates to the mean speed of detected cold spatters when using 316 L with R^2 value 0.99. This can be explained by the snow-plow effect. It cannot be concluded that the

scanning speed correlates to the mean speed of cold spatters (which can be seen in figure 53). According to statistics R^2 value is 0. In 316 L the melt pool front becomes unstable when scanning speed is increased, and therefore it produces more type III spatters than MP1.

Based on the results of test series I for 316L it can be concluded that increasing the laser power will decrease the number of hot spatters, increase the number of cold spatters and will not affect to the mean speed of hot- or cold spatters. The numbers of detected hot and cold spatters increase as the scanning speed increases, and velocity of the cold particles increase. On the basis of information it can be assumed that recoil pressure driven spatters (spatter type I), entrainment driven spatters and snow-plow effect spatters (spatter type III) are more common than Marangoni effect and recoil pressure driven spatters (spatter type II).

Based on the results of test series I for MP1 it can be concluded that increasing the laser power does not affect to the number of hot or cold spatters. The velocities of detected hot and cold spatters increase when the laser power increases. The number of detected hot and cold spatters increases as the scanning speed increases. On the basis of information, it can be assumed that recoil pressure driven spatters (spatter type I) and Marangoni effect spatters (spatter type II) are prevalent when the laser power increases. When the scanning speed increases, Marangoni effect and recoil pressure driven spatters (spatter type II) and snow-plow effect spatters (spatter type III) are prevalent.

11.2 Test series II

Test series II was performed with Jai machine vision camera using Varioptic optics. The camera was focused 5 mm above the powder bed. The illumination laser sheet was calibrated to the same level. The purpose of the test series II was to test the effects of different laser powers and scanning speeds to the spatter mean per image number, spatter mean speed number and melt pool dimensions. The test was carried out using EOS 316 L material and the used machine was EOS M 290. Test series II consist of 13 different test cases which can be found from table 5. Test position was on left center of the building platform when viewed from building chamber door.

11.2.1 Mean per image

The mean per image number corresponds to how many observations there are on average in each image. The heat input correlation to the mean per image was tested with both materials in test series I. Heat input was calculated using equation 1. The mean per image of hot and cold spatters was analyzed for 316 L and compared to the heat input, laser power and scanning speed. Results are presented in figure 54, 55 and 56.
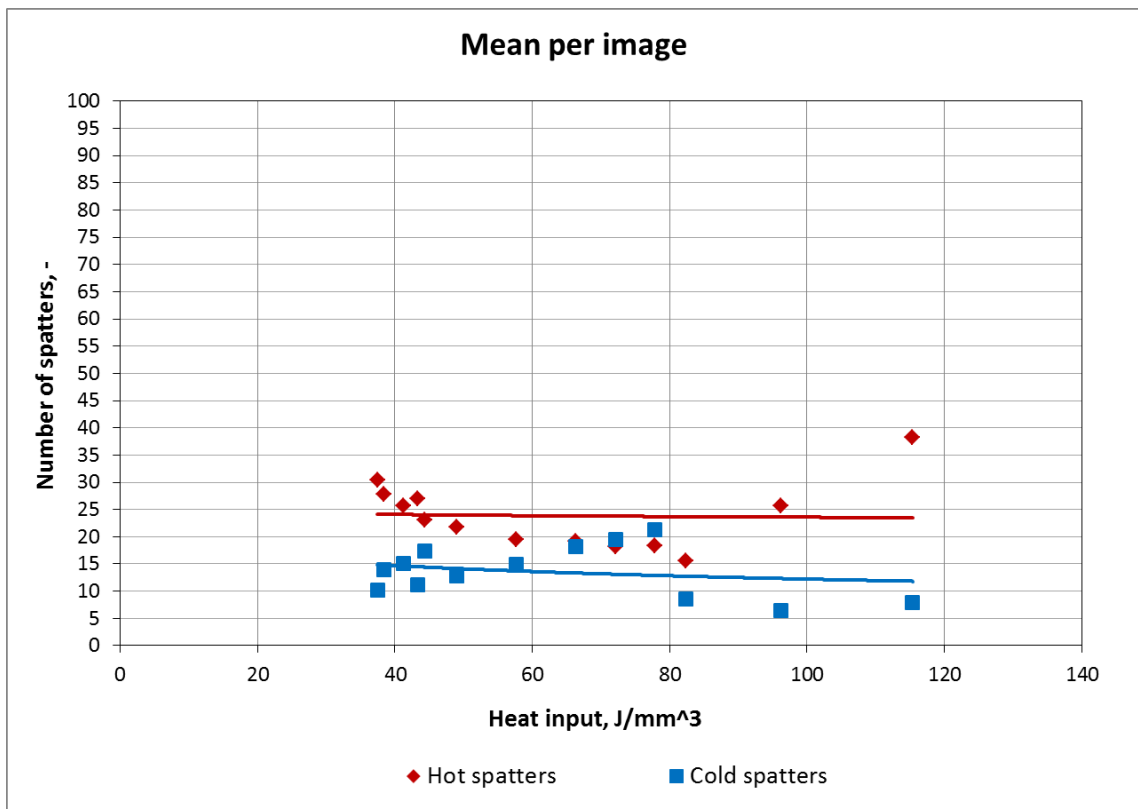

Figure 54. Mean per image value for 316 L when using different heat input.

It cannot be concluded that increasing the heat input correlates to the number of spatters when all test cases are analyzed (which can be seen in figure 54). When analyzing test cases SS +30, SS +40 and SS +50 increasing the heat input correlate to the number of hot spatters. Number of detected hot spatters increase as the heat input increases in test cases SS +30, SS +40 and SS +50, because when using high heat input, the melt pool becomes larger, which increases recoil pressure and Marangoni driven spattering (spatter type II). The process is moving from keyhole mode to the deep keyhole mode. Number of detected hot spatters decrease as the heat input increases in other test cases, because when the heat input is increasing the melt pool becomes more stable, which decreases recoil pressure and

Marangoni driven spattering (spatter type II). Process is moving from conduction mode to the keyhole mode.
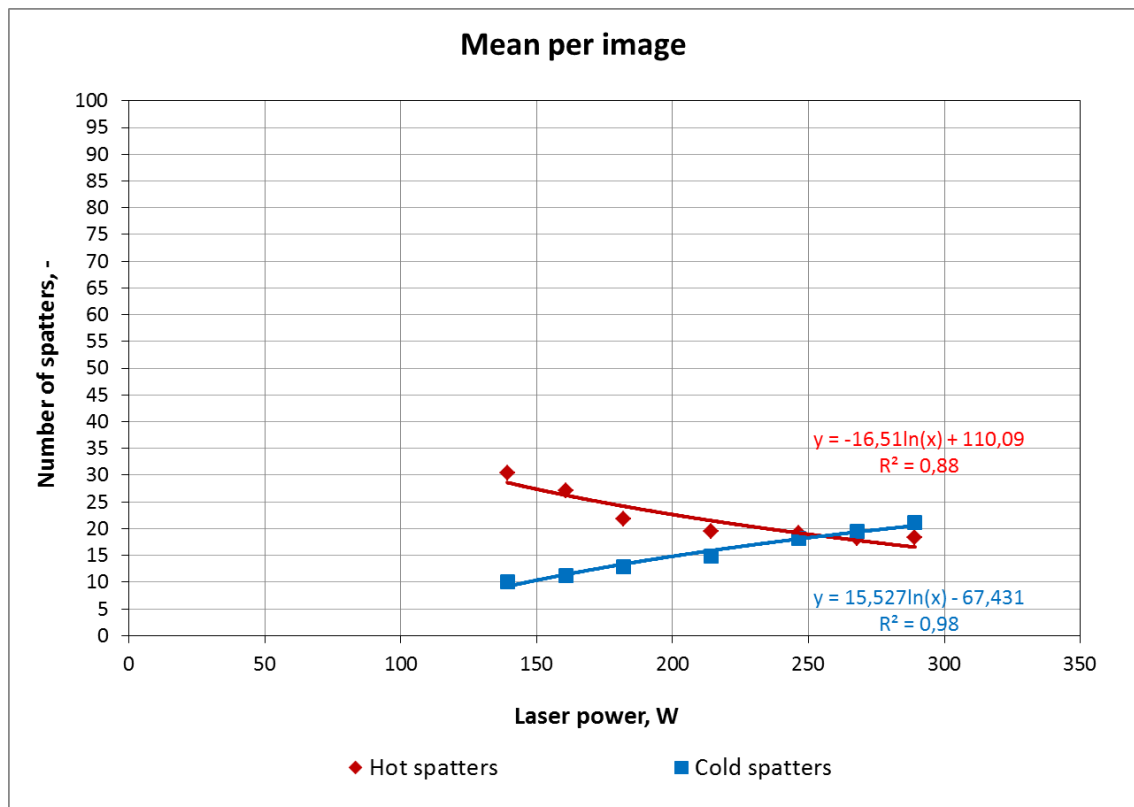
Figure 55. Mean per image value for 316 L when using different laser power.

The mean per image number of hot spatters decreases as the laser power increases (which can be seen in figure 55). It can be concluded that the laser power correlates to the number of detected hot spatters when using 316L with R^2 value 0.88. The number of detected hot spatters decreases as the laser power rises, because the forces causing recoil pressure driven spatters increases. Recoil pressure driven spatters fly upwards and our current measurement system cannot detect the spatters flying straight towards the camera.

The number of cold spatters increases as the laser power increases (which can be seen in figure 55). It can be concluded that the laser power correlates to the number of detected cold spatters when using 316L, because R^2 value is 0.98. Mean per image number for 316 L cold spatters increases as the laser power increases, because the vapor vortex causing entrainment driven spatters increase.

Figure 56. Mean per image value for 316 L when using different scanning speed.

It cannot be concluded that increasing the scanning speed correlates to the number of hot spatters when all test cases are analyzed (which can be seen in figure 56). According to statistics R^2 value is 0.08. When analyzing test cases STD, SS +30, SS +40 and SS +50 increasing the scanning speed correlate to the number of hot spatters. According to statistics R^2 value is 0.95. Number of detected hot spatters increase as the scanning speed increases in test cases STD, SS +30, SS +40 and SS +50, because when using high scanning speed the melt pool becomes longer and narrower, which increases recoil pressure and Marangoni driven spattering (spatter type II). Process is moving from keyhole mode to the conduction mode. Number of detected hot spatters decrease as the scanning speed increases in test cases SS -50, SS -40 and SS -30, because when the scanning speed is increasing the melt pool becomes more stable, which decreases recoil pressure and Marangoni driven spattering (spatter type II). Process is moving from deep keyhole to the keyhole mode.

The mean per image number of cold spatters increases as the scanning speed increases (which can be seen in figure 56). It can be concluded that scanning speed correlates to the

number of detected cold spatters, with R^2 value 0.80. Mean per image number of cold spatters increase when the scanning speed increases, because the vapor vortex causing entrainment driven spatters increase.

11.2.2   Mean speed

Mean speed value corresponds to how fast hot- and cold particles fly in the process. The correlation of heat input, laser power and scanning speed to the spatter mean speed was tested with material 316 L in test series II. Heat input was calculated by using equation 1. Mean speed of hot and cold spatters was analyzed for 316 L and compared to the heat input, laser power and scanning speed. Results are presented in figure 57, 58 and 59.
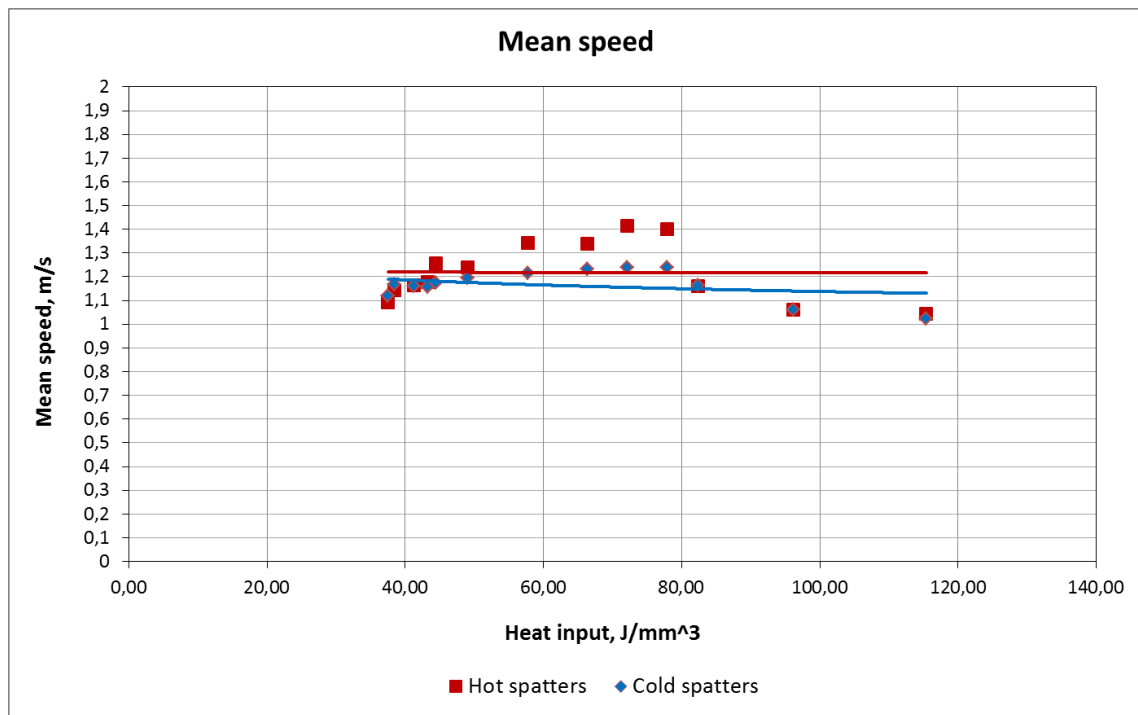
Figure 57. Mean speed of 316 L hot and cold spatters when using different heat input.

It cannot be concluded that increasing the heat input does not correlate to the mean speed of spatters when all test cases are analyzed (which can be seen in figure 57). When analyzing test cases except SS -30 %, SS -40 % and SS -50 % mean speed of spatters, number of spatters and the number of detected spatters increase as the heat input increases because the process is moving from conduction mode to the keyhole mode and therefore produces more recoil pressure driven type II spatters. In test cases SS -30, SS -40 and SS -

50 process is moving from keyhole mode to deep keyhole mode and therefore recoil pressure driven spatters (spatter type I) becomes prevalent.

Mean speed

The chart shows mean speed (m/s) vs. laser power (W) with two trend lines:

Hot spatters: $y = 0{,}4329\ln(x) - 1{,}0233$, $R^2 = 0{,}96$

Cold spatters: $y = 0{,}1626\ln(x) + 0{,}3327$, $R^2 = 0{,}93$
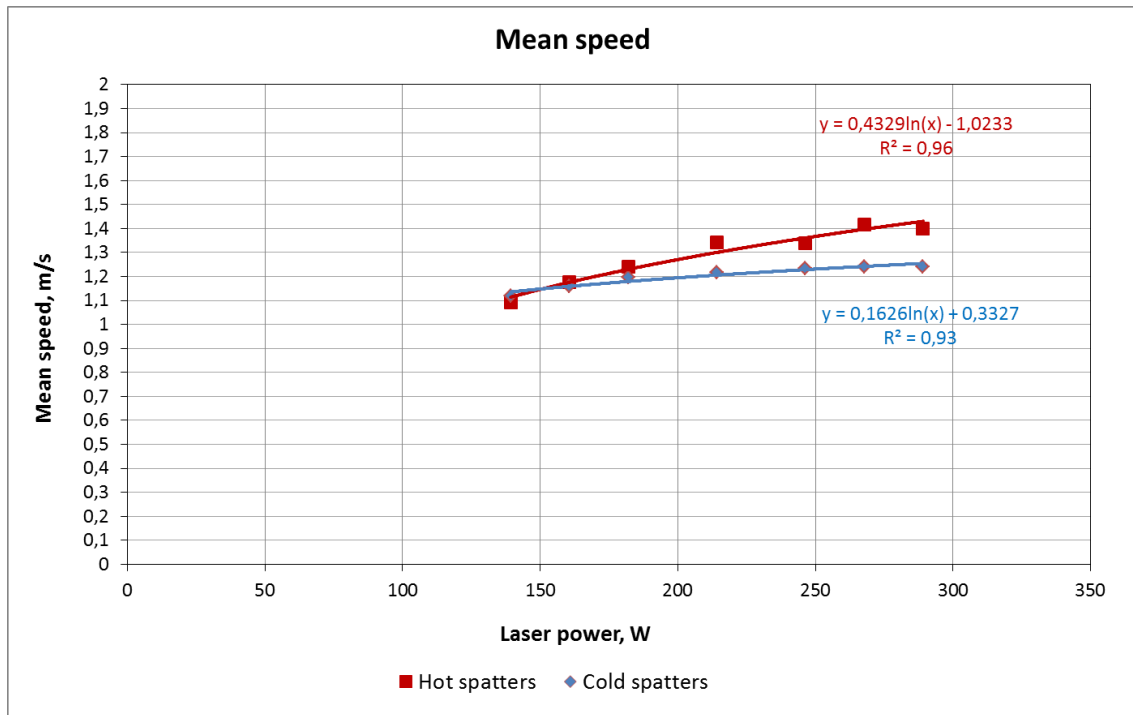
Figure 58. Mean speed of 316 L hot and cold spatters when using different laser power.

The mean speed of hot spatters increases as the laser power increases (which can be seen in figure 58). It can be concluded that laser power correlates to the hot spatters mean speed when using 316 L with R^2 value 0.96. Mean speed for hot spatters increase as the laser power increases, because forces causing Marangoni effect and recoil pressure (spatter type II) increase.

The mean speed of cold spatters is increasing as the laser power is increasing (which can be seen in figure 58). It can be concluded that the laser power correlates to the mean speed of detected cold spatters when using 316 L with R^2 value 0.93. The mean speed of the cold spatters increases as the laser power increases, because vapor vortex causing entrainment driven spatters increase.
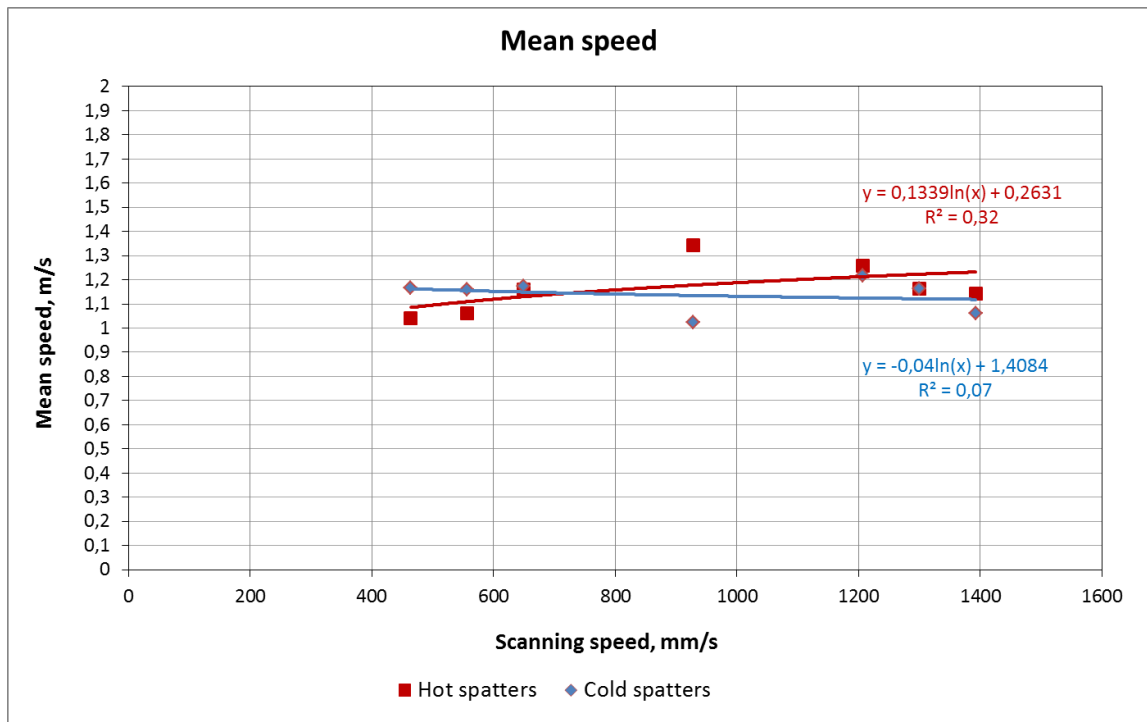
Figure 59. Mean speed of 316 L hot and cold spatters when using different scanning speed.

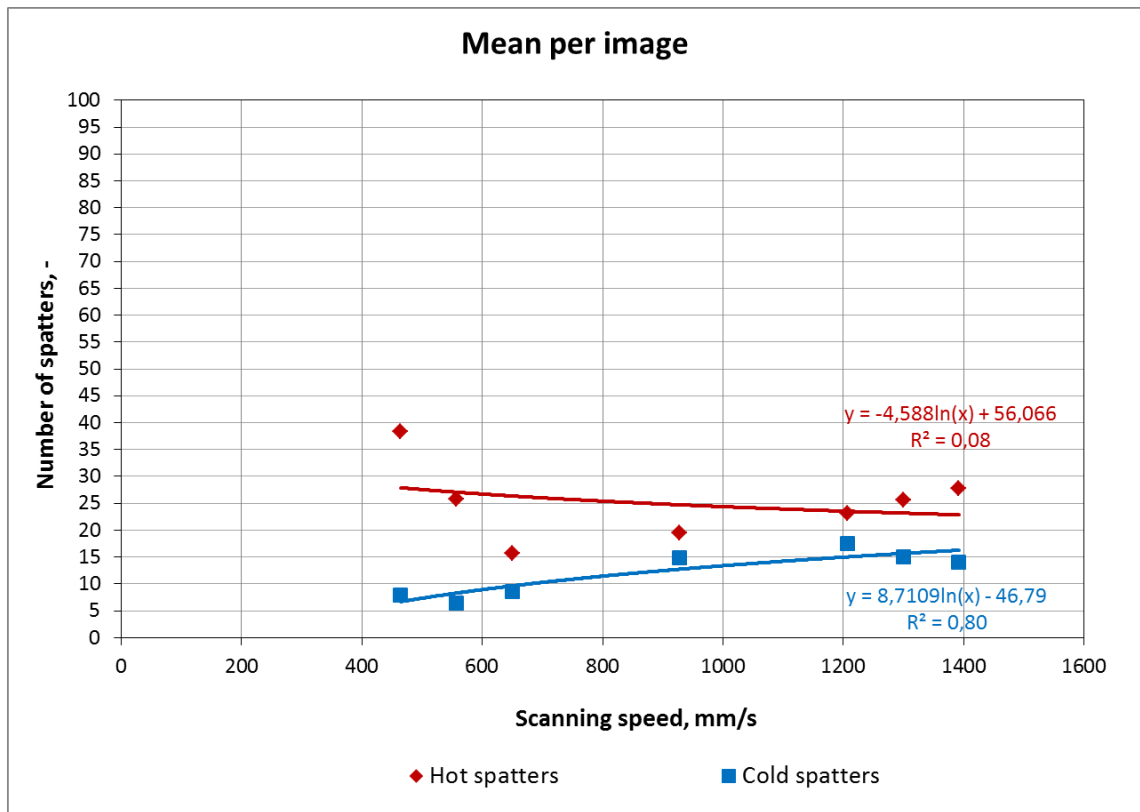It cannot be concluded that the scanning speed correlates to the mean speed of hot spatters (which can be seen in figure 59). According to statistics R^2 value is 0.32. This can be explained by different spatter types in the test cases. For example, in the test cases SS -50 %, SS -40 %, SS -30 % and STD, as the scanning speed increases the heat input decreases which reduces Marangoni effect. The number of Marangoni effect and the recoil pressure driven large spatters (spatter type II) decrease. The number of recoil pressure driven spatters (spatter type I) increases which causes increasing of the mean speed. In the test cases SS +30 %, SS +40 % and SS +50% heat input decreases as the scanning speed increases. Melt pool becomes longer and narrower which causes Marangoni effect and recoil pressure driven spattering (spatter type II). When using high scanning speeds, the melt pool becomes unstable and therefore, snow-plow effect spattering (spatter type III) increases. These larger and slower spatters (spatter types II and III) causes decreasing of the mean speed.

It cannot be concluded that the scanning speed correlates to the mean speed of detected cold spatters when all test cases are analyzed with R^2 value 0.07 (which can be seen in figure 59). When analyzing test cases SS +30 %, SS +40 % and SS +50 % mean speed of

cold spatters decrease as scanning speed increases because high scanning speeds causes slow snow-plow effect driven spatters (spatter type III).

11.2.3   Melt pool dimensions

Melt pool dimensions corresponds to how long and wide the melt pool is in the process. The correlation of heat input, laser power and scanning speed to the melt pool dimensions was tested 316 L in series II. Heat input was calculated by using equation 1. Melt pool length and width was analyzed for 316 L and compared to the heat input, laser power and scanning speed. Results are presented in figure 60, 61 and 62.
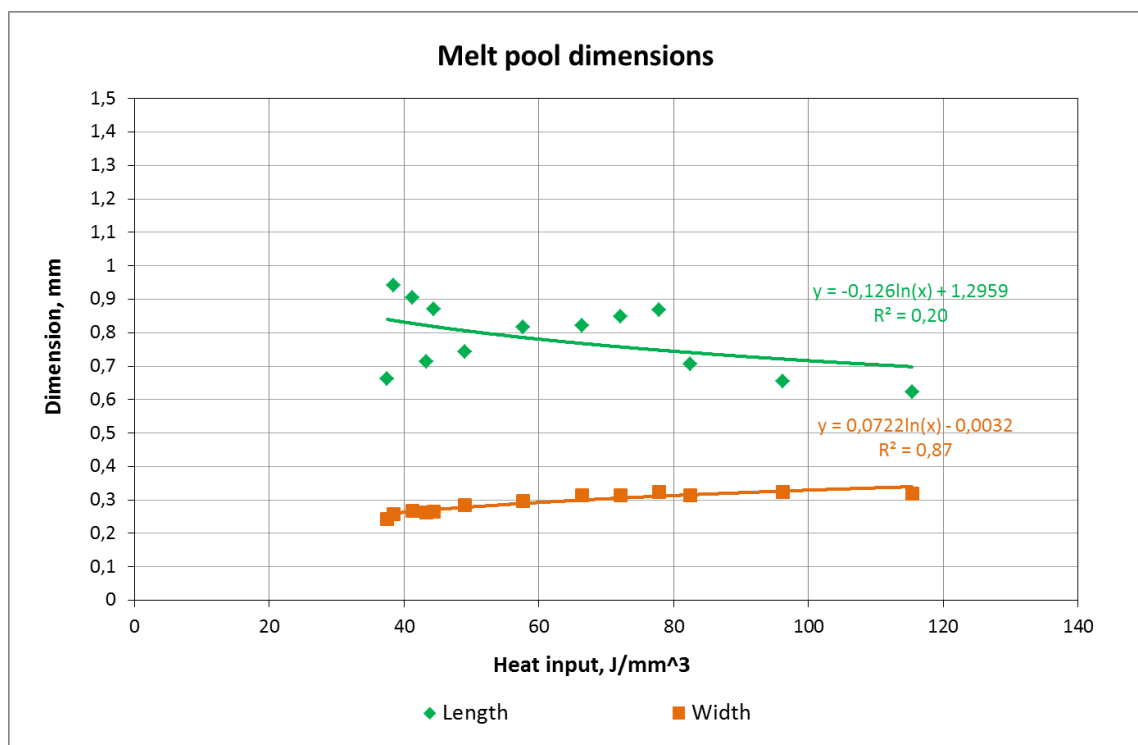
Figure 60. Melt pool dimensions of 316 L when using different heat input.

It can be concluded that the width of the melt pool correlates to the heat input with R^2 value 0.87 (which can be seen in figure 60). It cannot be concluded that the heat input correlates to melt pool length with R^2 value 0.20. The width of the melt pool remains almost constant when the heat input increases. This can be explained by the surrounding un-melted powder working as an insulation. The length of the melt pool has large variation when increasing the heat input, because heat transfers to the melted track rather than the un-melted powder.
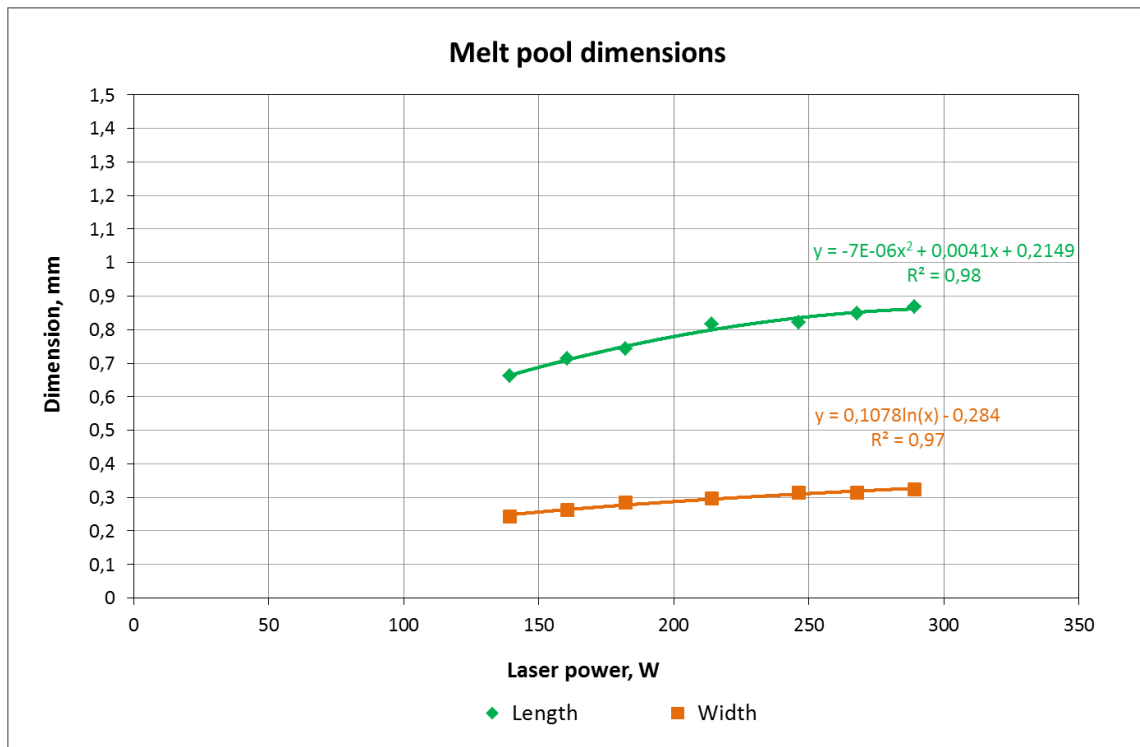
Figure 61. Melt pool dimensions of 316 L when using different laser power.

The length and width of the melt pool increases as the laser power increases (which can be seen in figure 61). It can be concluded that the laser power correlates to melt pool length with R^2 value 0.99, and width with R^2 value 1.00. Increasing the laser power influences more to the melt pool length than width because the surrounding un-melted powder works as an insulator and heat transfers to the melted track rather than the un-melted powder.
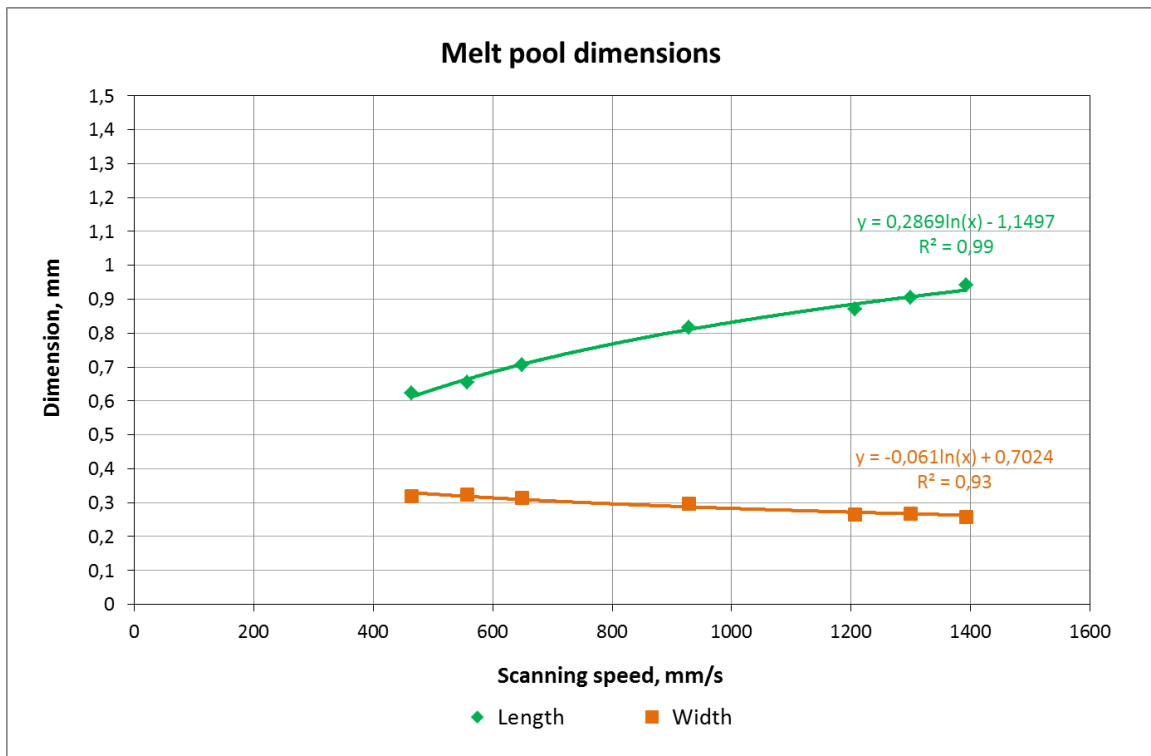
Figure 62. Melt pool dimensions of 316 L when using different scanning speed.

The length of the melt pool increases as the scanning speed increases (which can be seen in figure 62). It can be concluded that the scanning speed correlates to melt pool length with R^2 value 0.97. The width of the melt pool decreases as the scanning speed increases (which can be seen in figure 62). It can be concluded that the scanning speed correlates to melt pool width with R^2 value 0.99. Increasing the scanning speed increases the melt pool length and decreases the melt pool width, because heat input decreases as the scanning speed increases. When the scanning speed increases the melt pool does not have enough energy to expand in the widthwise direction. Therefore, melt pool width decreases.

Based on the results of test series II for 316L it can be concluded that increasing the laser power will decrease the number of hot spatters, increase the number of cold spatters, affects to the mean speed of hot or cold spatters and increase the melt pool length and width. Increasing the scanning speed does not correlate to the mean per image number of hot spatters. Increasing the scanning speed affects to the mean per image number of the detected cold spatters. Increasing the scanning speed does not affect to the mean speed of hot and cold spatters. As the scanning speed increases, the melt pool length increases and width decreases. On the basis of information, it can be assumed that recoil pressure driven

spatters (spatter type I), entrainment driven spatters and snow-plow effect spatters (spatter type III) are more common than Marangoni effect and recoil pressure driven spatters (spatter type II).

11.3 Discussions

Based on test series I and II, it was concluded that there are two prevalent mechanisms causing the spattering, depending on the phase of the process. Entrainment driven spattering is prevalent in the beginning of the standard process (conduction mode) before the laser beam has created a keyhole. The recoil pressure driven spattering becomes prevalent when the keyhole is formed (keyhole mode). Usually during the same laser stripe both of these mechanisms affect to the spattering depending on the melt pool depth and stability. The entrainment driven spatters are small (10-20 μm) and fast (10-20 m/s) and in the recoil pressure the spatters are large (50-70 μm) and slow (1-3 m/s). The mid-zone is in between of these mechanisms. In the mid-zone the spatter size is between 15-35 μm and velocity between 1-10 m/s. Different spattering mechanisms are shown in figure 63.
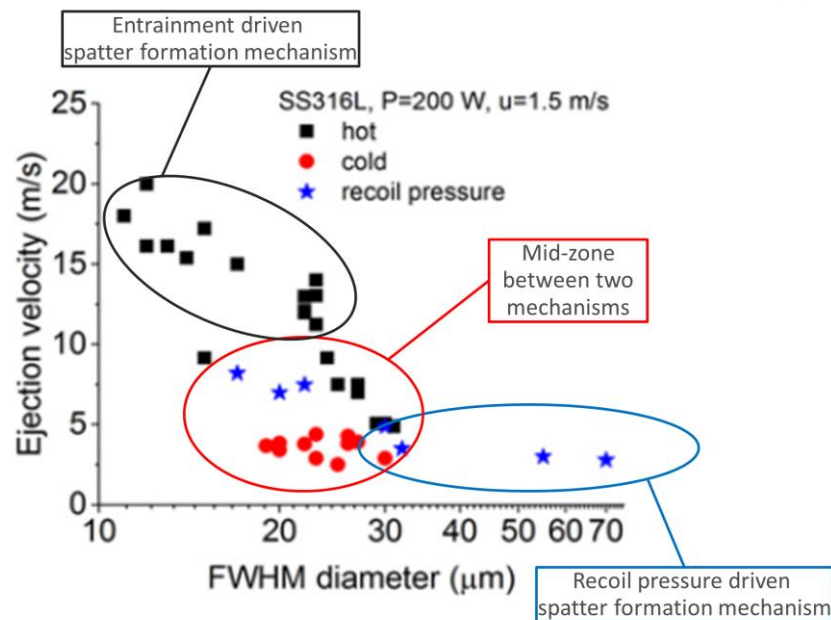
Figure 63. Different spattering mechanisms compared by ejection velocity and spatter size.

Higher productivity in AM is always desirable and therefore, faster scanning speed. Fast scanning speed causes instability to the melt pool, which causes elongation. Elongation can break from the melt pool creating balling defect. As the scanning speed increases the melt pool becomes shallower, length increases and width decreases, which increases Plateau-Rayleigh instability. As the melt pool becomes unstable it produces more hot and cold spatters (spatter type II) than the stable melt pool. It is therefore important to study the behavior of the melt pool in addition to the spatters. As the laser power is decreasing, the length and width of the melt pool is decreasing causing shallower melt pool, which increases the melt pool instability. However, high laser power causes strong Marangoni flow in the melt pool, which increases the number of spatters (spatter type II). High laser power increases vapor vortex around the melt pool, which causes the laser beam to scatter if the gas flow does not disintegrate the formed plasma cloud. High laser power causes deep keyhole, which increases the surface roughness of the build part.

12 CONCLUSIONS

Experimental set-up for spatter monitoring analysis system using machine vision camera and illumination laser was carried out in this thesis. This set-up and the measurement method provide the possibility to investigate the spatter phenomenon and melt pool behavior for better understanding of the process.

This thesis focused on the spatter analysis system hardware design, manufacturing and development. Linear rail with zero mounting system was selected for the spatter analysis system, because it minimizes user-specific variation, ensures the best repeatability between the tests and makes it possible to image left side of the building platform. JAI-GO-5100-USB was chosen as a camera, because it has the smallest physical size, high resolution sensor and stock-ready protection enclosure. Caspian C-39N0-250 liquid lens was chosen as optics because it was the only commercially available liquid lens for 2/3″ sensor size with variable iris. Oseir HiWatch was chosen as an illumination laser, because it was compatible with Osirec analysis software and it can illuminate also cold spatters.

The installation of the hardware of the measurement system was carried out inside the building chamber, on the left side of the chamber. Both sides of the building chamber could be investigated, but because it is hard to create even gas flow over the whole building platform, the left side was chosen to be investigated in this thesis. The left side of the building platform is located further from the illumination laser than the right side which makes it also a better location to test the illumination laser performance in the spatter illumination.

Testing of the measuring system was carried out by EOS. Measurement systems were tested in different temperatures (19 to 50 °C) and in different atmospheres (argon and nitrogen) within the building chamber of EOS M 290. The measurement system was found to work under different conditions and locations inside of the EOS M 290. The measurement procedure was also tested with different number of images and different number of layers to be imaged. Based on the results, an optimal number of 200 images from ten different layers per test case were selected as a measurement procedure, whereby

the effect of laser stripe angle can be minimized. The answers for the research questions set at the beginning of the thesis are as follows:

1. How spatters are defined?

In this thesis the spatters are defined as recoil pressure driven spatters (spatter type I, II and III) and entrainment driven spatters (type 1, type 2 and type 3). Recoil pressure and entrainment driven spattering produce hot and cold spatters. Hot spatters are recognized from their emitted light and cold spatter from the three-point series created by the illumination laser.

2. How do spatters form?

The spatters are ejected from melt pool and vapor vortex created by the process laser and powder bed interaction. Type I spatters are formed deep inside of the melt pool. Recoil pressure forms metallic jet upwards along the laser beam which ejects hot spatters. Type II hot droplet spatters are formed in the melt pool and are ejected in reverse scanning direction by Marangoni effect and recoil pressure. Type III powder spatters are formed in front of the melt pool which ejects hot spatters. Entrainment driven spatters are formed when the process laser beam creates rapidly moving vapor vortex around it. Type 1 subsumed spatters are absorbed into the melt pool. Type 2 cold spatters rise up from powder bed because of the vapor vortex, but do not hit to the laser beam. Type 3 hot spatters are type 2 cold spatters which hit to the laser beam.

3. How it is possible to image spatters with machine vision camera?

The machine vision camera used in this spatter analysis system images in monochrome. The camera detects the wavelength that hot spatters produces, and therefore is able to image the hot spatters. Cold spatters are illuminated with the illumination laser making them visible for the camera. The process is imaged from above, which enables detecting the spatters in xy-plane.

4. How spatters can be measured with this imaging system?

The spatters are measured with the spatter analysis system that was designed specifically for this thesis. The system measures the size of the spatter by first calculating the true pixel size (dividing field of view by resolution) and then by calculating how many pixels the

spatter illuminates. The speed of spatters can be measured by calculating how many pixels the spatter has moved during the exposure time of the camera.

5. How the measurement system was built to be suitable for monitoring spatters and melt pool with EOS requirements?

The hardware was tested in test series I, and the information gathered from test series I was used as a base for the changes in the hardware for test series II. The measurement system was designed to work in the best possible way in the EOS M 290 and only the best available components were used. DFMA and final users were taken into account in the designing process. A zero-point mounting system was designed to minimize the variation caused by users. The measurement system was designed to be as simple as possible to move to different locations in the machine, and to be easily removed from the machine without using any tools. The focus does not change even if the measurement system is removed from the machine and placed back inside.

6. What limitations spatter analysis systems have?

The spatters that are flying straight towards the camera cannot be detected with this measurement system set-up because the camera is placed above the building platform. The true pixel size (field of view divided by resolution) limits the size analysis of the melt pool and spatters. The length and power of the illumination laser pulse limits the speed analysis of spatters. Because of the zero-point mounting system it is possible to image only in the left side of the building platform at the moment.

7. How measured data can be used in research and development department?

Measured data can be used to determine in which mode (conduction or keyhole) the process is currently at. This information helps the R&D department in material parameter development and fine-tuning the current processes. The data received from the melt pool dimensions assists parameter development by finding faster the optimal laser power - scanning speed combination. The measured data can be used as a link between the process and hardware development departments.

13 FURTHER STUDIES

Spatter analysis system for DMLS process was designed and implemented in this thesis. The next logical step in further development of this system would be to inspect the multi fiber illumination laser with diffusors. The idea is to illuminate the whole platform because changing the place of the illumination laser and leveling it takes lot of time and increase user based variation. Creating enough pulse energy with one fiber using engineered diffusor produces technical problems. If the whole platform is to be illuminated, the illumination curtain needs to be created from four different spots. Further research should be focused on using different wavelengths on illumination, for example currently used 802 nm wavelength over exposes melt pool monitoring data and that is why it is important to find another suitable wavelength for illumination. Illumination laser with wavelength 405 nm could be more suitable for this kind of measurement system because the cameras have better quantum efficiency on visible (VIS) wavelengths than near-infrared (NIR) wavelengths. There are no commercially available 405 nm laser that is suitable for this system and therefore, it was not used in this thesis. The laser should have been specially designed and manufactured which would not have been possible at this time. With higher quantum efficiency images have less background noise.

Another important topic for further development area is the camera and liquid lenses. Camera should have a larger image sensor and because of that more pixels in the same field of view. When the number of pixels in the used field of view is increasing, the true pixel size is decreasing. The smaller true pixel size makes it possible to measure melt pool size and spatter size more precisely. At the moment there are no commercially available liquid lenses for larger image sensor than $1''$. That is a technical limitation for the use of high resolution cameras.

This thesis focused on imaging the left side of the building platform. The next step would be to image the rest of the building platform, because it was noticed that the location has influence to the quality of the part. Therefore, new and more functional mounting system should be designed. It was also noticed that different locations have different laminar shield gas flow depending on the location on the platform. For this reason, the Schlieren

imaging could be used for finding out the veritable gas flow on different locations. The Schlieren imaging is based on the density of transparent substance temperature differences or a different chemical composition. That causes changes in the substance refractive index. The Schlieren image shows the gas flow streams and turbulence. It was observed that the shield gas pressure and flow rate has effect on denudation zones and therefore, the influence of gas flow in the chamber to the spattering should be studied. Building chamber gas pressure has the more influence on denudation phenomenon compared to the laser power which can be seen as the surface roughness of the build part and it can be measured with confocal microscopy.

This thesis studied only two steel based materials, chromium-nickel stainless steel 316L and cobalt chrome MP1. Therefore, all materials and processes developed by Electro Optical Systems should be investigated. According to the comparison of the results for 316L and MP1 the spattering phenomena was material specific.

The depth of melt pool should be measured from metallographic sample to find out if the process is in the conduction mode, transition mode or keyhole mode. It is important to find the correlations between the processing mode and the number of spatters. In the current hardware measurement set-up an error on the focus plane is induced due to the position of the camera, it is in a small angle in relation to the building platform. That causes an error on the focus plane. It is possible to decrease the focus plane error with a Sheimpflug adapter by decreasing the angle between the focus plane and the building platform. Sheimpflug adapter makes it possible to tilt lens, which decreases the focus plane error. In the future it would be also suitable to test other commercially available image-based particle velocimetry software and compare the software features to the software used in this thesis.

LIST OF REFERENCES

3Dprint. 2018. Internet source. [Available: https://3dprint.com/178624/eos-eostate-exposure-ot/] [Accessed 4.1.2018]

3Dprinting industry. 2018. Internet source. [Available: https://3dprintingindustry.com/news/ge-publishes-patents-powder-bed-fusion-acoustic-monitoring-processes-qualify-metal-3d-printed-parts-114989/] [Accessed 4.1.2018]

Atzeni, E. & Salmi, A. 2015. Study on unsupported overhangs of AlSi10Mg parts processed by Direct Metal Laser Sintering (DMLS). Journal of Manufacturing Processes. Vol. 20, pp 500-506.

AutoVimation. Colibri. 2018. Internet source. [Available: http://www.autovimation.com/en/colibri-en][Accessed 4.1.2018]

Batchelor, B. 2012. Machine Vision Handbook Volume 2. London: Springer. 2291 p.

Beyerer, J., Puente León, F. & Frese, C. 2016. Machine Vision: Automated Visual Inspection: Theory, Practice and Applications. Berlin: Springer. 802 p.

Bi, G., Sun, C.N. & Gasser, A. 2013. Study on influential factors for process monitoring and control in laser aided additive manufacturing. Journal of Materials Processing Technology. Vol 213(3), pp. 463–468.

Bidare, P., Bitharas, I., Ward, R.M., Attallah, M.M. & Moore, A.J. 2018. Fluid and particle dynamics in laser powder bed fusion. Acta Materialia. Vol. 142, pp 107-120.

Bockoptronics. Schneider Xenoplan 1.9/35-0901. 2018. Internet source. [Available: http://www.bockoptronics.ca/bockoptronics/pdf/schneider/xenoplan_1_9_35.pdf][Accessed 4.1. 2018]

BrilliantOptics. Caspian C-39N0-250. 2018. Internet source. [Available: http://www.brilliantoptics.com/?p=210][Accessed 4.1.2018]

emva. GLOBAL MACHINE VISION INTERFACE STANDARDS. 2018. Internet source. [Available: http://www.emva.org/wp-content/uploads/FSF-Vision-Standards-Brochure-A4-screen.pdf] [Accessed 4.1.2018]

EOS. About EOS. INFO. 2018a. Internet source. [Available: https://www.eos.info/about_eos/history] [Accessed 4.1.2018]

EOS. Systems & Solutions. Metal. Materials. 2018b. Internet source. [Available: https://www.eos.info/material-m][Accessed 4.1.2018]

EOS. Industries & Markets. Aerospace. Engines. 2018c. Internet source. [Available: https://www.eos.info/industries_markets/aerospace/engines] [Accessed 4.1.2018]

EOS. Press. Press Release. March, 17th 2018d. Internet source. [Available: https://www.eos.info/eos_new_metal_materials_eos_titanium_ti64eli-eos_stainlesssteel_316l][Accessed 4.1.2018]

EOS. EOS M290. 2018e. Internet source. [Available: https://www.eos.info/eos-m290][Accessed 4.1.2018]

Ferrar, B., Mullen, L., Jones, E., Stamp, R. & Sutcliffe, C.J. 2011. Gas flow effects on selective laser melting (SLM) manufacturing performance. Journal of Materials Processing Tech.

Gade, R., Moeslund, T. B. 2014. Thermal cameras and applications: a survey. Machine Vision and Applications. Vol. 25, pp. 245–262.

Gunenthiram, V., Peyre, P., Schneider, M., Dal, M., Coste, F., Koutiri, I. & Fabbro, R. 2018. Experimental analysis of spatter generation and melt-pool behavior during the

powder bed laser beam melting process. Journal of Materials Processing Tech. Vol. 251, pp. 376-386.

Gibson, I., Rosen, W. & Stucker, B. 2010. Additive Manufacturing Technologies: Rapid Prototyping to Direct Digital Manufacturing. New York: Springer Science + Business Media. 459 p.

Gu, D. 2015. Laser Additive Manufacturing of High-Performance Materials. New York: Springer Science + Business Media. 322 p.

Heeling, T. & Wegener, K. 2016. Computational Investigation of Synchronized Multibeam Strategies for the Selective Laser Melting Process. Physics Procedia. Vol 83, pp. 899-908.

jai. Products. Spark series. 2018. Internet source. [Available: http://www.jai.com/en/products/spark-series-cmos-inspection-cameras-area-scan] [Accessed 4.1.2018]

Khairallah, S.A., Anderson, A.T., Rubenchik, A. & King, W.E. 2016. Laser powder-bed fusion additive manufacturing: Physics of complex melt flow and formation mechanisms of pores, spatter, and denudation zones. Acta Materialia. Vol 108, pp. 36-45.

Koseski, R.P., Suri, P., Earhardt, N.B., German, R.M. & Kwon, Y-S. 2005. Microstructural evolution of injection molded gas- and water-atomized 316L stainless steel powder during sintering. Materials Science & Engineering A. Vol. 390(1), pp. 171-177.

Ladewig, A., Schlick, G., Fisser, M., Schulze, V. & Glatzel, U. 2016. Influence of the shielding gas flow on the removal of process by-products in the selective laser melting process. Additive Manufacturing. Vol. 10, pp. 1-9.

LASERSTODAY. 2018a. Internet source. [Available: https://www.laserstoday.com/2016/07/laser-welding-fundamentals/] [Accessed 4.1.2018]

LASERSTODAY. 2018b. Internet source. [Available: https://www.laserstoday.com/2017/07/quality-assurance-of-selective-laser-melting-applications/] [Accessed 4.1.2018]

Lavery, N.P, Brown, S.G.R., Sienz, J., Cherry, J. & Belblidia, F. 2014. A Review of Computational Modelling of Additive Layer, Manufacturing - Multi-Scale and Multi-Physics. Sustainable Design and Manufacturing. Pp. 668-690.

Liu, Y., Yang, Y., Mai, S., Wang, D. & Song, C. 2015. Investigation into spatter behavior during selective laser melting of AISI 316L stainless steel powder. Materials & Design. Vol. 87, pp. 797-806.

Ly, S., Rubenchik, A.M., Khairallah, S.A., Guss, G. & Matthews, M.J. 2017. Metal vapor micro-jet controls material redistribution in laser powder bed fusion additive manufacturing. Scientific Reports. Vol. 7.

Matthews, M.J., Guss, G., Khairallah, S.A., Rubenchik, A.M., Depond, P.J. & King, W.E. 2016. Denudation of metal powder layers in laser powder bed fusion processes. Acta Materialia. Vol. 114, p. 33-42.

Opli. Machine vision. 2018. Internet source. [Available: http://www.opli.net/opli_magazine/imaging/2017/new-go-series-5-megapixel-usb3-vision-camera-runs-at-74-fps-may-news/][Accessed 4.1.2018].

Oseir. Industrial Imaging. 2018. Internet source. [Available: http://www.oseir.com/industrialimaging.html] [Accessed 4.1.2018].

Pavlov, M., Doubenskaia, M. & Smurov, I. 2010. Pyrometric analysis of thermal processes in SLM technology. Physics Procedia. Vol 5, pp. 523–531.

Pddnet. Innovations in Metal 3D Printing. 2018. Internet source. [Available: https://www.pddnet.com/article/2016/04/innovations-metal-3d-printing][Accessed 4.1.2018].

Pei, W., Zhengying, W., Zhen, C., Junfeng, L., Shuzhe, Z. & Jun, D. 2017. Numerical simulation and parametric analysis of selective laser melting process of AlSi10Mg powder. Applied Physics A. Vol. 123(8), pp. 1-15.

photographylife. PHOTOGRAPHY TUTORIALS. SENSOR SIZE, PERSPECTIVE AND DEPTH OF FIELD. 2018. Internet source. [Available: https://photographylife.com/sensor-size-perspective-and-depth-of-field] [Accessed 4.1.2018]

Ptgrey. Grasshopper3. 2018. Internet source. [Available: https://eu.ptgrey.com/grasshopper3-23-mp-mono-usb3-vision-sony-pregius-imx174][Accessed 4.1.2018].

Ophir. 2018. Internet source. [Available: http://www.ophiropt.com/de/laser-measurement-instruments/beam-profilers/products/camera-based-profilers/beamgage][Accessed 4.1.2018]

Purtonen, T., Kalliosaari, A. & Salminen, A. 2014. Monitoring and adaptive control of laser processes. Physics Procedia. Vol. 56 pp. 1218–1231.

Qiu, C., Panwisawas, C., Ward, M., Basoalto, H.C., Brooks, J.W. & Attallah, M.Z. 2015. On the role of melt flow into the surface structure and porosity development during selective laser melting. Acta Materialia. Vol. 96, pp. 72-79.

Repossini, G., Laguzza, V., Grasso, M. & Colosimo, B.M. 2017. On the use of spatter signature for in-situ monitoring of Laser Powder Bed Fusion. Additive Manufacturing. Vol. 16, pp. 35-48.

ResearchGate. Brandaris 128: A digital 25 million frames per second camera with 128 highly sensitive frames. 2018. Internet source. [Available: https://www.researchgate.net/publication/228937545_Brandaris_128_A_digital_25_million_frames_per_second_camera_with_128_highly_sensitive_frames][Accessed 4.1.2018].

Simonelli, M., Tuck, C., Aboulkhair, N.T., Maskey, I., Ashcroft, I., Wildman, R.D. & Hague, R. 2015. A Study on the Laser Spatter and the Oxidation Reactions During Selective Laser Melting of 316L Stainless Steel, Al-Si10-Mg, and Ti-6Al-4V. Metallurgical and Materials Transactions A. Vol. 46(9), pp. 3842-3851.

Spears, T. & Gold, S. 2016. In-process sensing in selective laser melting (SLM) additive manufacturing. Integrating Materials and Manufacturing Innovations. Vol. 5(1), p. 1–25.

Taheri Andani, M., Dehghani, R., Karamooz-Ravari, M.R., Mirzaeifar, R. & Ni, J. 2017. Spatter formation in selective laser melting process using multi-laser technology. Materials & Design. Vol. 131, pp. 460-469.

TelescopeOptics. 2018. Internet source. [Available: http://www.telescope-optics.net/optical_coatings.htm] [Accessed: 4.1.2018]

Vision Doctor. Optical basics. 2018. Internet source. [Available: http://www.vision-doctor.com/en/optical-basics/image-circle-diameter.html] [Accessed 4.1.2018]

Wang, D., Wu, S., Fu, F., Mai, S., Yang, Y., Liu Y. & Song, C. 2017. Mechanisms and characteristics of spatter generation in SLM processing and its effect on the properties. Materials & Design. Vol. 117, pp. 121-130.

Lee, Y.S. & Zhang W. 2015 Mesoscopic Simulation of Heat Transfer and Fluid Flow in Laser Powder Bed Additive Manufacturing.
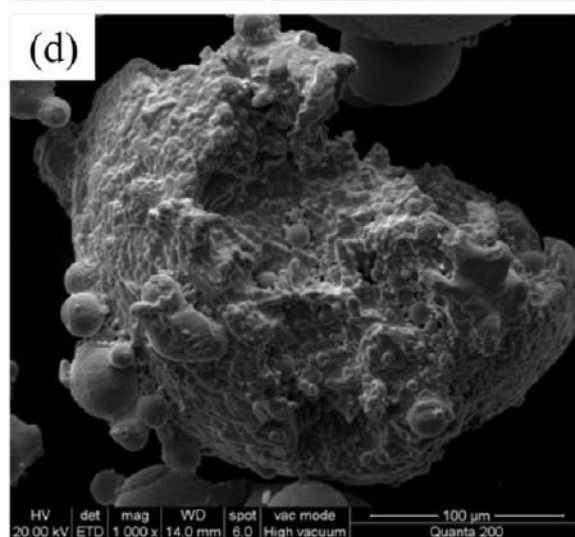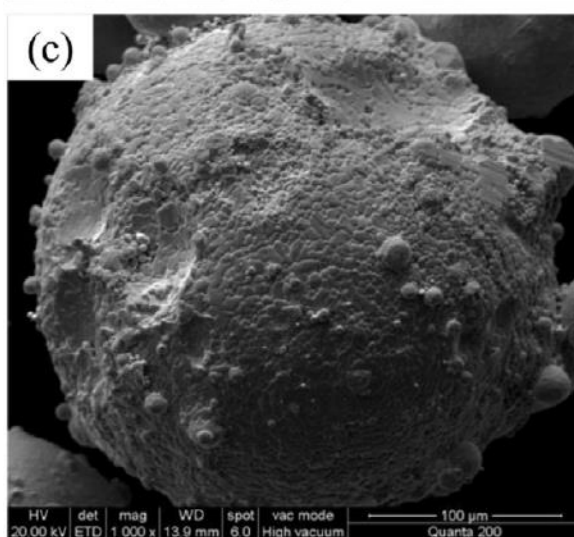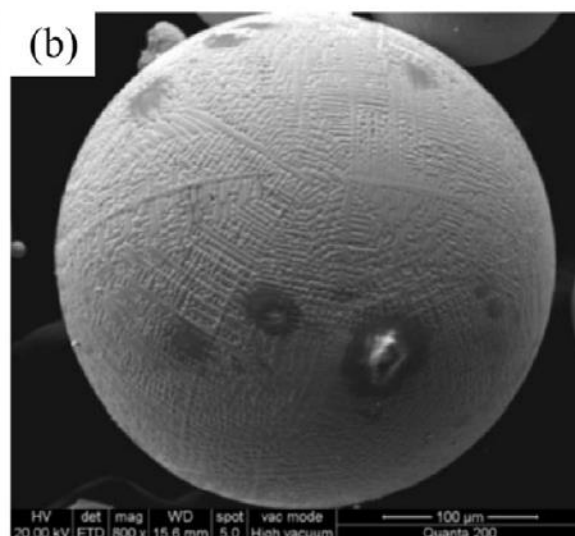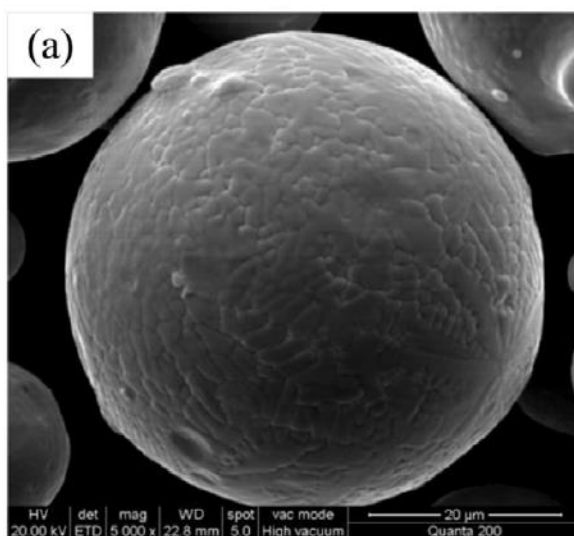
EOS StainlessSteel 316L

EOS StainlessSteel 316L is a corrosion resistant iron based alloy which has been optimized especially for processing on EOSINT M280 systems.

This document provides information and data for parts built using EOS StainlessSteel 316L powder (EOS art.-no. 9011-0032) on the following system specifications:

- EOSINT M280 200W System with PSW3.6 and Parameter Set 316L_Surface 1.0
- EOSINT M280 400W System with PSW3.6 and Parameter Set 316L_Surface 1.0
- EOS M290 400W System with EOSPRINT 1.0 and Parameter Set 316L_Surface 1.0

Description

The parts built from EOS StainlessSteel 316L have chemical composition corresponding to ASTM F138 "Standard Specification for Wrought 18Cr-14Ni-2.5Mo Stainless Steel Bar and Wire for Surgical Implants (UNS S31673)". This kind of stainless steel is characterized having a good corrosion resistance and evidence that there are no leachable substances in cytotoxic concentrations.

This material is ideal in

- Lifestyle/Consumer, e.g. watches, other jewellery, spectacle frames, decorations
- Automotive/Industrial, e.g. non-corroding common material, food and chemical plants
- Aerospace/Turbine industry
- Entry-level material for Laser Sintering Technology, e.g. mounting parts, heat exchangers, functional elements in electronic housing and accessories

Parts built from EOS StainlessSteel 316L can be machined, shot-peened and polished in as-built or stress relieved (AMS2759) states if required. Solution annealing is not necessary because the mechanical properties of as-built state are showing desired values (ASTM A403). Parts are not ideal in temperature range 427°C – 816°C where precipitation of chromium carbides occurs. Due to layer-wise building method, the parts have a certain anisotropy which could be seen from mechanical properties.

Technical data

General process data

	EOS StainlessSteel 316L
Typical achievable part accuracy [1], [7]	
– small parts	approx. ±20–50 µm (±0.0008 – 0.002 inch)
– large parts	approx. ± 0.2 %
Min. wall thickness [2], [7]	approx. 0.3 - 0.4 mm (0.012 – 0.016 inch)
Layer thickness	20 µm (0,8 x 10⁻ inch)
Surface roughness [3], [7]	
– as-manufactured	R. 13 ±5 µm; R. 80 ±20 µm R. 0.5 ±0.2 x 10⁻³ inch; R. 3.1 ±0.8 x 10⁻³ inch
– after shot-peening	R_a 5 ±2 µm; R_z 30 ±10µm R. 0.2 ±0.08 x 10⁻² inch; R. 1.2 ±0.4 x 10⁻² inch
– after polishing	R_z up to < 1 µm Rz up to < 0.04 x 10⁻² inch (can be very finely polished)
Volume rate [4]	2 mm³/s (7.2 cm³/h) 0.44 in³/h

[1] Based on users' experience of dimensional accuracy for typical geometries, e.g. ± 40 µm when parameters can be optimized for a certain class of parts or ± 60 µm when building a new kind of geometry for the first time. Part accuracy is subject to appropriate data preparation and postprocessing.

[2] Mechanical stability is dependent on geometry (wall height etc.) and application

[3] Due to the layerwise building, the surface structure depends strongly on the orientation of the surface, for example sloping and curved surfaces exhibit a stair-step effect. The values also depend on the measurement method used. The values quoted here given an indication of what can be expected for vertical surfaces.

[4] Volume rate is a measure of build speed during laser exposure. The total build speed depends on the average volume rate, the recoating time (related to the number of layers) and other factors such as contour and Up-/DownSkin parameters.

Physical and chemical properties of parts

	EOS StainlessSteel 316L		
Material composition	Element	Min	Max
	Fe	balance	
	Cr	17.00	19.00
	Ni	13.00	15.00
	Mo	2.25	3.00
	C		0.030
	Mn		2.00
	Cu		0.50
	P		0.025
	S		0.010
	Si		0.75
	N		0.10
Relative density with standard parameters	approx. 100 %		
Density with standard parameters	min. 7.9 g/cm³ min. 0.285 lb/in³		

Mechanical properties of parts (at room temperature) [7]

	As built
Ultimate tensile strength [5]	
– in horizontal direction (XY)	640 ± 50 MPa
– in vertical direction (Z)	540 ± 55 MPa
Yield strength, Rp0.2% [5]	
– in horizontal direction (XY)	530 ± 60 MPa
– in vertical direction (Z)	470 ± 90 MPa
Young's modulus [5]	
– in horizontal direction (XY)	typ. 185 GPa
– in vertical direction (Z)	typ. 180 GPa
Elongation at break [5]	
– in horizontal direction (XY)	40 ± 15 %
– in vertical direction (Z)	50 ± 20 %
Hardness [6]	typ. 89 HRB

[5] Machining and testing of the test bars according to ISO 6892 / ASTM E8M, proportional test pieces, diameter of the neck area 5 mm (0.2 inch), gauge length 4D – 20.0mm (0.79 inch), stress rate 10MPa/s, strain speed in plastic region 0.375 1/min.

[6] Rockwell hardness (HRB) measurement according to EN ISO 6508-1 on grinded surface.

[7] These properties were determined on an EOSINT M 280-400W. Test parts from following machine types EOSINT M 280-200W and EOS M 290-400W correspond with these data.

Abbreviations

typ.	typical
min.	minimum
approx.	approximately
wt	weight

The quoted values refer to the use of these materials with EOSINT M 280 systems according to current specifications (including the latest released process software PSW and any hardware specified for the relevant material) and operating instructions. All values are approximate. Unless otherwise stated, the quoted mechanical and physical properties refer to standard building parameters and test samples built in vertical orientation. They depend on the building parameters and strategies used, which can be varied by the user according to the application.

The data are based on our latest knowledge and are subject to changes without notice. They are provided as an indication and not as a guarantee of suitability for any specific application.

EOS®, EOSINT®, DMLS®, DirectTool® and DirectPart® are registered trademarks of EOS GmbH.

EOS CobaltChrome MP1

EOS CobaltChrome MP1 is a cobalt-chrome-molybdenum-based superalloy powder which has been optimized especially for processing on EOSINT M systems.

This document provides information and data for parts built using EOS CobaltChrome MP1 powder (EOS art.-no. 9011-0012) on the following system specifications:

- EOSINT M 270 Installation Mode *Standard*
  with PSW 3.3 or 3.4 and default job CC20_MP1_020_default.job or
  CC20_MP1_040_default.job

- EOSINT M 270 Dual-Mode
  with PSW 3.5 and EOS Original Parameter Set MP1_Surface 1.0 or
  MP1_Performance 1.0

- EOSINT M 280
  with PSW 3.5 and EOS Original Parameter Set MP1_Surface 1.0, MP1_Performance 1.0
  or MP1_Speed 1.0

Description

Parts built from EOS CobaltChrome MP1 conform to the chemical composition UNS R31538 of high carbon CoCrMo alloy. They are nickel-free (< 0.1 % nickel content) and are characterized by a fine, uniform crystal grain structure. As built EOS CobaltChrome MP1 meets the chemical and mechanical specifications of ISO 5832-4 and ASTM F75 for cast CoCrMo implant alloys, as well as the specifications of ISO 5832-12 and ASTM F1537 for wrought CoCrMo implants alloys except remaining elongation. The remaining elongation can be increased to fulfil even these standards by high temperature stress relieving or hot isostatic pressing (HIP).

Parts made from EOS CobaltChrome MP1 can be machined, spark-eroded, welded, micro shot-peened, polished and coated if required. They are suitable for biomedical applications (note: subject to fulfilment of statutory validation requirements where appropriate), and for parts requiring high mechanical properties in elevated temperatures (500 - 1000 °C) and with good corrosion resistance. Due to the layerwise building method, the parts have a certain anisotropy, which can be reduced or removed by appropriate heat treatment - see Technical Data for examples.

Technical data

General process data

Typical achievable part accuracy [1]	
– small parts	approx. $\pm$ 20 – 50 µm approx. $\pm$ 0.8 – 2 x 10^{-2} inch
– large parts	approx. $\pm$ 50 – 200 µm approx. $\pm$ 2 – 8 x 10^{-2} inch
Min. wall thickness [2]	approx. 0.3 mm approx. 0.012 inch
Surface roughness [3]	
– as built	
MP1 Surface (20 µm)	R_a 4 –10 µm; R_z 20 – 40 µm R_a 0.16 – 0.39 x 10^{-2} inch, R_z 0.79 – 1.57 x 10^{-2} inch
MP1 Performance (40 µm)	R_a 7 – 10 µm; R_z 35 – 50 µm R_a 0.28 – 0.39 x 10^{-2} inch, R_z 1.37 – 1.96 x 10^{-2} inch
MP1 Speed (50 µm)	R_a 8 – 12 µm; R_z 38 – 50 µm R_a 0.31 – 0.47 x 10^{-2} inch, R_z 1.49 – 1.96 x 10^{-2} inch
– after polishing	R_z up to < 1µm R_z up to < 0.04 x 10^{-2} inch
Volume rate [4]	
– Parameter set MP1_Surface 1.0 / default job CC20_MP1_020_default.job (20 µm layer thickness)	1.6 mm²/s (5.1 cm²/h) 0.35 in²/h
– Parameter set MP1_Performance 1.0 / default job CC20_MP1_040_default.job (40 µm layer thickness)	3.2 mm²/s (11.5 cm²/h) 0.70 in²/h
– Parameter set MP1_Performance 1.0 for M 280 / 400 W (40 µm layer thickness)	4.2 mm²/s (15.1 cm²/h) 0.92 in²/h
– Parameter set MP1_Speed 1.0 / for M 280 / 400 W (50 µm layer thickness)	5.5 mm²/s (19.8 cm²/h) 1.21 in²/h

[1]   Based on users' experience of dimensional accuracy for typical geometries, e.g. $\pm$ 20 μm (0.8 x 10 [-3] inch) when parameters can be optimized for a certain class of parts or $\pm$ 50 μm (2 x 10 [-3] inch) when building a new kind of geometry for the first time. For larger parts the accuracy can be improved by post-process stress-relieving at 1150 °C (2100 °F) for 6 hours. Part accuracy is subject to appropriate data preparation and post-processing, in accordance with EOS training.

[2]   Mechanical stability is dependent on geometry (wall height etc.) and application

[3]   Due to the layerwise building, the surface structure depends strongly on the orientation of the surface, for example sloping and curved surfaces exhibit a stair-step effect. The values also depend on the measurement method used. The values quoted here given an indication of what can be expected for horizontal (up-facing) or vertical surfaces.

[4]   Volume rate is a measure of build speed during laser exposure. The total build speed depends on the average volume rate, the recoating time (related to number of layers) and other factors such as DMLS-Start settings.

Physical and chemical properties of parts

Material composition	Co (60 – 65 wt-%)
	Cr (26 – 30 wt-%)
	Mo (5 – 7 wt-%)
	Si ($\leq$ 1.0 wt-%)
	Mn ($\leq$ 1.0 wt-%)
	Fe ($\leq$ 0.75 wt-%)
	C ($\leq$ 0.16 wt-%)
	Ni ($\leq$ 0.10 wt-%)
Relative density	approx. 100 %
Density	approx. 8.3 g/cm³
	approx. 0.30 lb/in³

Mechanical properties of parts at 20 °C (68 °F)

	As built	Stress relieved [5]
Tensile strength [6]		
– in horizontal direction (XY)	1350 ± 100 MPa 196 ± 15 ksi	1100 ± 100 MPa 160 ± 15 ksi
– in vertical direction (Z)	1200 ± 150 MPa 174 ± 22 ksi	1100 ± 100 MPa 160 ± 15 ksi
Yield strength (Rp 0.2 %) [6]		
– in horizontal direction (XY)	1060 ± 100 MPa 154 ± 15 ksi	600 ± 50 MPa 87 ± 7 ksi
– in vertical direction (Z)	800 ± 100 MPa 116 ± 15 ksi	600 ± 50 MPa 87 ± 7 ksi
Elongation at break [6]		
– in horizontal direction (XY)	(11 ± 3) %	min. 20 %
– in vertical direction (Z)	(24 ± 4) %	min. 20 %
Modulus of elasticity [6]		
– in horizontal direction (XY)	200 ± 20 GPa 29 ± 3 Msi	200 ± 20 GPa 29 ± 3 Msi
– in vertical direction (Z)	190 ± 20 GPa 28 ± 3 Msi	200 ± 20 GPa 29 ± 3 Msi
Fatigue life [7]		
– max. stress to reach 10 million cycles	approx. 560 MPa, 81 ksi	
– max. stress to reach 1 million cycles	approx. 660 MPa, 96 ksi	
Hardness [8]	approx. 35 – 45 HRC	

[5] High temperature stress relieved, 6 hours at 1150 °C (2100 °F) under inert argon atmosphere

[6] Tensile testing according to ISO 6892-1:2009 (B) Annex D, proportional test pieces, diameter of the neck area 5mm (0.2 inch), original gauge length 25mm (1 inch).

[7] Testing according to ASTM E466:1996, using vertical samples, as built, under 250 MPa (36.3 ksi) stress amplitude and 44 Hz testing frequency

[8] Rockwell C (HRC) hardness measurement according to EN ISO 6508-1 on polished surface. Note that measured hardness can vary significantly depending on how the specimen has been prepared.

Thermal properties of parts

	As built
Coefficient of thermal expansion	
– over 20 – 500 °C (68 – 932 °F)	typ. 13.6 x 10^{-6} m/m °C typ. 7.6 x 10^{-6} in/in °F
– over 500 – 1000 °C (932–1832 °F)	typ. 15.1 x 10^{-6} m/m °C typ. 8.4 x 10^{-6} in/in °F
Thermal conductivity	
– at 20 °C (68 °F)	typ. 13 W/m °C typ. 90 Btu in/(h ft² °F)
– at 300 °C (572 °F)	typ. 18 W/m °C typ. 125 Btu in/(h ft² °F)
– at 500 °C (932 °F)	typ. 22 W/m °C typ. 153 Btu in/(h ft² °F)
– at 1000 °C (1832 °F)	typ. 33 W/m °C typ. 229 Btu in/(h ft² °F)
Maximum operating temperature	approx. 1150 °C approx. 2100 °F
Melting range	1350 – 1430 °C 2460 – 2600 °F

Abbreviations

typ.	typical
min.	minimum
approx.	approximately
wt	weight

Notes

The data are valid for the combinations of powder material, machine and parameter sets referred to on page 1, when used in accordance with the relevant Operating Instructions (including Installation Requirements and Maintenance) and Parameter Sheet. Part properties are measured using defined test procedures. Further details of the test procedures used by EOS are available on request. Unless otherwise specified, the data refer to the parameter set MP1_Surface 1.0 or the equivalent default job CC20_MP1_020_default.job. The corresponding data for the parameter set MP1_Performance 1.0 or the equivalent default job CC20_MP1_040_default.job are approximately the same except where otherwise specified.

The data correspond to our knowledge and experience at the time of publication. They do not on their own provide a sufficient basis for designing parts. Neither do they provide any agreement or guarantee about the specific properties of a part or the suitability of a part for a specific application. The producer or the purchaser of a part is responsible for checking the properties and the suitability of a part for a particular application. This also applies regarding any rights of protection as well as laws and regulations. The data are subject to change without notice as part of EOS' continuous development and improvement processes.

EOS®, EOSINT® and DMLS® are registered trademarks of EOS GmbH.

Realize Highest Quality Metal Parts using the Benchmark in Additive Manufacturing — now with the most comprehensive Monitoring Suite

EOS M 290: The DMLS System for a Proven Production of Serial Components with homogenous properties in every part, in every job with every system

With a building volume of 250 x 250 x 325 mm and 400 W laser, the EOS M 290 allows a fast, flexible and costeffective production of metal parts directly from CAD data.

Reproducible part quality, high cost efficiency, comprehensive quality assurance

- The robust system design and the powerful 400-watt fiber laser enable a reliably high performance day in, day out.

- The exceptional high beam quality of the laser spot and its excellent detail resolution is ideal for manufacturing highly complex DMLS components ensuring homogeneous part properties from part-to-part, job-to-job and machine-to-machine.

- The widest range of validated materials and processes available in the market covering all customer requirements.

- The intuitive, open and productive CAM tool EOSPRINT allows optimization of CAD data ensuring a quick and easy job and workflow management. The EOS ParameterEditor module offers developers a large and open tool set ensuring a great freedom for application-specific optimization.

- An comprehensive monitoring suite enables to conduct a real-time quality assurance of all production and quality relevant data. EOSTATE is composed of five different monitoring systems – System, Laser, PowderBed, MeltPool, and Exposure OT (optical tomography).

Technical data EOS M 290

Building volume	250 mm x 250 mm x 325 mm (9.85 x 9.85 x 12.8 in)
Laser type	Yb fibre laser; 400 W
Precision optics	F-theta lens; high-speed scanner
Scanning speed	up to 7.0 m/s (23 ft./sec)
Focus diameter	100 µm (0.004 in)
Power supply	32 A / 400 V
Power consumption	max. 8,5 kW / average 2,4 kW / with platform heating up to 3,2 kW
Inert gas supply	7,000 hPa; 20 m³/h (102 psi; 706 ft³/h)

Dimensions (W x D x H)

System	2,500 mm x 1,300 mm x 2,190 mm (98.4 x 51.2 x 86.2 in)
Recommended installation space	min. 4,800 mm x 3,600 mm x 2,900 mm (189 x 142 x 114 in)
Weight	approx. 1,250 kg (2,756 lb)

Software

EOSTATE Everywhere, EOSPRINT incl. EOS ParameterEditor

Materials*

EOS Aluminium AlSi10Mg, EOS CobaltChrome MP1, EOS MaragingSteel MS1, EOS NickelAlloy HX, EOS NickelAlloy IN625, EOS NickelAlloy IN718, EOS StainlessSteel CX, EOS StainlessSteel PH1, EOS StainlessSteel 17-4PH, EOS StainlessSteel 316L, EOS Titanium Ti64, EOS Titanium Ti64ELI, EOS Titanium TiCP Grade 2

Optional accessories

EOSTATE Monitoring Suite (EOSTATE Laser, EOSTATE PowderBed, EOSTATE MeltPool, EOSTATE Exposure OT), Comfort Powder Module, IPCM-M extra, IPCM-M pro**, wet separator, blasting cabinet

* Further materials on request
** Currently under development

Think the impossible. You can get it.

FLIR GRASSHOPPER®3
USB3 VISION

HIGH PERFORMANCE CCD + CMOS

The high performance Grasshopper3 camera line combines the benefits of CCD with the affordability and data throughput of USB 3.0. Its FPGA and frame buffer-based architecture provides optimal reliability, a rich set of features, and a full image processing pipeline including color interpolation, gamma, and lookup table functionality. The Grasshopper3 offers a powerful, easy-to-use, and cost-effective alternative to Camera Link and dual GigE LAG solutions.

KEY FEATURES

- USB 3.0 for bandwidth, ease of use, and cost effectiveness
- Variety of high-resolution large format CCD and CMOS sensors
- FPGA and frame buffer-based architecture for optimal reliability
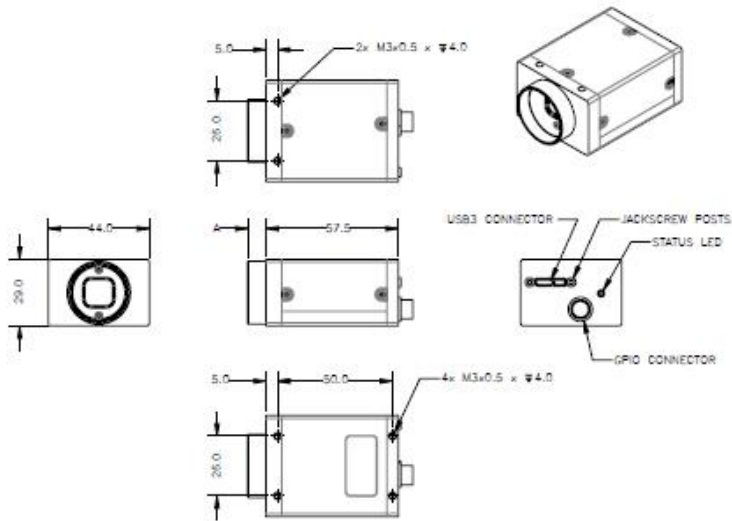
6 GS3-U3-23S6M-C Imaging Performance

Measurement	Video Mode 0	Video Mode 7
Pixel Clock (MHz)	37.13	37.13
ADC (Bits)	10-bit	12-bit
Quantum Efficiency (% at 525 nm)	76	76
Temporal Dark Noise (Read Noise) (e-)	14.19	6.83
Signal to Noise Ratio Maximum (dB)	45.11	45.12
Signal to Noise Ratio Maximum (Bits)	7.49	7.49
Absolute Sensitivity Threshold (γ)	19.69	9.77
Saturation Capacity (Well Depth) (e-)	32406	32513
Dynamic Range (dB)	66.87	72.94
Dynamic Range (Bits)	11.11	12.11
Gain (e-/ADU)	0.51	0.52
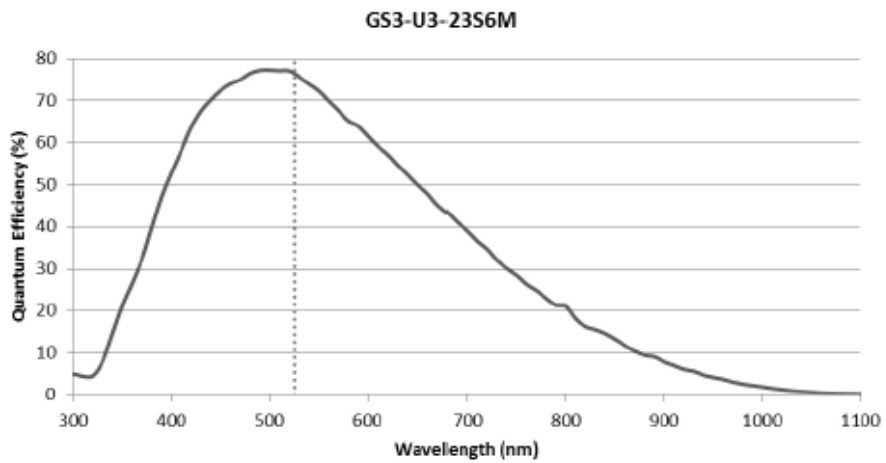
GS3-U3-23S6M

- 5.1-megapixel 2/3" CMOS imager (global shutter)
- Up to 74 fps at full resolution
- 3.45 µm square pixels
- Small size (29 x 29 x 41.5 mm, excluding lens mount)
- 8/10-bit output in a choice of monochrome or raw Bayer color
- Exposure control from 7 µs to 8 seconds in 1 µs steps
- 2X binning for increased sensitivity (monochrome only)
- Single and multi-ROI modes for flexible windowing and use of smaller optics
- Automatic Level Control (ALC) for dynamic lighting conditions
- Accepts power over USB3 Vision interface or via separate 6-pin connector
- C-mount lens mount

See the possibilities

Specifications for GO-5100-USB

Go Series

Specifications	GO-5100-USB
Sensor	2/3" CMOS global shutter (IMX250)
System clock	74.25 MHz (for pulse generator)
Frame rate, full frame	74 frames/sec. @ 8-bit
Active area	8.5 mm (h) x 7.09 mm (v), 11.1 mm diagonal
Cell size	3.45 μm (h) x 3.45 μm (v)
Active pixels	2464 (h) x 2056 (v)
Read-out modes Full	2464 (h) x 2056 (v) up to 74 fps
ROI (mono)	H: 16 to 2464 pixels in 16 pixel steps
	V: 1 to 2056 lines in 1 line steps
ROI (color)	H: 16 to 2464 pixels in 16 pixel steps
	V: 2 to 2056 lines in 2 line steps
Binning	1x2, 2x1, 2x2 (monochrome only)
EMVA 1288 Parameters	12-bit output format
Absolute sensitivity (mono)	3.78 p (λ = 525 nm)
Absolute sensitivity (color)	3.99 p (λ = 525 nm)
Maximum SNR (mono)	40.27 dB
Maximum SNR (color)	40.22 dB
Traditional SNR* mono	>60 dB (0 dB gain)
color	>60 dB (0 dB gain, green)
Video signal output mono	8/10/12-bit monochrome†
color (raw)	8/10/12-bit raw Bayer†
Gain control	Manual/auto 0 dB to +24 dB
White balance (GO-5100C)	Manual, one-push auto, or continuous (3000K to 9000K)
Gamma	0.45, 0.6, 1.0 or 256-point LUT
Synchronization	Internal
Video modes	Normal, Single ROI, Multi ROI, Sequencer (Trigger & Command), Delayed Readout
Trigger input	Opto In, Pulse Generator, Software, NAND Out (2), User Output (2), Action Commands (2)
Trigger modes	Timed/EPS, Trigger Width, Sequencer
Electronic shutter	
Timed exposure	7 μs to 8 sec., in 1 μs steps (8-bit)
Auto shutter	100 μs to 8 sec.
Auto Level Control (ALC)	Shutter range from 100 μs to 8 sec., gain range from 0 dB to +24 dB. Tracking speeds and max values adjustable.
Pre-processing functions	Flat-field correction, color shading correction (GO-5100C-USB), blemish compensation (512 pixels)
Operating temperature	+5°C to +45°C
Storage temperature	-25°C to +60°C
Humidity	20 – 80% non-condensing
Vibration	10 G (20 Hz to 200 Hz XYZ)
Shock	80 G
Regulations	CE (EN 61000-6-2, EN 61000-6-3), FCC Part 15 Class B, RoHS/WEEE
Power	
6-pin connector	12V to 24V DC ± 10%, 3.1 W typical @ +12V
USB 3.0	Bus power: 3.9 W typical @ +5V
Lens mount	C-mount
Dimensions (H x W x L)	29 mm x 29 mm x 41.5 mm (excl. lens mount)
Weight	46 g

Ordering Information

GO-5100M-USB	Monochrome camera with USB3 Vision
GO-5100C-USB	Color camera with USB3 Vision

*Traditional SNR is based on random noise in a single frame, where EMVA SNR measurements consider more comprehensive noise sources and variance over time. For a more complete description, see the manual.

†12-bit output available in video processing bypass mode. See manual for details.

Dimensions

Outside size tolerance ± 0.3mm

Connector pin-out

DC In / Trigger

HIROSE HR10A-7R-6PB(73)

Pin	Signal
1	+12V to +24V DC input
2	Opto In 1
3	Opto Out 1
4	Opto Out 2
5	Opto Common
6	GND

USB 3.0 Interface

Micro B type - ZX360-B-10P or equiv.

No	I/O	Name	Note
1	I	VBUS IN	Power (VBUS)
2	I/O	DM	USB2.0 Differential pair (-)
3	I/O	DP	USB2.0 Differential pair (+)
4		OTG ID	USB OTG ID for identifying lines
5		GND	GND
6	O	FX3 SSTXM	USB3.0 Signal Transmission line (-)
7	O	FX3 SSTXP	USB3.0 Signal Transmission line (+)
8		GND	GND
9	I	FX3 SSRXP	USB3.0 Signal Receiving line (-)
10	I	FX3 SSRXP	USB3.0 Signal Receiving line (+)

Spectral Response

Monochrome ———
Red ——— Green ——— Blue ———
Note: color response includes IR-cut filter (half value 670 nm)

JAi
See the possibilities

For more information please contact:

BOCK OPTRONICS INC.
14 Steinway Blvd., Unit 7
Toronto, Ontario   M9W 6M6

Tel: (416) 674-2804
sales@bockoptronics.ca
www.bockoptronics.ca

3 Mega-Pixel Lens

Schneider
K R E U Z N A C H

Xenoplan 1.9/35-0901

In accordance with the sensitivity of modern 2 / 3" CCD and CMOS sensors, the 3 megapixel lenses are corrected and broadband-coated for the spectral range of 400 – 1000 nm (VIS + NIR). Even under production and / or extreme conditions, the robust mechanical design with lockable focus and iris setting mechanism guarantees reliable continuous use in which the set optical parameters remain in place.

Xenoplan 1.9/35

Key Features

- High-resolution optics
- Highest optical imaging performance
  even with smallest pixel sizes
- Broadband coating (400 - 1000 nm)
- Compact and low weight
- Vibration insensitivity for stable imaging performance
- Focus and iris setting lockable

Applications

- Machine Vision and other imaging applications
- 3D measurement
- Traffic
- Medical
- Robot vision
- Food processing

Technical Specifications

F-number	1.9
Focal length	34.9 mm
Image circle	11 mm
Transmission	400 - 1000 nm
Interface	C-Mount
Weight	92 gr.
Filter thread	M30.5 x 0.5
Order no.	1001960

Contact

Jos. Schneider Optische Werke GmbH	Schneider Asia Pacific Ltd.	Schneider Optics Inc.
Ringstraße 132	20/F Central Tower, 28 Queen's Road	285 Oser Ave.
55543 Bad Kreuznach	Central, Hong Kong	Hauppauge, NY 11788
Germany	China	USA
Phone +49 671 601-205	Phone +852 8302 0301	Phone +1 631 761-5000
Fax +49 671 601-81205	Fax +852 8302 4722	Fax +1 631 761-5090
www.schneiderkreuznach.com	www.schneider-asiapacific.com	www.schneideroptics.com/industrial
industrie@schneiderkreuznach.com	info@schneider-asiapacific.com	industrial@schneideroptics.com

Schneider
KREUZNACH
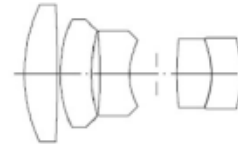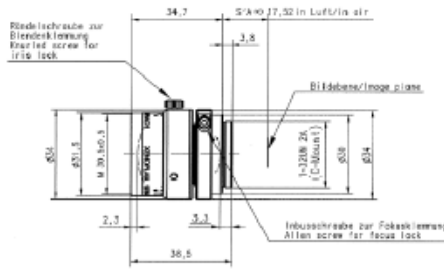
Xenoplan 1.9/35

XENOPLAN 1.9/35MM

f'	=	34.9 mm	β'_P =	0.879
s_F	=	-6.5 mm	s_{EP} =	55.5 mm
$s'_{F'}$	=	17.0 mm	s'_{AP} =	-15.7 mm
HH'	=	-15.8 mm	Σd =	52.6 mm
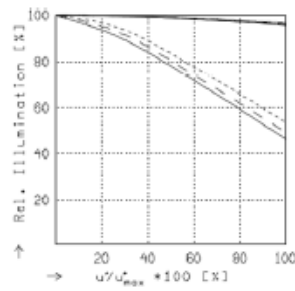
RELATIVE ILLUMINATION

The relativ illumination is shown for the given focal distances or magnifications.

f / 2.0   f / 4.0   f / 8.0

—— β' = -0.0200 u'_{max} = 5.5   00' = 1803.
 β' = -0.0500 u'_{max} = 5.5   00' = 756.
----- β' = -0.1000 u'_{max} = 5.5   00' = 409.
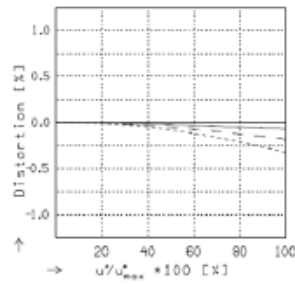
DISTORTION

Distortion is shown for the given focal distances or magnifications. Positive values indicate pincushion distortion and negative values barrel distortion.

—— β' = -0.0200 u'_{max} = 5.5   00' = 1803.
— — β' = -0.0500 u'_{max} = 5.5   00' = 756.
----- β' = -0.1000 u'_{max} = 5.5   00' = 409.
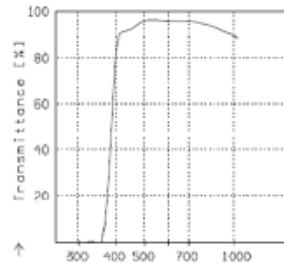
TRANSMITTANCE

Relative spectral transmittance is shown with reference to wavelength.

Xenoplan 1.9/35

Schneider KREUZNACH

XENOPLAN 1.9/35MM

MODULATION with reference to the relative image height

Wavelength	λ	[nm] :	555	655	605	505	455	405
Spectral weighting	[%] :	19.6	23.7	22.2	15.7	12.1	6.7
Spatial frequency R [1/mm] :	10	20	30
Format	[mm X mm] :	6.6 X 8.8	radial ———
Diagonal 2u'	[mm] :	11.0	tangential – –

→ u'/u'$_{max}$ *100 [%] u'$_{max}$ = 5.5   → u'/u'$_{max}$ *100 [%] u'$_{max}$ = 5.5   → u'/u'$_{max}$ *100 [%] u'$_{max}$ = 5.5

f'=34.9 f/2.0 1/ß'=-50.00 00'=1803.   f'=34.9 f/4.0 1/ß'=-50.00 00'=1803.   f'=34.9 f/8.0 1/ß'=-50.00 00'=1803.

→ u'/u'$_{max}$ *100 [%] u'$_{max}$ = 5.5   → u'/u'$_{max}$ *100 [%] u'$_{max}$ = 5.5   → u'/u'$_{max}$ *100 [%] u'$_{max}$ = 5.5

f'=34.9 f/2.0 1/ß'=-20.00 00'=757.   f'=34.9 f/4.0 1/ß'=-20.00 00'=757.   f'=34.9 f/8.0 1/ß'=-20.00 00'=757.

→ u'/u'$_{max}$ *100 [%] u'$_{max}$ = 5.5   → u'/u'$_{max}$ *100 [%] u'$_{max}$ = 5.5   → u'/u'$_{max}$ *100 [%] u'$_{max}$ = 5.5

f'=34.9 f/2.0 1/ß'=-10.00 00'=409.   f'=34.9 f/4.0 1/ß'=-10.00 00'=409.   f'=34.9 f/8.0 1/ß'=-10.00 00'=409.

Focusing :   MTF$_{max}$ at f / 1.9 , R = 30   1/mm. u'/u'$_{max}$ = 0
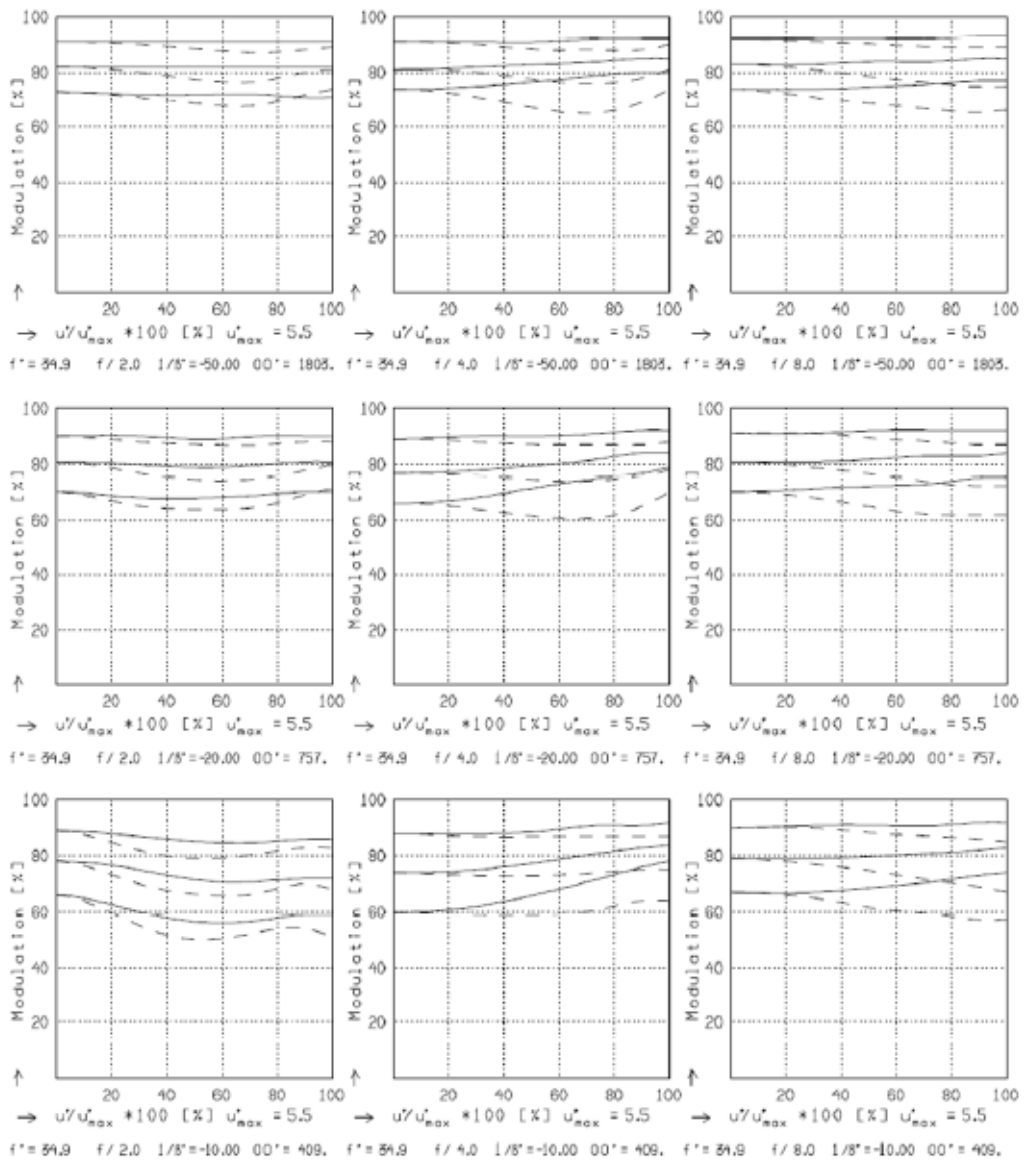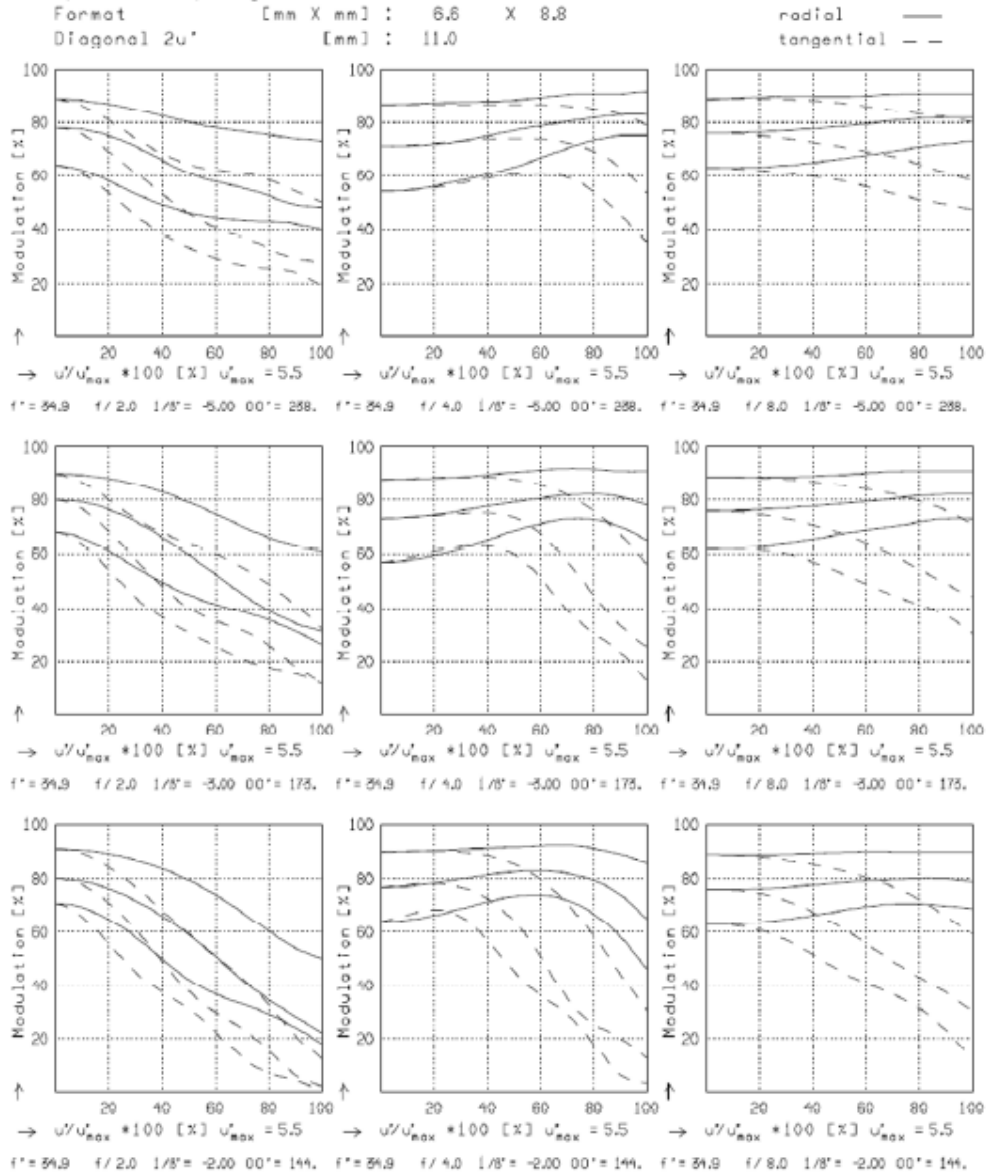
Xenoplan 1.9/35

XENOPLAN 1.9/35MM

MODULATION with reference to the relative image height

Wavelength	λ	[nm] :	555	655	605	505	455	405
Spectral weighting		[%] :	19.6	23.7	22.2	15.7	12.1	6.7
Spatial frequency R [1/mm] :			10	20	30			
Format		[mm X mm] :	6.6	X	8.8		radial	———
Diagonal 2u'		[mm] :	11.0				tangential	— —

f'= 34.9   f/ 2.0   1/ß'= -5.00   00'= 288.   f'= 34.9   f/ 4.0   1/ß'= -5.00   00'= 288.   f'= 34.9   f/ 8.0   1/ß'= -5.00   00'= 288.

f'= 34.9   f/ 2.0   1/ß'= -3.00   00'= 173.   f'= 34.9   f/ 4.0   1/ß'= -3.00   00'= 173.   f'= 34.9   f/ 8.0   1/ß'= -3.00   00'= 173.

f'= 34.9   f/ 2.0   1/ß'= -2.00   00'= 144.   f'= 34.9   f/ 4.0   1/ß'= -2.00   00'= 144.   f'= 34.9   f/ 8.0   1/ß'= -2.00   00'= 144.

Focusing :   MTF$_{max}$ at f / 1.9 . R = 30   1/mm. u'/u'$_{max}$ = 0

MADS – 160330 – Caspian C-39N0-250

PRODUCT
● ● ● ● ● ● ●

Caspian
C-39N0-250

Overview

The Caspian C-39N0-250 is an electronically focus controllable C-Mount lens, based on the Arctic 39N0 Liquid Lens. It incorporates all necessary electronic components to drive the Liquid Lens, and just needs a DC power supply; focus can be controlled through either an RS232, I2C, Analog or SPI input. With a 25 mm effective focal length, and 2/3" sensor compatibility, it is specifically designed for machine vision applications. For more information on this module, please refer to TEDS – Caspian C-39N0-250.

Ordering information

C-C-39N0-250-XX where **XX** determines objective configuration:

    I2C : I2C or analog operation
    RS33 : RS232 with 3.3 V signal or analog operation
    RS12 : RS232 with 12 V signal or analog operation
    SPI : SPI operation only

Key Features

- o Variable focus from 12 cm to infinity
- o Silent
- o Supports I2C - Analog - RS232 - SPI interfaces
- o Supports closed loop operation

Contents

varioptic
a Business Unit of
Parrot

MADS – 160330 – Caspian C-39N0-250

PRODUCT

Opto-Electrical performance

Performances described below are for 25°C

Optical Performances at V_∞	Symbol	Min	Typ	Max	Unit	Notes
Voltage for infinite focus	V_∞		46		V	(2)
Focal length at V_∞	EFL		25		mm	
Image circle diameter			11		mm	
Corner Chief Ray Angle	CRA		0		°	
Flange distance			17.5		mm	(3)
F- number	F#	4		22	-	
Diagonal Field of view	DFOV		24.8		°	(4)
Focus control performances						
Focus distance	x	12		∞	cm	(2)
Voltage for x= 12 cm	V_{12cm}		62		V	(2)

Notes :

(1) For more information on the behavior of the C-39N0-250 or Arctic 39N0 please refer to lens and module full datasheet.

(2) Distance to object referred to the principal plane of the objective, as described as below:

Object plane
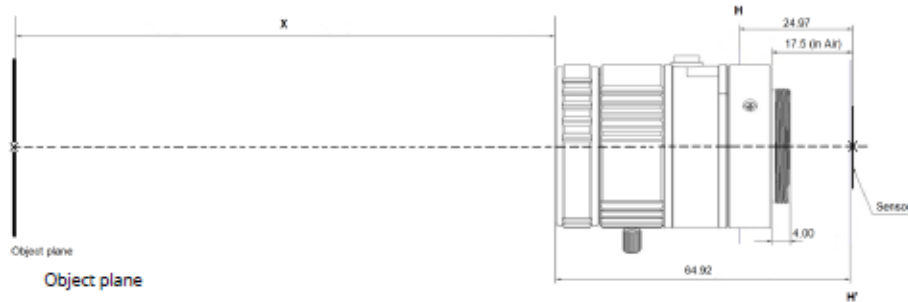
(3) Refer to ISO 10935
(4) For a sensor size of 2/3"

Temperature Range

Parameter	Unit	Min	Typ	Max	Notes
Operating temperature range	°C	0°C	25	+50°C	TBC
Storage temperature range	°C	-40°C	25	+85°C	TBC

MADS – 160330 – Caspian C-39N0-250

PRODUCT

Mechanical dimensions

Weight: 116.4g

MADS – 160330 – Caspian C-39N0-250

PRODUCT

Electrical connection

The module has a 6 pin connector for power and control (JST_1).
Connector reference: JST SHR-06V-S-B
Wire reference: JST SH3-SH3-28300

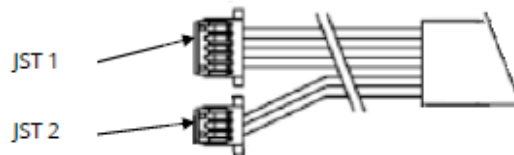These pins have different functions depending on the module version.

JST 1

JST 2

Figure 1: Electrical interface

Communication terminal JST_1

Pin	Name	Description
1	VIN	Positive power supply (+5 to +24 VDC/ red wire)
2	GND	Ground (black wire)
3	I2Csda_Rx_SDI	Multipurpose pin (depending on the part/ yellow wire)
4	I2Cscl_Rx_SCK	Multipurpose pin (depending on the part/ blue wire)
5	SDO_Ana	Multipurpose pin (depending on the part)
6	MCLR	Programming pin (must be unconnected)

The function of the multipurpose pins depends on the part number:

		Caspian C-39N0-250-			
Pin	Name	R12	R33	SPI	I2C
3	I2Csda_Rx_SDI	Rx (RS232)	Rx (3.3V)	SDI	SDA
4	I2Cscl_Tx_SCK	Tx (RS232)	Tx (3.3V)	SCK	SCL
5	SDO_Ana	Analog input	Analog input	SDO	Analog input

Programming terminal JST_2

Pin	Name	R12	R33	SPI	I2C
1	ICSPDAT	Rx (RS232)	Rx (3.3V)	SDI	SDA
2	ICSPCLK	Tx (RS232)	Tx (3.3V)	SCK	SCL
3	MCLR	Analog input	Analog input	SDO	Analog input

MADS – 160330 – Caspian C-39N0-250

PRODUCT

Electrical Specifications

Parameter	Symbol	Min	Typ	Max	Unit	Notes
Power supply						
Input voltage	V_{cc}	3.3	5	24	V	
Current consumption - Active mode	I_{cc}		50		mA	(1)
Current consumption – Standby mode	$I_{cc\,Stb}$		12		mA	
Control voltage						
RS12						
I2Csda_Rx_SDI / I2Cscl_Rx_SCK		-25		25	V	(2)
RS33/I2C/SPI						
I2Csda_Rx_SDI / I2Cscl_Rx_SCK		-0.3		3.6	V	(2)
SDO_Ana pin		-0.3		3.6	V	(2)
MCLR pin		-0.3		3.6	V	

Notes :

(1) Current consumption depends on the voltage applied on the Liquid Lens, value given for 4.5v power supply, see below chart for more details.

Typical current consumption Icc (mA)

Driver state and voltage applied to Lens		(standby)	25 V	70 V
Power supply	3.3V	16.4	70	100
	4.5V	12	50	71
	12V	4.5	27	34
	24V	2.2	20	23

(2) Absolute Maximum Ratings

Analog control

Caspian C-30N0-250 modules, except the SPI version, can be controlled by an analog voltage. In this case, the voltage seen by the Liquid Lens is given by the following equation:
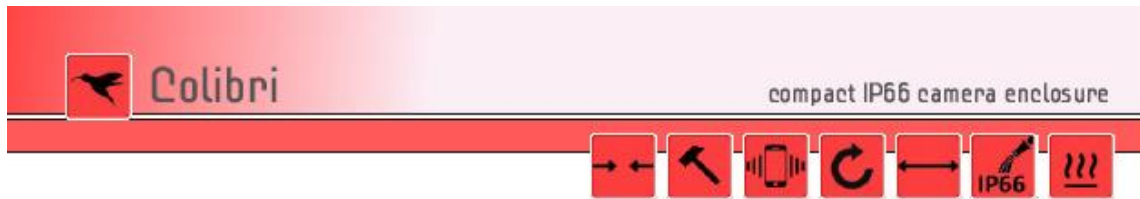
$$V_{rms} = (V_a * 22.5) + 24 \qquad \text{with } 0V < V_a < 2V$$

With:
- V_{rms} : rms value of the voltage seen by the Liquid Lens (AC voltage)
- V_a : analog input voltage (DC voltage)

Colibri — compact IP66 camera enclosure

Benefits:

- For cameras up to 30 x 30mm cross section
- Robust construction
- Compact size
- Small dead weight
- High IP protection class
- Flexible camera positioning
- High chemical resistance
- Vibration-proof mounting
- Camera mount included
- Excellent heat dissipation
- Front and back side camera assembly possible
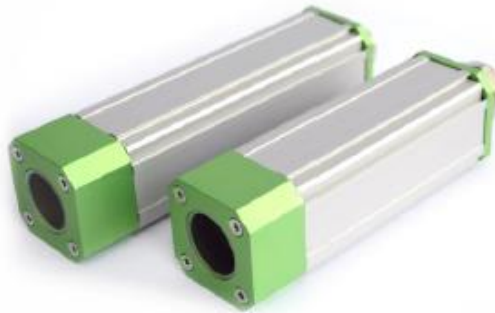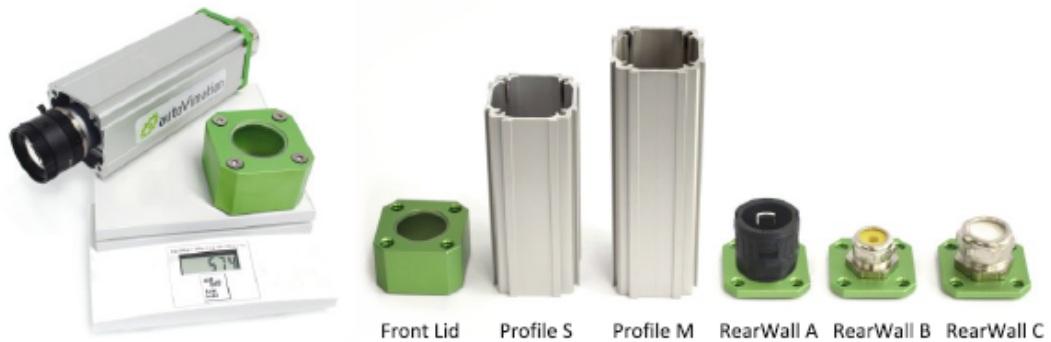
Technical Details:

Camera Size	29 x 29mm 30 x 30mm	Weight (incl. camera mount)	Approx. 420g (Size S) Approx. 465g (Size M)
Max. Lens Diameter	39mm	Enclosure Material	Anodized Aluminum
Inner Length	146mm (Size S) 176mm (Size M)	Enclosure Seals	NBR
Enclosure Dimensions (w x h x l, without cable gland)	50 x 50 x 156mm (Size S) 50 x 50 x 186mm (Size M)	Cable Gland Aperture (max. connector size)	20mm (Rear Wall A) 16.5mm (Rear Wall B) 20.5mm (Rear Wall C)
Window Aperture	28mm	Cable Diameter	4-6.5mm (Rear Wall B) Self drilling (Rear Wall C)
Window Material	Borosilicate, BK7	Cable Gland Seal	TPE
Window Coating	Double sided AR		
Window Seal	Hytrel		
Protection Class	IP66 (Nema 4)		

The camera mount guarantees excellent heat dissipation

autoVimation
building machine vision

sales@autovimation.com   +49 721 6276756   +49 721 6276759

Front Lid   Profile S   Profile M   RearWall A   RearWall B   RearWall C

Order Numbers:

Colibri S				Colibri M		
Camera Height	Rear Wall	Order Number		Camera Height	Rear Wall	Order Number
29mm	A	22.900.120		29mm	A	22.900.150
	B	22.901.120			B	22.901.150
	C	22.902.120			C	22.902.150
30mm	A	23.000.120		30mm	A	22.900.150
	B	23.001.120			B	23.001.150
	C	23.002.120			C	23.002.150

Accessories:

Product	Image	Order Number		Product	Image	Order Number
Colibri Air Nozzle		50.100.023		Mounting Kit 24		5.240.000
90° Deflection Mirror + Adapter required		20.020.004 + 10.062.979		Mounting Kit 26		5.260.000
30mm to 40mm Adapter Bracket		10.062.979		Mounting Kit 27		5.270.000
Corrugated Tube 28mm		20.000.006		Mounting Kit 28		5.280.000
Mounting Kit 21		5.210.000		Mounting Kit 29		5.290.000

Colibri Drawings

Front Lid

28mm aperture

50

50

max. 39mm lens diameter

39

Size S

28 internal

34

156 (146 internal)

Rear Wall A

max. 20mm connector

Size M

28 internal

21

186 (176 internal)

Rear Wall B

max. 13.5mm connector
4 - 6.5mm cable

25

Rear Wall C

max. 20mm connector
several cables
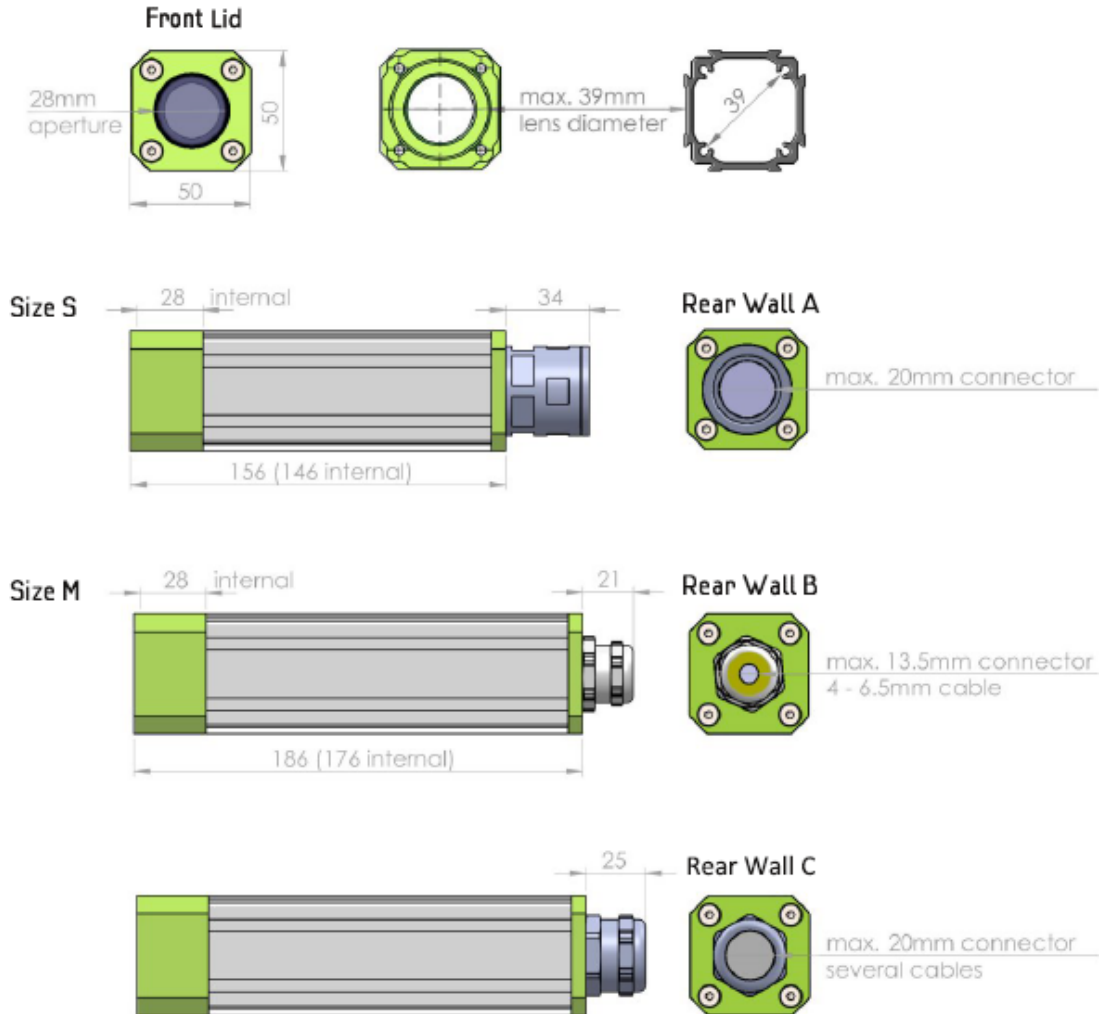
**HiWatch Compact** — Diode laser illumination for high-speed imaging

Oseir's diode lasers are powerful and affordable tools for imaging and measuring of small, high-speed targets in industrial and research applications, production and process development.

The HiWatch is an ideal instrument for non-intrusive imaging and diagnostics purposes due to adjustable sequence and number of pulses. Pulse duration is freely adjustable within the specifications. HiWatch replaces and even outperforms traditionally used Xenon flash lamps and double-NdYAG lasers in applications requiring high-intensity illumination and precise timing in a robust and compact package.

HiWatch laser systems are designed for use in demanding industrial environments. The optical components stand humidity, dust and corrosive effects. Lightweight and robust HiWatch systems are easy to handle and offer a versatile solution to imaging measurements even in harsh environments.

Typical HiWatch applications:

➢ Monitoring and analysis of high-intensity processes such as laser welding and laser cutting, plasma assisted processes etc.
➢ High-speed imaging of rapid moving targets, e.g. micro machining processes etc.
➢ Velocity measurement of high-speed targets, PIV (Particle Image Velocimetry)
➢ Spray analysis and particle/droplet sizing (medical sprays, paint sprays etc.)
➢ Non-intrusive measurement of fluids, orifices, droplets, particles with stroboscopic illumination
➢ High-speed machine vision applications
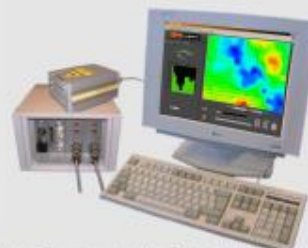
HiWatch is a key component of many high-performance vision systems.

Oseir
www.oseir.com

Oseir Ltd
Alasniitynkatu 30
FIN-33560 TAMPERE
info@oseir.com

Application examples:
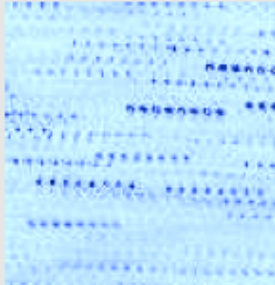
8-shot PIV image from a water channel with 20 micron beads.
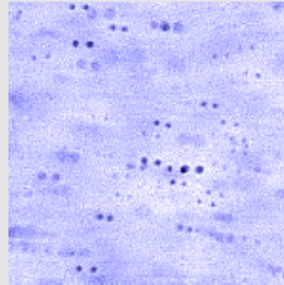
Spray droplets monitoring & analysis. Measurement of velocity and size.

Water jet for cutting of paper, jet thickness 200 microns. Measurement of width & size.

PIV (Particle Imaging Velocimetry) and illumination of rapid flow and spray processes.

Visualization and sizing of particles, and solid objects in sprays, flows and in high-intensity environments such as flames, explosions etc.

High-speed image capture and velocity measurement of any fast moving target with a CCD camera.

HiWatch specifications:

PARAMETER		NOTE
Emission wavelength	802 nm	
Output geometry	7 x 1 mm, adjustable direction	1
Emission power	50 W	2
Single pulse length	0.05—1 us	
Max. pulse frequency	5 MHz	
Max. pulse energy	0.5 mJ	
Laser head weight	Approx. 350 g	
Laser head dimensions	130 x 64 x 25 (LxWxH)	
Cooling	Filtered dry compressed air	
Safety class	3B	3

NOTES:
1. 10º horizontal fan angle
2. Peak power
3. Conforming to IEC 60125-A1+A2.

For further information or quotations please approach Oseir Ltd. directly or visit our website at www.oseir.com.